Chapter III

Physics results of AMS-01

From the STS-91 flight of AMS-01, we gained experience and knowledge on how to execute a particle physics experiment in space. The construction of the complete detector which will be deployed on the Space Station will benefit from this practical understanding of the technical capabilities and performance of each component in actual flight conditions.

Results from the Shuttle flight (AMS-01):

Two hours after the shuttle lift-off on June 2, 1998, we began performing tests on AMS. We were informed by NASA that the Ku-band system for the orbiter was not functioning. This meant that we could only obtain data in real time via the S-band when the orbiter passed over certain ground-receiving stations around the globe. With this limited information, however, it was immediately determined that the detector had survived the shuttle launch and all the detector components were operating nominally. Figure 22a shows the on-orbit Silicon Tracker displacement from the measurement of the laser alignment system. Figure 22b shows the same measurement when AMS was on the launch pad. Comparing these two measurements indicates that the entire Tracker system has remained stable with an accuracy of l.l μ $\pm$ 3μ. The AMS Digital Data Recorder was activated in the Shuttle crew compartment ensuring that all data were being recorded. The next photograph shows Astronaut Dr Franklin Chang-Diaz recording the AMS-01 data on board Shuttle Discovery.

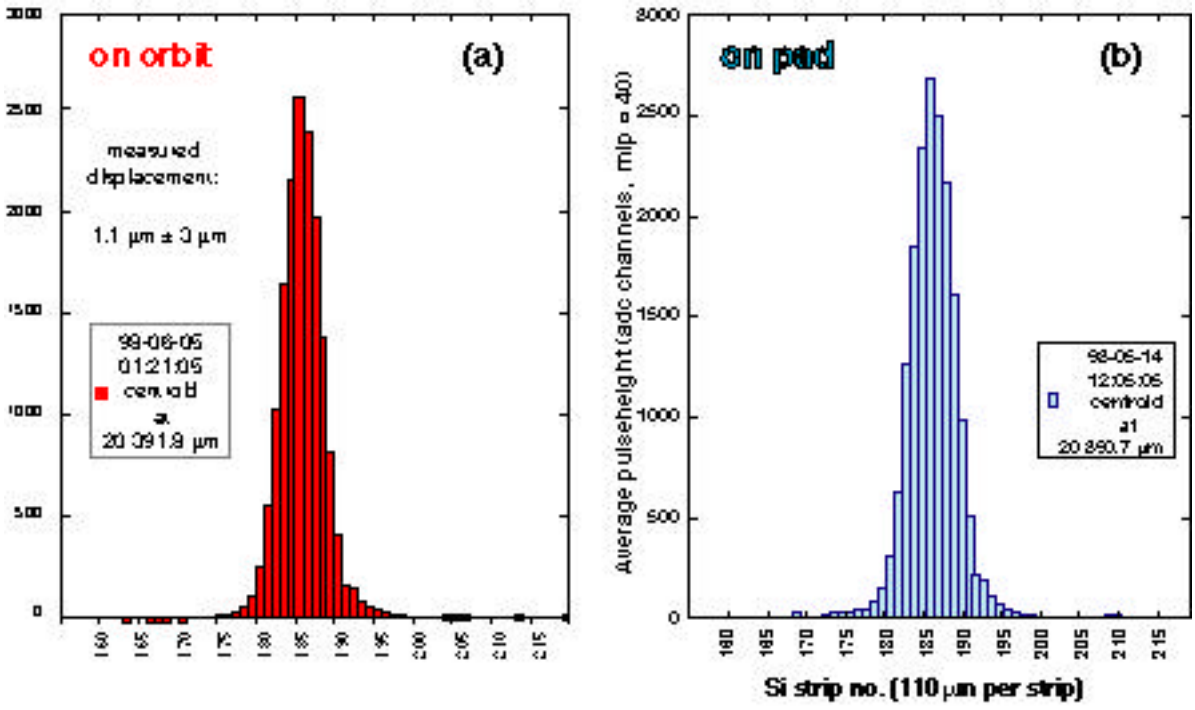

Figure 22 : Laser displacement measured in orbit (a). On launch pad (b).

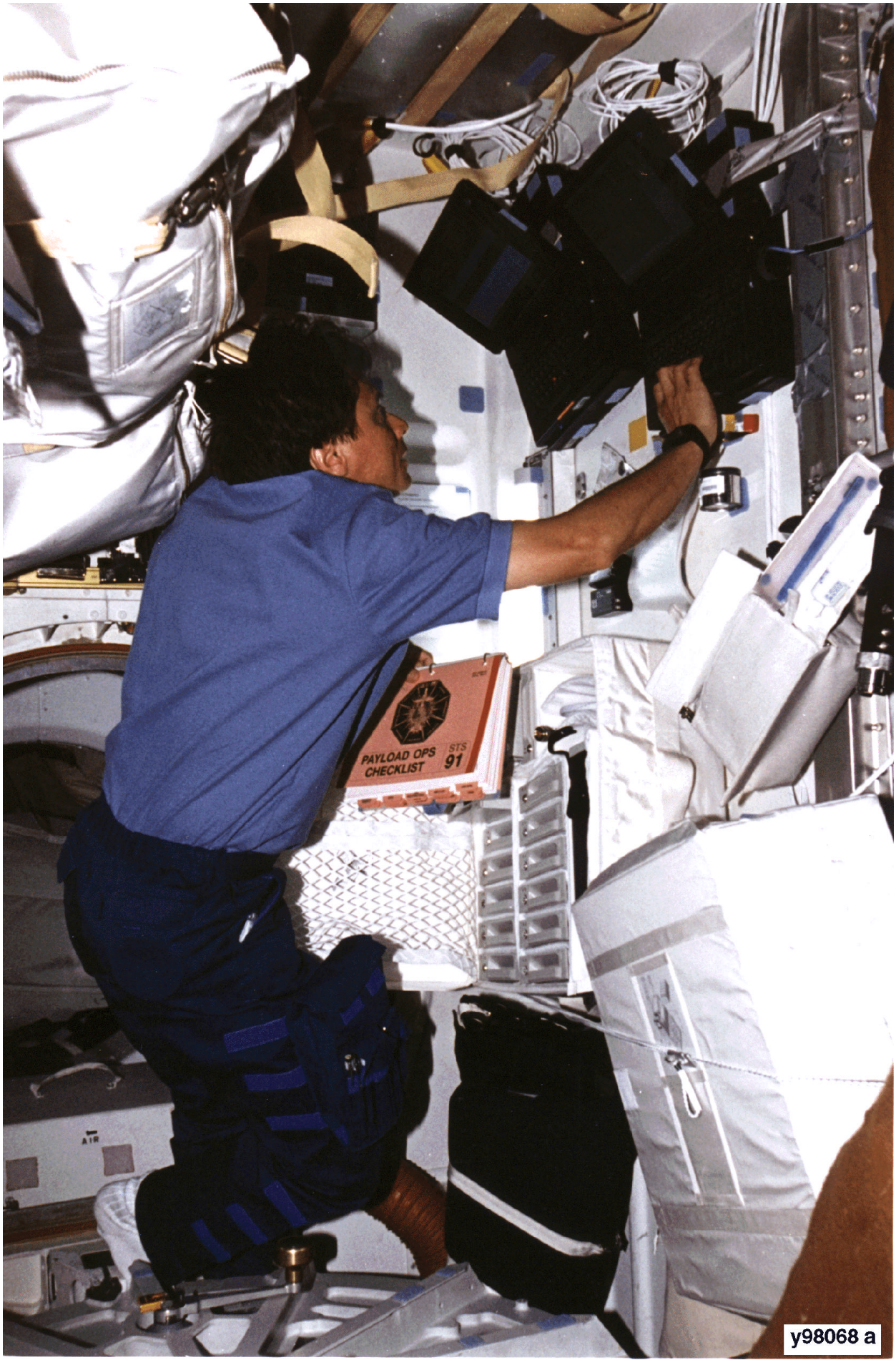
PAYLOAD OPS
CHECKLIST
STS
91
y98068 a

During flight, the detector was located in the payload bay of the space shuttle and operated in vacuum. Events were triggered by the coincidence of signals in all four TOF planes consistent with the passage of a charged particle through the active tracker volume. Triggers with a coincident signal from the Veto Counters were rejected. The detector performance as well as temperature and magnetic field were monitored continuously. A total of 100 million triggers were recorded.

After the flight, AMS-01 was checked again :

- First, the detector was placed in a heavy ion (He, C) beam from 1.0 to 5.6 GV at 600 different incident angles. This test was done with a total of 45 million events and was carried out at GSI-Darmstadt. Figure 23 shows the location of AMS at the GSI ion accelerator and Figure 24 shows one of the carbon-beam test results. The photograph (Figure 25) shows AMS-01 spectrometer being rotated to one of the 600 angle positions.
- Second, the detector was placed in a proton and pion beam at CERN, with momentum from 2 to 14 GeV at 1200 different incident angles. This test was done with a total of 100 million events.

The continued monitoring of AMS-01 confirmed that the detector performance before, during and after the flight remained the same. In particular, the alignment of the silicon tracker remained the same to an accuracy of ~ 5 μm.

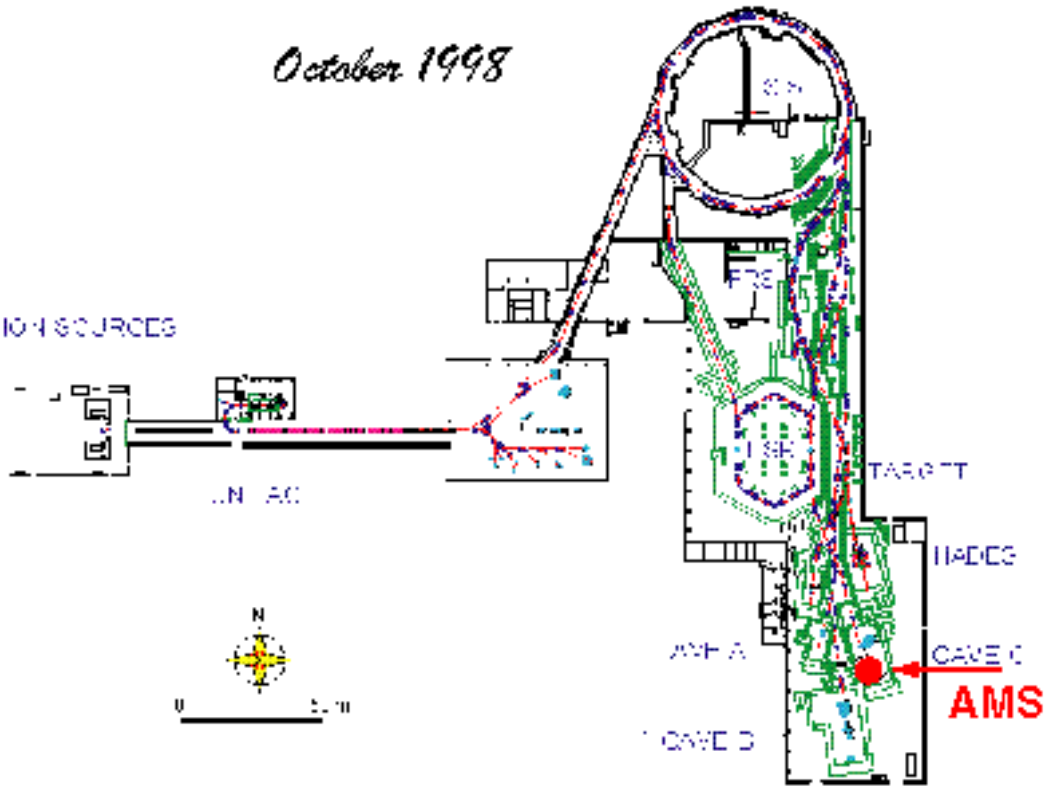

Figure 23 : Location of AMS at the GSI Ion Accelerator.

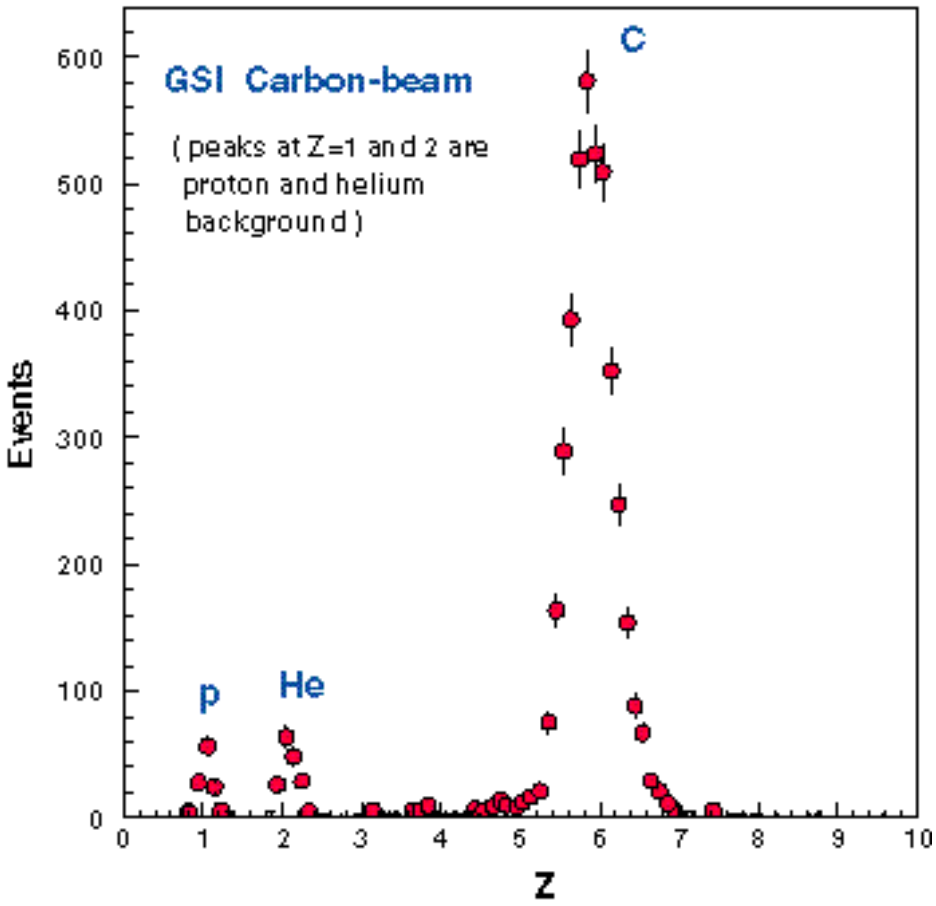

Figure 24 : Results of tests of AMS-01 at GSI carbon beam .

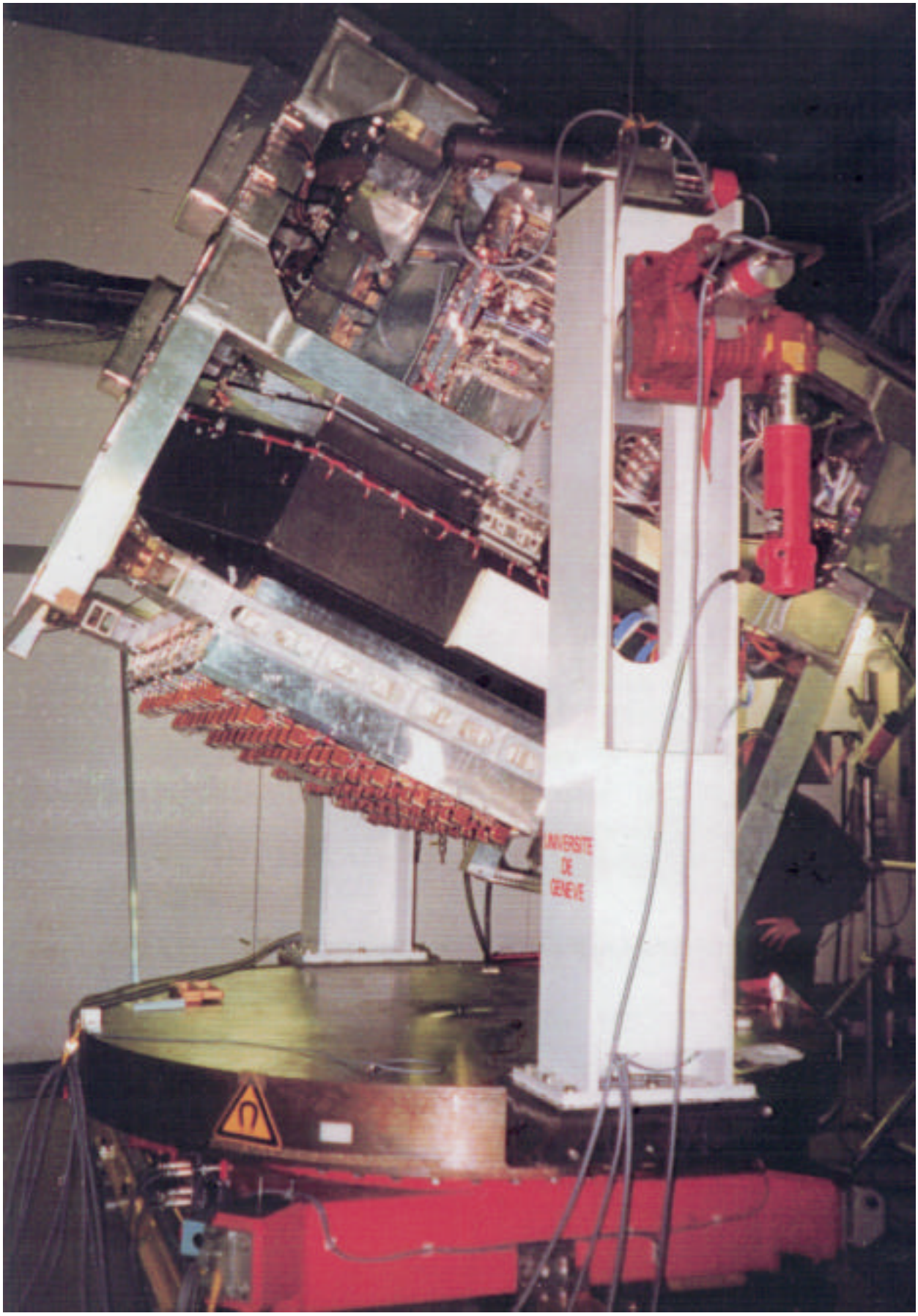

Figure 25 : AMS-01 being rotating at GSI for beam tests.

An intensive international analysis effort was organized to analyze the AMS-01 data. All the results were checked by two independent analysis groups.

Five papers have been published in Physics Letters B and are included here (as Attachments I, II, III, IV, V) together with the referees' comments (included at the end of each paper). Other papers on deuterium, antiprotons … are in preparation. In addition, the editor of Physics Reports has invited us to publish a Physics Report on the construction and physics results of AMS-01, which will be published shortly.

Attachment I

Search for Antihelium in Cosmic Rays

The AMS Collaboration

Abstract

The Alpha Magnetic Spectrometer (AMS) was flown on the space shuttle *Discovery* during flight STS–91 in a 51.7° orbit at altitudes between 320 and 390 km. A total of 2.86×10^6 helium nuclei were observed in the rigidity range 1 to 140 GV. No antihelium nuclei were detected at any rigidity. An upper limit on the flux ratio of antihelium to helium of $< 1.1 \times 10^{-6}$ is obtained.

Published in Phys. Lett. B461 (2 Sep 1999) 387-396
Accepted without comment by the referee.

Introduction

The existence (or absence) of antimatter nuclei in space is closely connected with the foundation of the theories of elementary particle physics, CP–violation, baryon number nonconservation, Grand Unified Theory (GUT), etc. Balloon–based cosmic ray searches for antinuclei at altitudes up to 40 km have been carried out for more than 20 years; all such searches have been negative [1–7]. The absence of annihilation gamma ray peaks excludes the presence of large quantities of antimatter within a distance of the order of 10 Mpc from the earth. The baryogenesis models are not yet supported by particle physics experimental data. To date baryon nonconservation and large levels of CP–violation have not been observed. The Alpha Magnetic Spectrometer (AMS) [8] is scheduled for a high energy physics program on the International Space Station. In addition to searching for dark matter and the origin of cosmic rays, a major objective of this program is to search for antinuclei using an accurate, large acceptance magnetic spectrometer. AMS was flown on the space shuttle *Discovery* on flight STS–91 in June 1998. This was primarily a test flight that would enable the AMS team to gather data on background sources, adjust operating parameters and verify the detector's performance under actual space flight conditions. A search for antihelium nuclei using the data collected during this precursor flight is reported. The signal investigated is nuclei with charge $Z = -2$.

AMS on STS–91

A schematic cross section in the bending plane of AMS as flown on STS–91, Fig. 1, shows the permanent magnet, tracker, time of flight hodoscopes, Cerenkov counter and anticoincidence counters. The AMS coordinate system, as shown, coincides with the shuttle coordinate system, with the z–axis (up in the figure) pointing out of the shuttle payload bay and the x–axis pointing towards the tail of the shuttle. The geometric acceptance was ~ 0.3 m^2sr. AMS as flown on STS–91 will be described in detail elsewhere [9].

The magnet provided the analyzing power of the spectrometer. It was made of 1.9 tons of Nd-Fe-B in the shape of a cylindrical shell of inner diameter 1115 mm and length 800 mm. The Nd-Fe-B was magnetized to 46 MGOe with the direction varying to provide a dipole field in the x direction, perpendicular to the cylinder axis. At the center the magnetic field was 0.14 Tesla and the analyzing power, BL^2, was 0.14 Tm^2.

The trajectory of charged particles traversing the magnet bore was observed with a tracker made of six planes, T1 to T6, of double sided silicon microstrip detectors [10]. For AMS on STS–91 half of the tracker area was equipped. From the deflection the rigidity, $R = pc/|Z|e$ (GV), was measured. The tracker also provided a determination of charge magnitude, $|Z|$, through multiple energy loss measurements. Special care was taken to minimize the amount of material in the tracker construction; the total amount of material within the tracker volume was less than 3% of a radiation length parallel to the z–axis. The tracker alignment was made first with metrology, continuously monitored with an infrared laser system and then verified with high momentum tracks from the CERN PS test beam. During flight hits in the tracker were measured with an accuracy of ~ 10 μm in the bending, or y, direction and ~ 30 μm in the x and z directions. The resolution in terms of rigidity was verified for $|Z| \geq 2$ nuclei using helium and carbon ion beams at GSI–Darmstadt. Fig. 2 shows the rigidity resolution for $Z = 2$ flight data and the agreement with the $Z = 2$ helium data measured at GSI. Note that at low momenta the resolution was limited by multiple scattering.

The particle direction and velocity were measured with a four layer, S1 to S4, time-of-flight (TOF) hodoscope. Each layer consisted of 14 scintillator paddles of thickness 10 mm, width 110 mm, hermetically arranged with a 5 mm overlap. As shown in Fig. 1, two layers were above the magnet

and two below. The paddles in each pair were orthogonal. The pulse height information recorded from the TOF paddles provided an additional determination of $|Z|$. The typical accuracy of the time of flight measurements was 105 psec for $|Z| = 2$. Fig. 3 shows the velocity, $\beta = v/c$, resolution for high rigidity $|Z| = 2$ particles.

The velocity measurement was complemented by a threshold Cerenkov counter made of aerogel with a refractive index of 1.035.

A layer of anticoincidence scintillation counters (ACC) covered the inner surface of the magnet to reject the background caused by particles passing through or interacting in the magnet walls and support structures. The detector was also shielded from low energy (up to several MeV) particles by thin carbon fiber walls (LEPS). For particles arriving from above, as shown in Fig. 1, the amount of material at normal incidence was 1.5 g/cm^2 in front of the TOF system, and 3.5 g/cm^2 in front of the tracker.

During construction, the detector components went though extensive space qualification tests (acceleration, vibration, thermal vacuum, electromagnetic interference and radiation). For example, the magnet was tested in a centrifuge to 17.7 g. Key electronics components were tested at Dubna in heavy ion beams of Ne, Ar and Kr.

During flight the detector was located in the payload bay of the space shuttle and operated in vacuum. Events were triggered by the coincidence of signals in all four TOF planes consistent with the passage of a charged particle through the active tracker volume. Triggers with a coincident signal from the ACC were vetoed. The detector performance as well as temperature and magnetic field were monitored continuously. A total of 100 million triggers were recorded.

After the flight, the detector was checked again:

- first, the detector was placed in a heavy ion (He, C) beam from 1.0 to 5.6 GV at 600 different incident angles. This test was done with a total of 45 million events and was carried out at GSI–Darmstadt.

- second, the detector was placed in a proton and pion beam at CERN with momentum from 2 to 14 GeV at 1200 different incident angles. This test was done with a total of 100 million events.

The continued monitoring of the detector confirmed that the detector performance before, during and after the flight remained the same. In particular, the alignment of the silicon tracker remained the same to an accuracy of $\sim 5\,\mu$m.

Event Selection

After the shuttle had attained orbit, data collection commenced on 3 June 1998 and continued over the next nine days for a total of 184 hours. During data taking the shuttle altitude varied from 320 to 390 km and the latitude ranged between $\pm$ 51.7 degrees. Before rendezvous with the MIR space station the attitude of the shuttle was maintained to keep the z–axis of AMS (see Fig. 1) pointed within 45 degrees of the zenith. While docked, the attitude was constrained by MIR requirements and varied substantially. After undocking the pointing was maintained within 1, 20 and then 40 degrees of the zenith. Shortly before descent the shuttle turned over and the pointing was towards the nadir. For this search, data collected while passing through the South Atlantic Anomaly was excluded.

The procedure to search for antihelium began with event reconstruction, which included:

- Measurement of the particle rigidity, R, from the deflection of the trajectory measured by the tracker in the magnetic field. To ensure that the particle was well measured, hits in at least four tracker planes were required and the fitting was performed with two different algorithms, the results of which were required to agree.

- Measurement of the particle velocity, β, and direction, $\hat{z} = \pm 1$, from the TOF, where $\hat{z} = -1$ signifies a downward going particle in Fig. 1.

- Determination of the magnitude of the particle charge, $|Z|$, from the measurements of energy losses in the TOF counters and tracker planes (corrected for β).

From this reconstruction the sign of the particle charge was derived from the deflection in the rigidity fit and the direction. The particle mass was derived from $|Z|$R and β.

The major backgrounds to the antihelium ($Z = -2$) search are the abundant amount of protons and electrons ($|Z| = 1$) and helium ($Z = +2$). To distinguish antihelium from e^-, p and He, the detector response to e^-, p and He was studied in three ways:

(i) from the e^-, p and He data collected in flight.

(ii) from the He beam data at GSI and the p beam data at the CERN PS.

(iii) from Monte Carlo studies of (i) and (ii).

Key points in the selection for $\overline{\text{He}}$ events and the rejection of background were:

to select events with $|Z| = 2$: This was to ensure no contamination from $|Z| = 1$ events with a wrongly measured charge magnitude which would mimic $|Z| > 1$ events. Fig. 4 shows the energy deposition and the assigned charge magnitude as measured independently by the TOF and the tracker. The probability of the wrong charge magnitude being assigned by the combined TOF and tracker measurements was estimated to be less than 10^{-7}.

to determine the sign of $|Z| = 2$ events: This was to distinguish He from $\overline{\text{He}}$. This was done with the following method:

(i) **Identify the particle direction:** measurement of the particle direction leads to the correct assignment of the sign of the charge. Fig. 5 shows the particle direction, $\hat{z}/\beta$, distribution. No events were observed between the $\hat{z} = +1$ and $\hat{z} = -1$ populations which indicates there was no leakage of particles from one population to the other and the direction was always correctly assigned.

(ii) **Identify large angle nuclear scattering events:** events in which a single nuclear scattering in one of the inner tracker planes, T2–T5, introduced a large angle kink in the track and might cause an incorrect measurement of the charge sign. This background was suppressed by a cut on the estimated rigidity error. Additional suppression was achieved by requiring agreement for the rigidity and charge sign measured using all the hits in the tracker and separately in the first three hits and the last three hits along the track. Fig. 6 shows the asymmetry, $A_{12} = (R_1 - R_2)/(R_1 + R_2)$, of the rigidity measured with the first and last three hits along the track, R_1 and R_2, and the cuts applied. From Fig. 6 we see that whereas these cuts reject much of the large angle scattering events (Fig. 6a), the cuts do not reject the genuine signal (Fig. 6b).

(iii) **Identify events with collinear delta rays:** events with collinear debris, *e.g.* delta rays, from an interaction of the primary particle in the tracker material which may shift a measured point from the trajectory, leading to an incorrectly measured rigidity and charge sign. This background was efficiently rejected by an isolation cut which rejected events with an excess of energy observed within 5 mm of the track.

A probabilistic function was then constructed from measurements of the velocity, rigidity and energy loss which described the compatibility of these measurements with the passage of a helium or antihelium nucleus of mass $A = 3$ or 4. Fig. 7 shows the compatibility distribution for the antihelium candidates (Fig. 7a) and helium samples together with Monte Carlo predictions for the helium event distribution (Fig. 7b). As seen, the compatibility cut enables us to reject the small remaining background and keep nearly all of the helium sample.

The results of our search are summarized in Fig. 8. As seen, we obtain a total of 2.86×10^6 He events up to a rigidity of 140 GV. We found no antihelium event at any rigidity.

Results and Interpretation

Since no antihelium nuclei were observed, we can only establish an upper limit on their flux. Here three upper limits on this flux relative to the observed flux of helium nuclei are calculated which differ in the assumptions used for the antihelium rigidity spectrum. In the first it is assumed to have the same shape as the helium rigidity spectrum. In the second this spectrum is assumed to be uniform. Finally a conservative estimate is made independent of the antihelium rigidity spectrum.

All of these methods require the measured rigidity spectrum to be corrected for the detector resolution and efficiency as a function of the measured, R_m, and incident, R, rigidity. The detection efficiency including the rigidity resolution function, $f(\mathrm{R}, \mathrm{R}_m)$, was evaluated through complete Monte Carlo simulation using the GEANT Monte Carlo package [11]. The incident rigidity spectrum, $dN'/d\mathrm{R}$ was extracted from the measured spectrum, $dN'/d\mathrm{R}_m$, by numerical deconvolution of $dN'/d\mathrm{R}_m = \int (dN'/d\mathrm{R}) \times f(\mathrm{R}, \mathrm{R}_m) d\mathrm{R}$. To obtain the detector efficiency for antihelium, $\varepsilon_{\overline{\mathrm{He}}}(\mathrm{R})$, a small correction was applied to the efficiency for helium nuclei, $\varepsilon_{\mathrm{He}}(\mathrm{R})$, based on the estimated [12] difference in absorption cross sections.

Letting $N_{\mathrm{He}}(\mathrm{R}_i)$ be the number of incident helium nuclei in the rigidity bin $(\mathrm{R}_i, \mathrm{R}_i{+}\Delta\mathrm{R})$ and $N'_{\mathrm{He}}(\mathrm{R}_i)$ be the number of measured He in the same rigidity bin after correction for the detector resolution, then $N'_{\mathrm{He}}(\mathrm{R}_i) = \varepsilon_{\mathrm{He}}(\mathrm{R}_i) N_{\mathrm{He}}(\mathrm{R}_i)$, where $\varepsilon_{\mathrm{He}}(\mathrm{R}_i)$ is the detection efficiency in this bin, and similarly for antihelium. Over the rigidity interval studied no $\overline{\mathrm{He}}$ were found, $N'_{\overline{\mathrm{He}}}(\mathrm{R}_i) = 0$ for each i. At the 95 % confidence level this is taken to be less than 3 and the differential upper limit for the flux ratio is given by:

$$\frac{N_{\overline{\mathrm{He}}}(\mathrm{R}_i)}{N_{\mathrm{He}}(\mathrm{R}_i)} < \frac{3 \quad / \varepsilon_{\overline{\mathrm{He}}}(\mathrm{R}_i)}{N'_{\mathrm{He}}(\mathrm{R}_i) / \varepsilon_{\mathrm{He}}(\mathrm{R}_i)} \,. \tag{1}$$

The difference between $\varepsilon_{\overline{\mathrm{He}}}(\mathrm{R}_i)$ and $\varepsilon_{\mathrm{He}}(\mathrm{R}_i)$ is small, so these terms practically cancel and the results below are essentially independent of the detection efficiency.

(i) If the incident $\overline{\mathrm{He}}$ spectrum is assumed to have the same shape as the He spectrum over the range $1 < \mathrm{R} < 140$ GV, then summing equation (1) yields a limit of:

$$\frac{N_{\overline{\mathrm{He}}}}{N_{\mathrm{He}}} \;<\; 1.1 \times 10^{-6}.$$

(ii) Assuming a uniform $\overline{\mathrm{He}}$ rigidity spectrum, and using a mean $\overline{\mathrm{He}}$ inverse detection efficiency, $\langle 1/\varepsilon_{\overline{\mathrm{He}}}\rangle = \sum(1/\varepsilon_{\overline{\mathrm{He}}}(\mathrm{R}_i))/n$, and noting that $N'_{\overline{\mathrm{He}}} = \sum N'_{\overline{\mathrm{He}}}(\mathrm{R}_i) = 0$ which is also taken to be less than 3 at the 95 % C.L., summing equation (1) yields a limit of

$$\frac{N_{\overline{\mathrm{He}}}}{N_{\mathrm{He}}} = \frac{\sum N_{\overline{\mathrm{He}}}(\mathrm{R}_i)}{\sum N_{\mathrm{He}}(\mathrm{R}_i)} < \frac{3 \quad \langle 1/\varepsilon_{\overline{\mathrm{He}}}\rangle}{\sum N'_{\mathrm{He}}(\mathrm{R}_i)\,/\varepsilon_{\mathrm{He}}(\mathrm{R}_i)}, \tag{2}$$

$$\text{which evaluates to} \quad \frac{N_{\overline{\mathrm{He}}}}{N_{\mathrm{He}}} < 1.8\times10^{-6} \text{ for R = 1.6 to 40 GV}$$

$$\text{and} \quad \frac{N_{\overline{\mathrm{He}}}}{N_{\mathrm{He}}} < 3.9\times10^{-6} \text{ for R = 1.6 to 100 GV.}$$

(iii) For a conservative upper limit, which does not depend on the antihelium spectrum, equation (1) is summed from $\mathrm{R}_{min} = 1.6$ GV up to a variable R_{max} and instead of the mean value $\langle 1/\varepsilon_{\overline{\mathrm{He}}}\rangle$ the minimum value of this efficiency in the $(\mathrm{R}_{min}, \mathrm{R}_{max})$ interval is taken, yielding

$$\frac{\sum N_{\overline{\mathrm{He}}}(\mathrm{R}_i)}{\sum N_{\mathrm{He}}(\mathrm{R}_i)} < \frac{3 \quad /\varepsilon^{min}_{\overline{\mathrm{He}}}(\mathrm{R}_{min}, \mathrm{R}_{max})}{\sum N'_{\mathrm{He}}(\mathrm{R}_i)\,/\varepsilon_{\mathrm{He}}(\mathrm{R}_i)}, \text{ where } \mathrm{R}_i = (\mathrm{R}_{min}, \mathrm{R}_{max}). \tag{3}$$

These results are shown in Fig. 9 as a function of R_{max}.

In conclusion, we found no antihelium nuclei at any rigidity. Up to rigidities of 140 GV, 2.86×10^6 helium nuclei were measured. Assuming the antihelium rigidity spectrum to have the same shape as the helium spectrum, an upper limit at the 95 % confidence level on the relative flux of antihelium to helium of 1.1×10^{-6} was obtained. This result is an improvement in both sensitivity and rigidity range over previous measurements [7]. This flight has shown that the completed AMS on the International Space Station will provide many orders of magnitude of improvement in the sensitivity to search for anithelium.

Acknowledgements

We thank Professors S. Ahlen, C. Canizares, A. De Rujula, J. Ellis, A. Guth, M. Jacob, L. Maiani, R. Mewaldt, R. Orava, J. F. Ormes and M. Salamon for helping us to initiate this experiment.

The success of the first AMS mission is due to many individuals and organizations outside of the collaboration. The support of NASA was vital in the inception, development and operation of the experiment. The dedication of Douglas P. Blanchard, Mark J. Sistilli, James R. Bates, Kenneth Bollweg and the NASA and Lockheed–Martin Mission Management team, the support of the Max–Plank Institute for Extraterrestrial Physics, the support of the space agencies from Germany (DLR), Italy (ASI), France (CNES) and China and the support of CSIST, Taiwan, made it possible to complete this experiment on time.

The support of CERN and GSI–Darmstadt, particularly of Professor Hans Specht and Dr. Reinhard Simon made it possible for us to calibrate the detector after the shuttle returned from orbit.

We are most grateful to the STS–91 astronauts, particularly to Dr. Franklin Chang–Diaz who provided vital help to AMS during the flight.

The support of INFN, Italy, ETH–Zürich, the University of Geneva, the Chinese Academy of Sciences, Academia Sinica and National Central University, Taiwan, the RWTH–Aachen, Germany, the University of Turku, the University of Technology of Helsinki, Finland, U.S. DOE and M.I.T. is gratefully acknowledged.

References

[1] G.F.Smoot *et al.,* Phys. Rev. Lett. **35** (1975) 258–261.

[2] G.Steigman *et al.,* Ann. Rev. Astr. Ap. **14** (1976) 339.

[3] G.Badhwar *et al.,* Nature **274** (1978) 137.

[4] A.Buffington *et al.,* ApJ **248** (1981) 1179–1193.

[5] R.L.Golden *et al.,* ApJ **479** (1997) 992.

[6] J.F.Ormes *et al.,* ApJ Letters **482** (1997) L187.

[7] T.Saeki *et al.,* Phys. Lett. **B422** (1998) 319.

[8] S. Ahlen *et al.,* Nucl. Inst. Meth. **A350** (1994) 351.

[9] AMS Collab, J. Alcaraz *et al.,* Nucl. Inst. Meth. , , in preperation;
see also: G. M. Viertel, M. Capell, Nucl. Inst. Meth. **A 419** (1998) 295–299.

[10] AMS Tracker Group, G. Ambrosi *et al.,* Nucl. Inst. Meth. (1999), to be submitted to NIM.

[11] See R. Brun *et al.*, "GEANT 3", CERN DD/EE/84-1 (Revised), September 1987.
The FLUKA program (see P. A. Aamio, FLUKA Users Guide, CERN Report TIS–RP–190 (1990)) is used to simulate hadronic interactions..

[12] A.A.Moiseev and J.F.Ormes, Astroparticle Physics **6** (1997) 379–386.

The AMS Collaboration:

J.Alcaraz[x], D.Alvisi[j], B.Alpat[ab], G.Ambrosi[r], H.Anderhub[af], L.Ao[g], A.Arefiev[aa], P.Azzarello[r], E.Babucci[ab], L.Baldini[j,l], M.Basile[j], D.Barancourt[s], F.Barao[v,u], G.Barbier[s], G.Barreira[v], R.Battiston[ab], R.Becker[l], U.Becker[l], L.Bellagamba[j], P.Béné[r], J.Berdugo[x], P.Berges[l], B.Bertucci[ab], A.Biland[af], S.Bizzaglia[ab], S.Blasko[ab], G.Boella[y], M.Bourquin[r], G.Bruni[j], M.Buenerd[s], J.D.Burger[l], W.J.Burger[ab], X.D.Cai[l], R.Cavalletti[j], C.Camps[b], P.Cannarsa[af], M.Capell[l], D.Casadei[j], J.Casaus[x], G.Castellini[p], Y.H.Chang[m], H.S.Chen[i], Z.G.Chen[g], N.A.Chernoplekov[z], A.Chiarini[j], T.H.Chiueh[m], Y.L.Chuang[ac], F.Cindolo[j], V.Commichau[b], A.Contin[j], A.Cotta–Ramusino[j], P.Crespo[v], M.Cristinziani[r], J.P.da Cunha[n], T.S.Dai[l], J.D.Deus[u], L.K.Ding[i], N.Dinu[k], L.Djambazov[af], I.D'Antone[j], Z.R.Dong[h], P.Emonet[r], F.J.Eppling[l], T.Eronen[ae], G.Esposito[ab], P.Extermann[r], J.Favier[c], C.C.Feng[w], E. Fiandrini[ab], F.Finelli[j], P.H.Fisher[l], R.Flaminio[c], G.Fluegge[b], N.Fouque[c], Yu.Galaktionov[aa,l], M.Gervasi[y], P.Giusti[j], W.Q.Gu[h], T.G.Guzik[e], K.Hangarter[b], A.Hasan[af], V.Hermel[c], H.Hofer[af], M.A.Huang[ac], W.Hungerford[af], M.Ionica[k], R.Ionica[k], J.Isbert[e], M.Jongmanns[a,f], W.Karpinski[a], G.Kenney[af], J.Kenny[ab], W.Kim[ad], A.Klimentov[l,aa], J.Krieger[a,1], R.Kossakowski[c], V.Koutsenko[l,aa], G.Laborie[s], T.Laitinen[ae], G.Lamanna[ab], G.Laurenti[j], A.Lebedev[l], S.C.Lee[ac], G.Levi[j], P.Levtchenko[ab,2], T.P.Li[i], C.L.Liu[w], H.T.Liu[i], M.Lolli[j], I.Lopes[n], G.Lu[g], Y.S.Lu[i], K.Lübelsmeyer[a], D.Luckey[l], W.Lustermann[af], G.Maehlum[ab,3], C.Maña[x], A.Margotti[j], F.Massera[j], F.Mayet[s], R.R.McNeil[e], B.Meillon[s], M.Menichelli[ab], F.Mezzanotte[j], R.Mezzenga[ab], A.Mihul[k], G.Molinari[j], A.Mourao[u], A.Mujunen[t], F.Palmonari[j], G.Pancaldi[j], A.Papi[ab], I.H.Park[ad], M.Pauluzzi[ab], F.Pauss[af], E.Perrin[r], A.Pesci[j], A.Pevsner[d], R.Pilastrini[j], M.Pimenta[v,u], V.Plyaskin[aa], V.Pojidaev[aa], H.Postema[l,4], E.Prati[j], N.Produit[r], P.G.Rancoita[y], D.Rapin[r], F.Raupach[a], S.Recupero[j], D.Ren[af], Z.Ren[ac], M.Ribordy[r], J.P.Richeux[r], E.Riihonen[ae], J.Ritakari[t], U.Roeser[af], C.Roissin[s], R.Sagdeev[o], D.Santos[s], G.Sartorelli[j], A.Schultz von Dratzig[a], G.Schwering[a], V.Shoutko[l], E.Shoumilov[aa], R.Siedling[a], D.Son[ad], T.Song[h], M.Steuer[l], G.S.Sun[h], H.Suter[af], X.W.Tang[i], Samuel C.C.Ting[l], S.M.Ting[l], F.Tenbusch[a], G.Torromeo[j], J.Torsti[ae], J.Trümper[q], J.Ulbricht[af], S.Urpo[t], I.Usoskin[y], E.Valtonen[ae], J.Vandenhirtz[a], E.Velikhov[z], B.Verlaat[af,5], I.Vetlitsky[aa], F.Vezzu[s], J.P.Vialle[c], G.Viertel[af], D.Vité[r], H.Von Gunten[af], S.Waldmeier Wicki[af], W.Wallraff[a], B.C.Wang[w], J.Z.Wang[g], Y.H.Wang[ac], J.P.Wefel[e], E.A.Werner[a,1], C.Williams[j], S.X.Wu[l,m], P.C.Xia[h], J.L.Yan[g], L.G.Yan[h], C.G.Yang[i], M.Yang[i], P.Yeh[ac], H.Y.Zhang[f], D.X.Zhao[h], G.Y.Zhu[i], W.Z.Zhu[g], H.L.Zhuang[i], A.Zichichi[j].

---

[a] I. Physikalisches Institut, RWTH, D-52056 Aachen, Germany[6]
[b] III. Physikalisches Institut, RWTH, D-52056 Aachen, Germany[6]
[c] Laboratoire d'Annecy-le-Vieux de Physique des Particules, LAPP, F-74941 Annecy-le-Vieux CEDEX, France
[e] Louisiana State University, Baton Rouge, LA 70803, USA
[d] Johns Hopkins University, Baltimore, MD 21218, USA
[f] Center of Space Science and Application, Chinese Academy of Sciences, 100080 Beijing, China
[g] Chinese Academy of Launching Vehicle Technology, CALT, 100076 Beijing, China
[h] Institute of Electrical Engineering, IEE, Chinese Academy of Sciences, 100080 Beijing, China
[i] Institute of High Energy Physics, IHEP, Chinese Academy of Sciences, 100039 Beijing, China[7]
[j] University of Bologna and INFN-Sezione di Bologna, I-40126 Bologna, Italy
[k] Institute of Microtechnology, Politechnica University of Bucharest and University of Bucharest, R-76900 Bucharest, Romania
[l] Massachusetts Institute of Technology, Cambridge, MA 02139, USA
[m] National Central University, Chung-Li, Taiwan 32054
[n] Laboratorio de Instrumentacao e Fisica Experimental de Particulas, LIP, P-3000 Coimbra, Portugal
[o] University of Maryland, College Park, MD 20742, USA
[p] INFN Sezione di Firenze, I-50125 Florence, Italy
[q] Max–Plank Institut fur Extraterrestrische Physik, D-85740 Garching, Germany
[r] University of Geneva, CH-1211 Geneva 4, Switzerland
[s] Institut des Sciences Nucleaires, F-38026 Grenoble, France
[t] Helsinki University of Technology, FIN-02540 Kylmala, Finland
[u] Instituto Superior Técnico, IST, P-1096 Lisboa, Portugal
[v] Laboratorio de Instrumentacao e Fisica Experimental de Particulas, LIP, P-1000 Lisboa, Portugal
[w] Chung–Shan Institute of Science and Technology, Lung-Tan, Tao Yuan 325, Taiwan 11529
[x] Centro de Investigaciones Energéticas, Medioambientales y Tecnologícas, CIEMAT, E-28040 Madrid, Spain[8]
[y] INFN-Sezione di Milano, I-20133 Milan, Italy
[z] Kurchatov Institute, Moscow, 123182 Russia
[aa] Institute of Theoretical and Experimental Physics, ITEP, Moscow, 117259 Russia
[ab] INFN-Sezione di Perugia and Universitá Degli Studi di Perugia, I-06100 Perugia, Italy[9]
[ac] Academia Sinica, Taipei, Taiwan
[ad] Kyungpook National University, 702-701 Taegu, Korea
[ae] University of Turku, FIN-20014 Turku, Finland
[af] Eidgenössische Technische Hochschule, ETH Zürich, CH-8093 Zürich, Switzerland
[1] Now at ISATEC, Aachen, Germany.
[2] Permanent address: Nuclear Physics Institute, St. Petersburg, Russia.
[3] Now at IDE–AS, Oslo, Norway.
[4] Now at European Laboratory for Particle Physics, CERN, CH-1211 Geneva 23, Switzerland.
[5] Now at National Institute for High Energy Physics, NIKHEF, NL-1009 DB Amsterdam, The Netherlands.
[6] Supported by the Deutsches Zentrum für Luft– und Raumfahrt, DLR.
[7] Supported by the National Natural Science Foundation of China.
[8] Supported also by the Comisión Interministerial de Ciencia y Tecnología.
[9] Also supported by the Italian Space Agency.

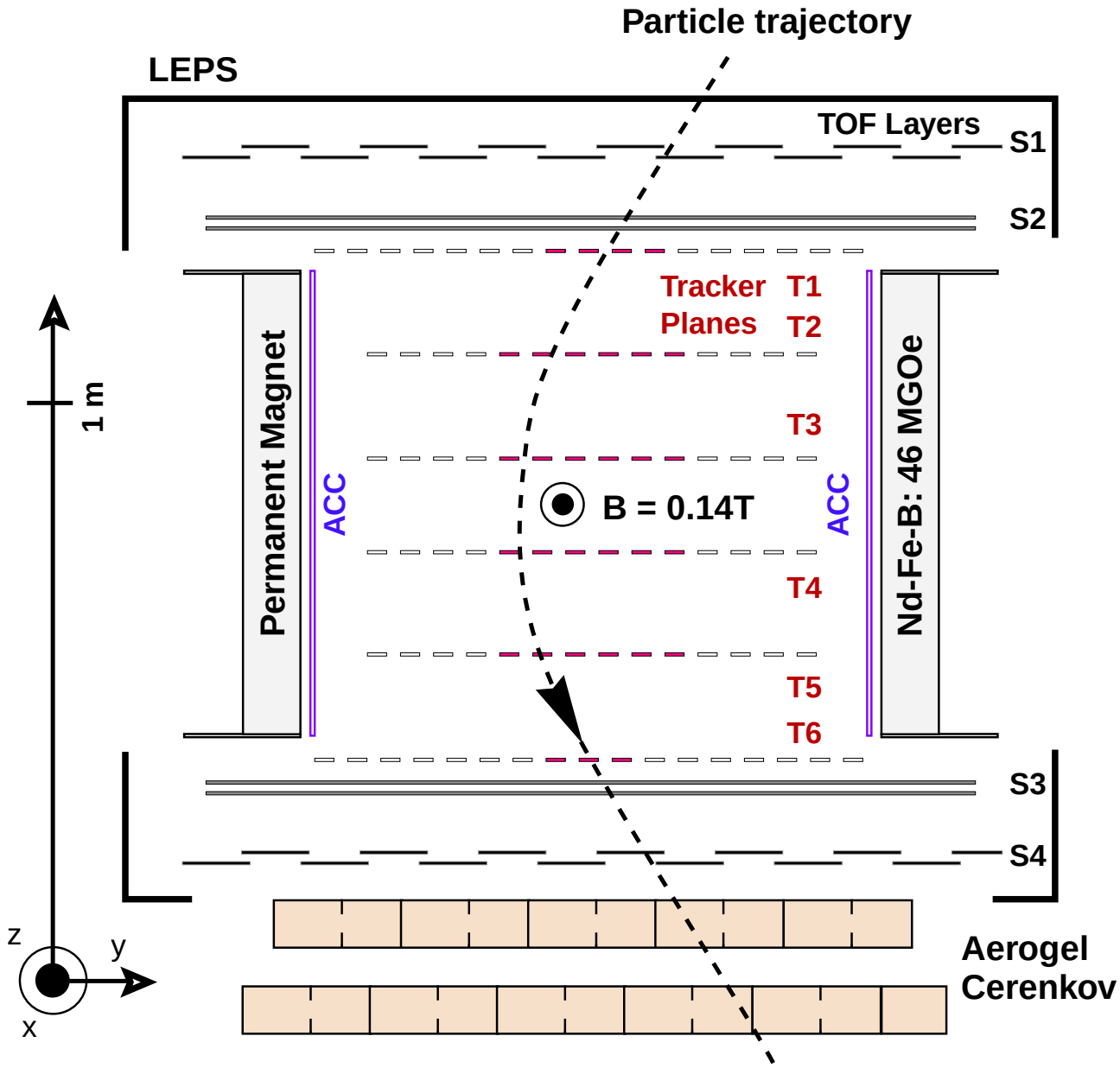

Figure 1: Schematic view of AMS as flown on STS–91 showing the cylindrical permanent magnet, the silicon microstrip tracker planes T1 to T6, the time of flight (TOF) hodoscope layers S1 to S4, the aerogel cerenkov counter, the anticoincidence counters (ACC) and low energy particle shields (LEPS).

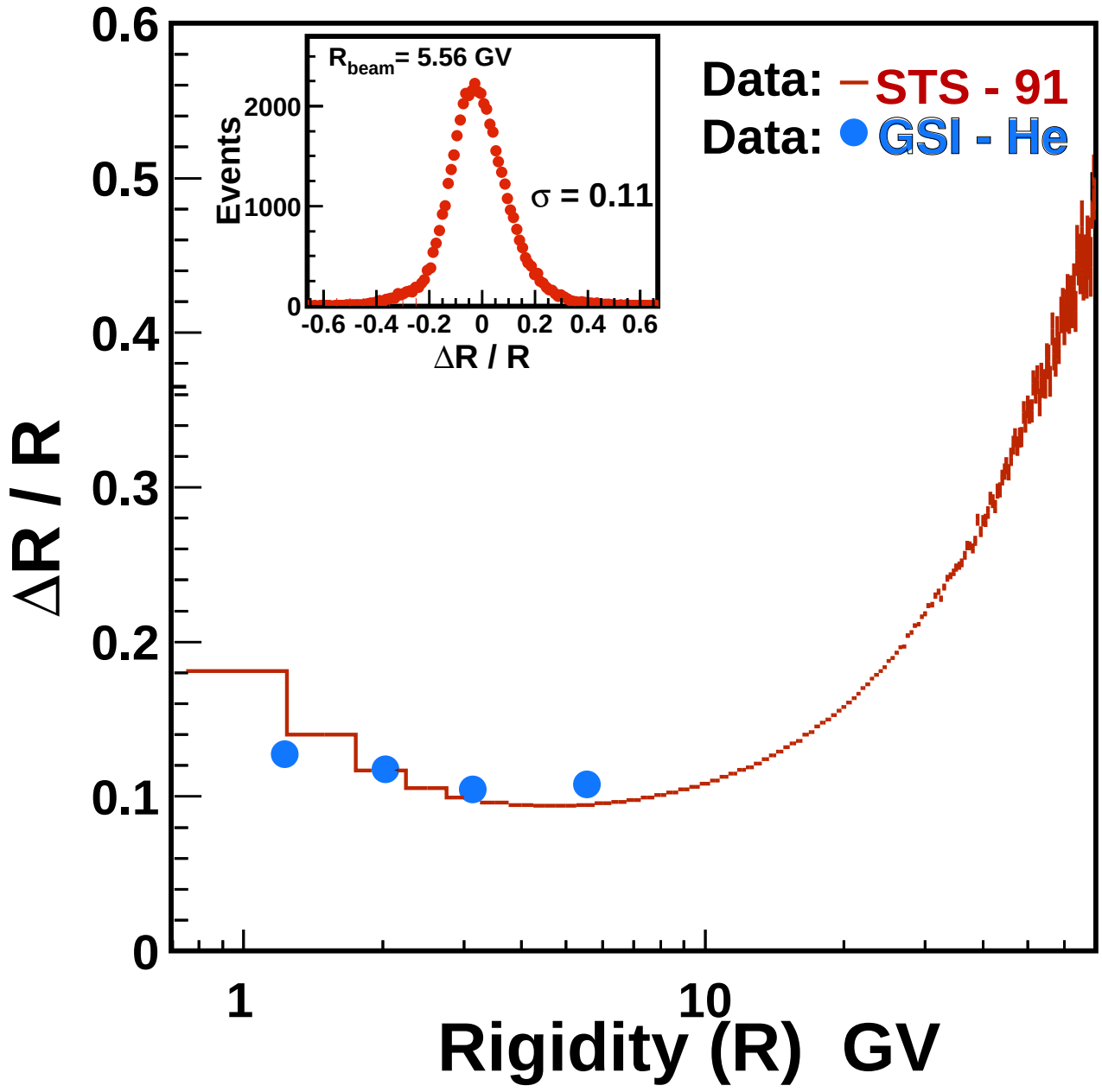

Figure 2: Rigidity resolution for $|Z| = 2$ flight data (histogram) compared with the GSI He test beam (points).
Inset: Typical rigidity resolution, $\Delta R/R = (R_{measured} - R_{beam})/R_{beam}$, from the GSI He data.

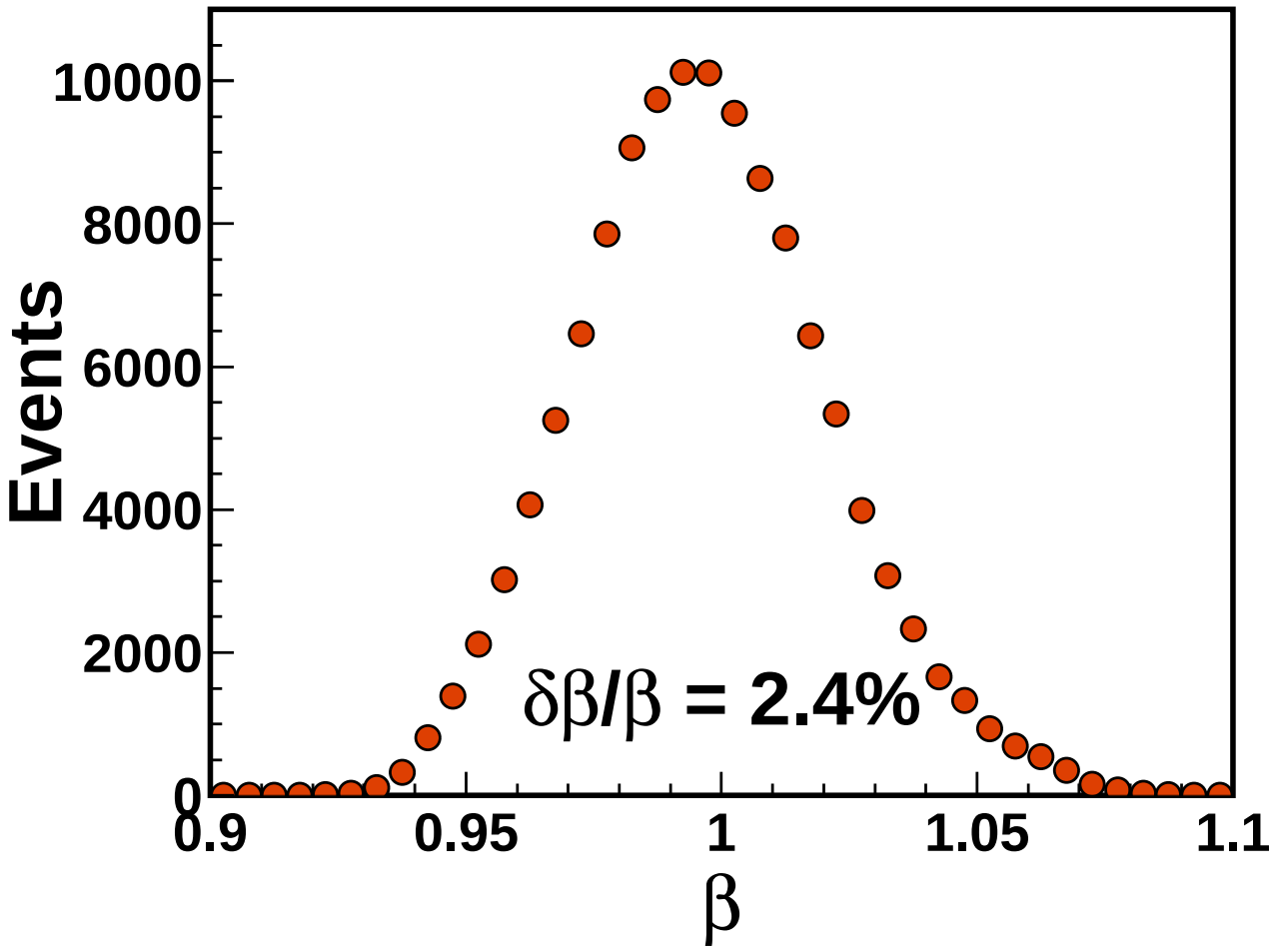

Figure 3: Measured velocity, β = v/c, distribution for |Z| = 2 events with R > 16 GV.

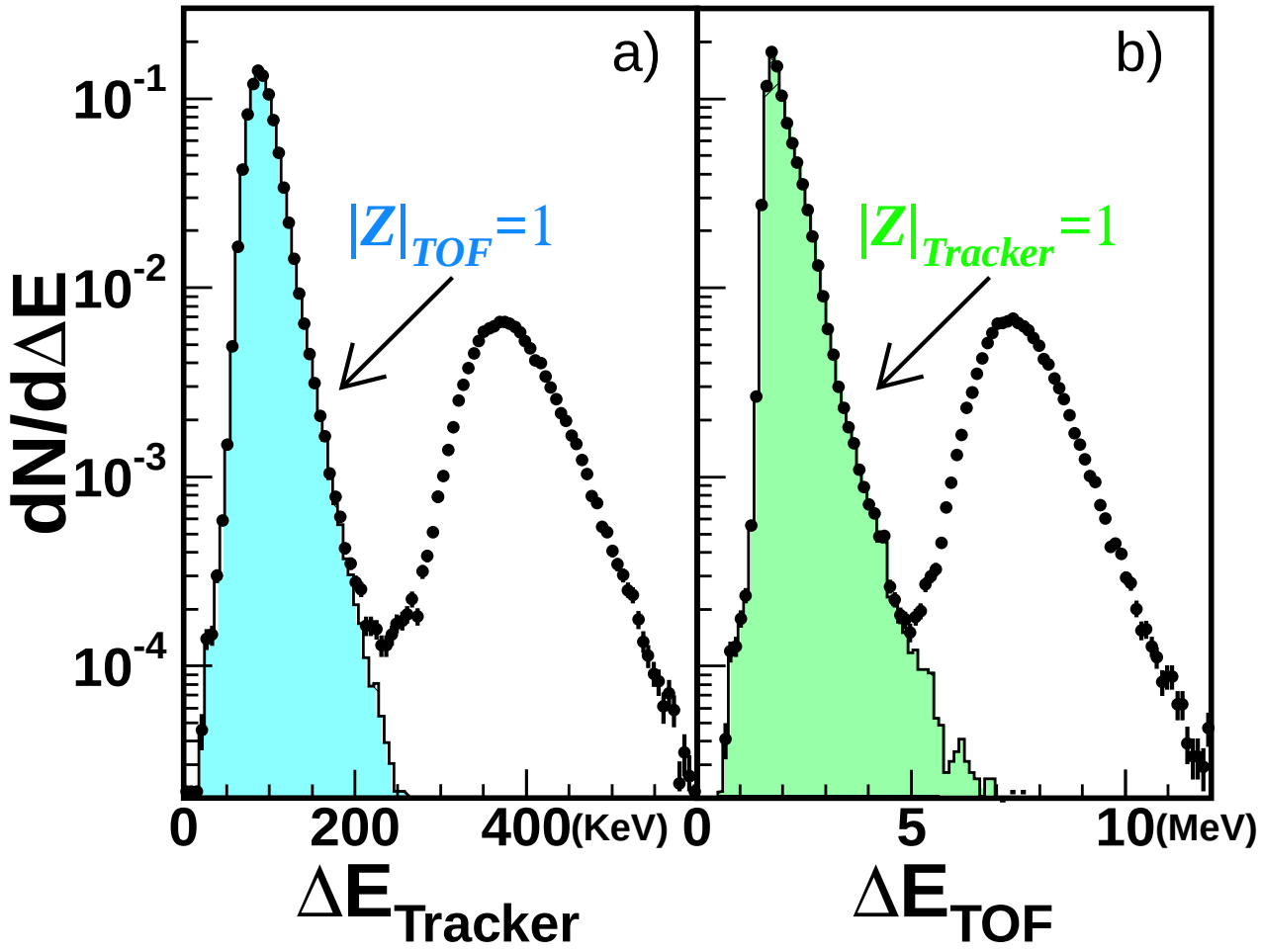

Figure 4: Energy loss measurements (points) are made independently in the tracker (a) and TOF (b) for $|Z| \leq 2$ events. The filled histogram shows which events were assigned to be $|Z| = 1$ by the other detector.

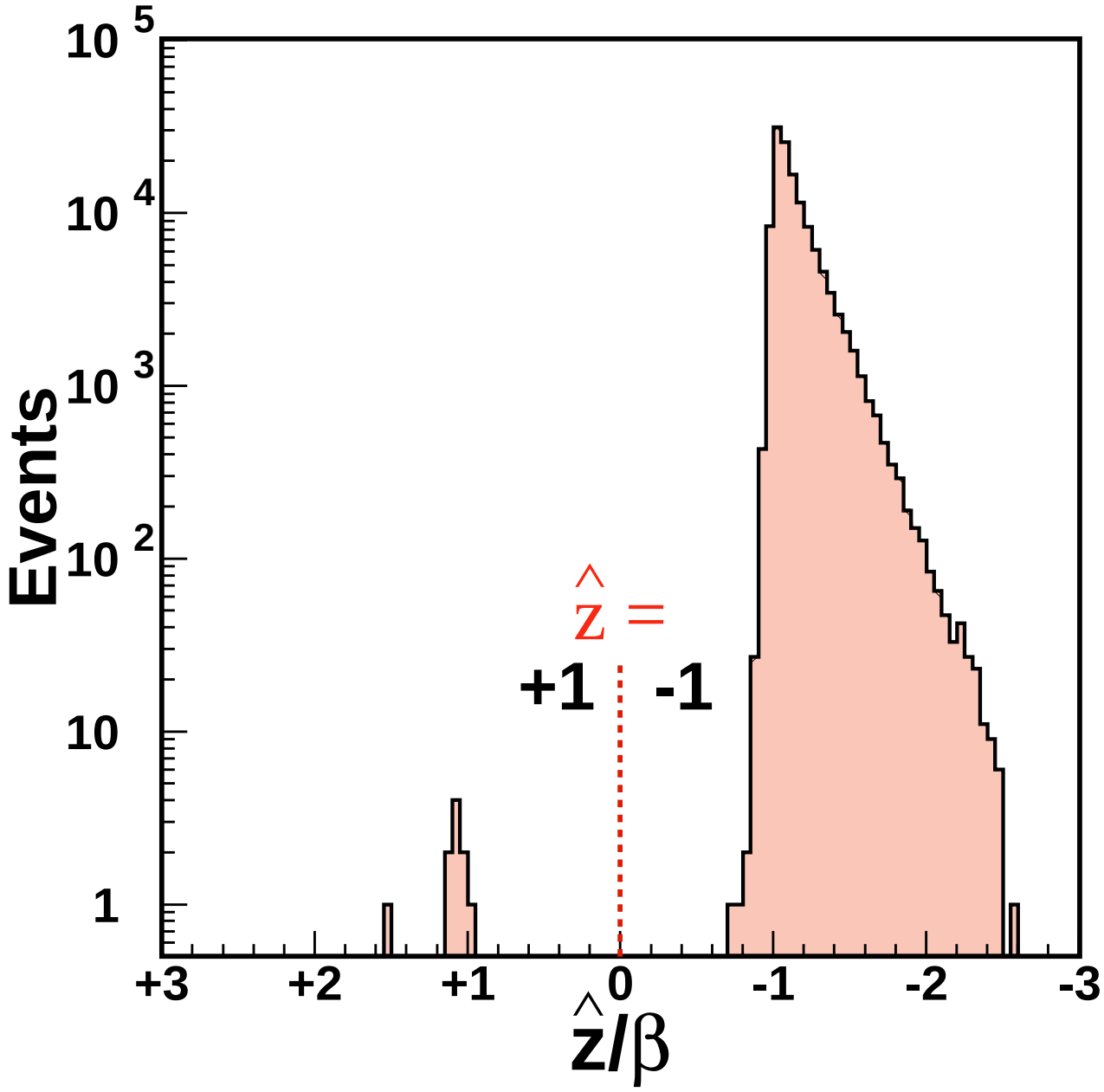

Figure 5: A typical direction, $\hat{z}/\beta$, distribution for $|Z| = 2$ events. As seen, the $\hat{z} = +1$ (or upward) and $\hat{z} = -1$ (or downward) populations are clearly separated.

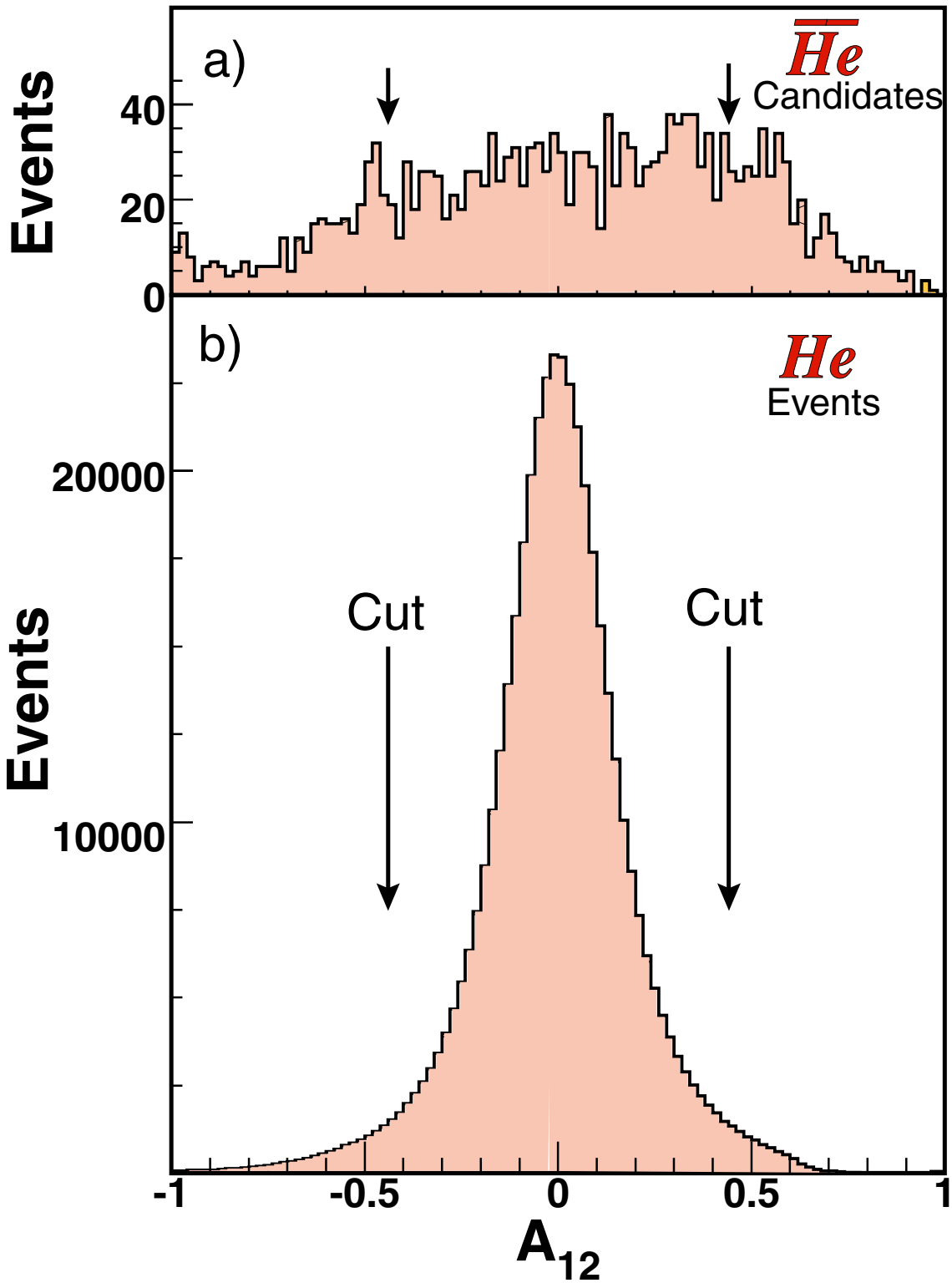

Figure 6: The asymmetry, $A_{12} = (R_1 - R_2)/(R_1 + R_2)$, of the rigidity measurements using the first, R_1, and last, R_2, three hits along the track for $|Z| = 2$ events. Also shown are the cuts used. As seen the A_{12} cuts reject much of the large angle scattering events (a). The cuts do not reject the genuine signal (b).

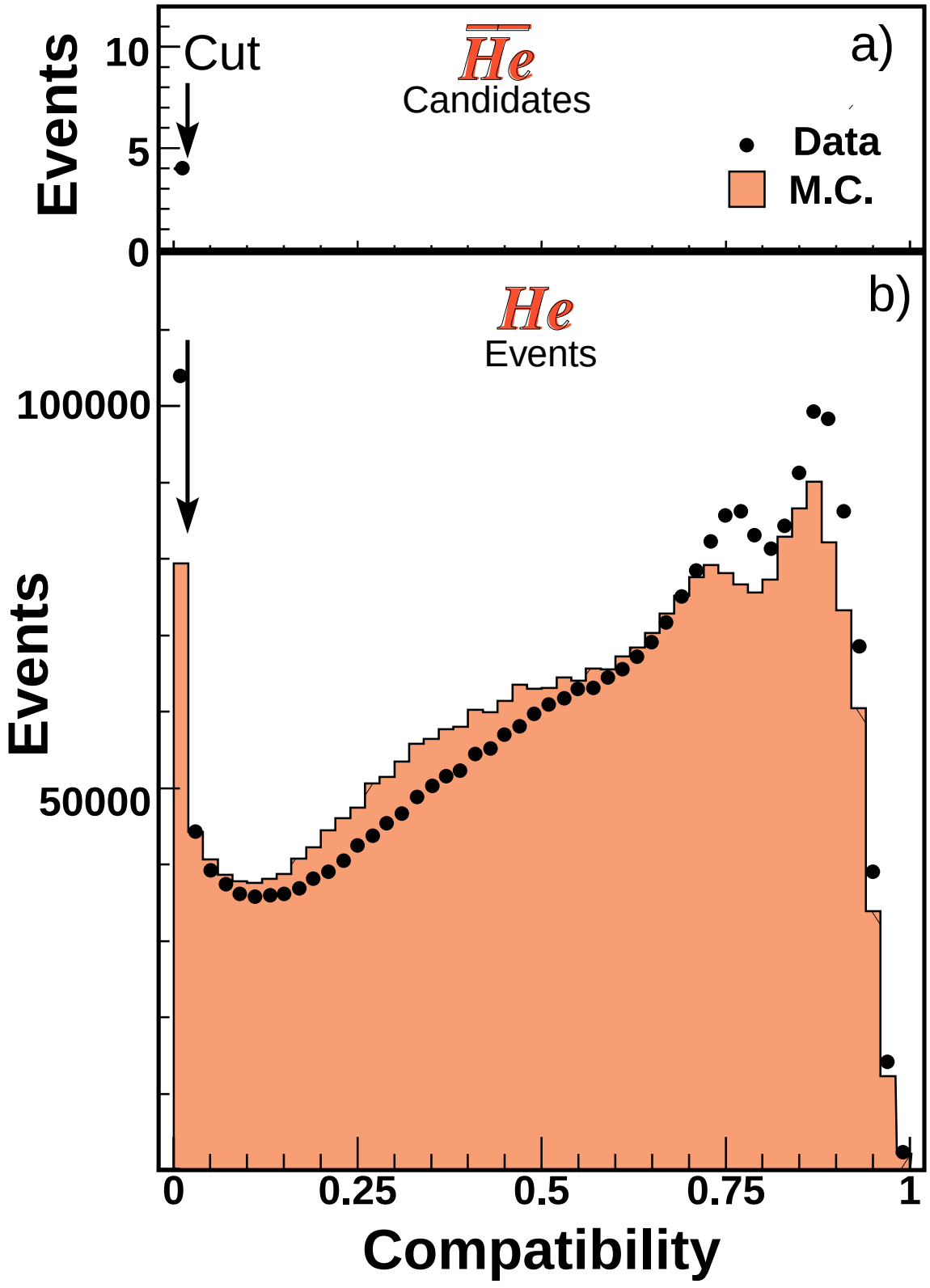

Figure 7: (a) Compatibility of the measured event parameters, β, R and $|Z|$, to be an $\overline{\text{He}}$ nucleus. (b) Compatibility to be a He nucleus. The hatched histogram is the Monte Carlo prediction for He nuclei.

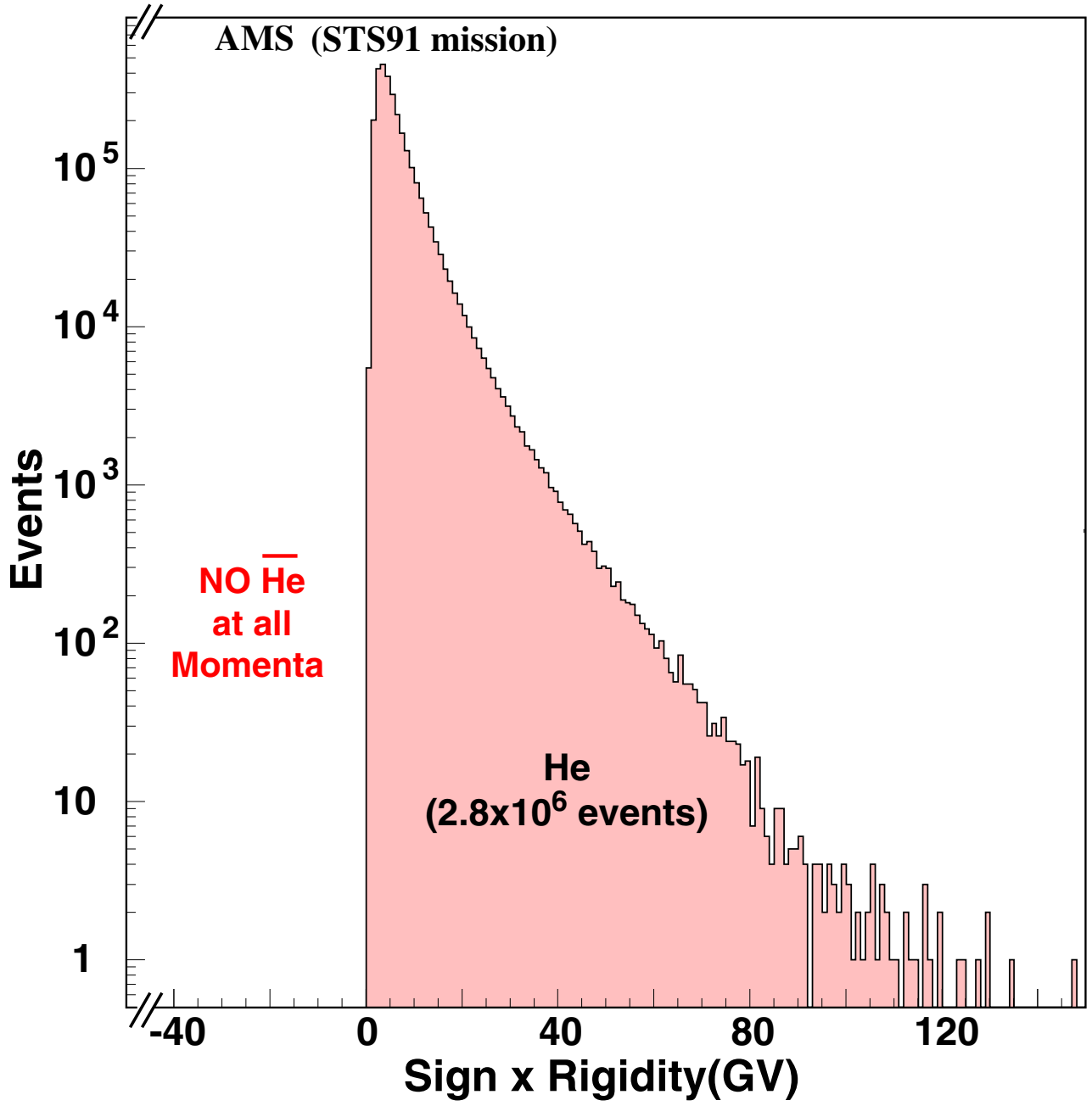

Figure 8: Measured rigidity times the charge sign for selected $|Z| = 2$ events.

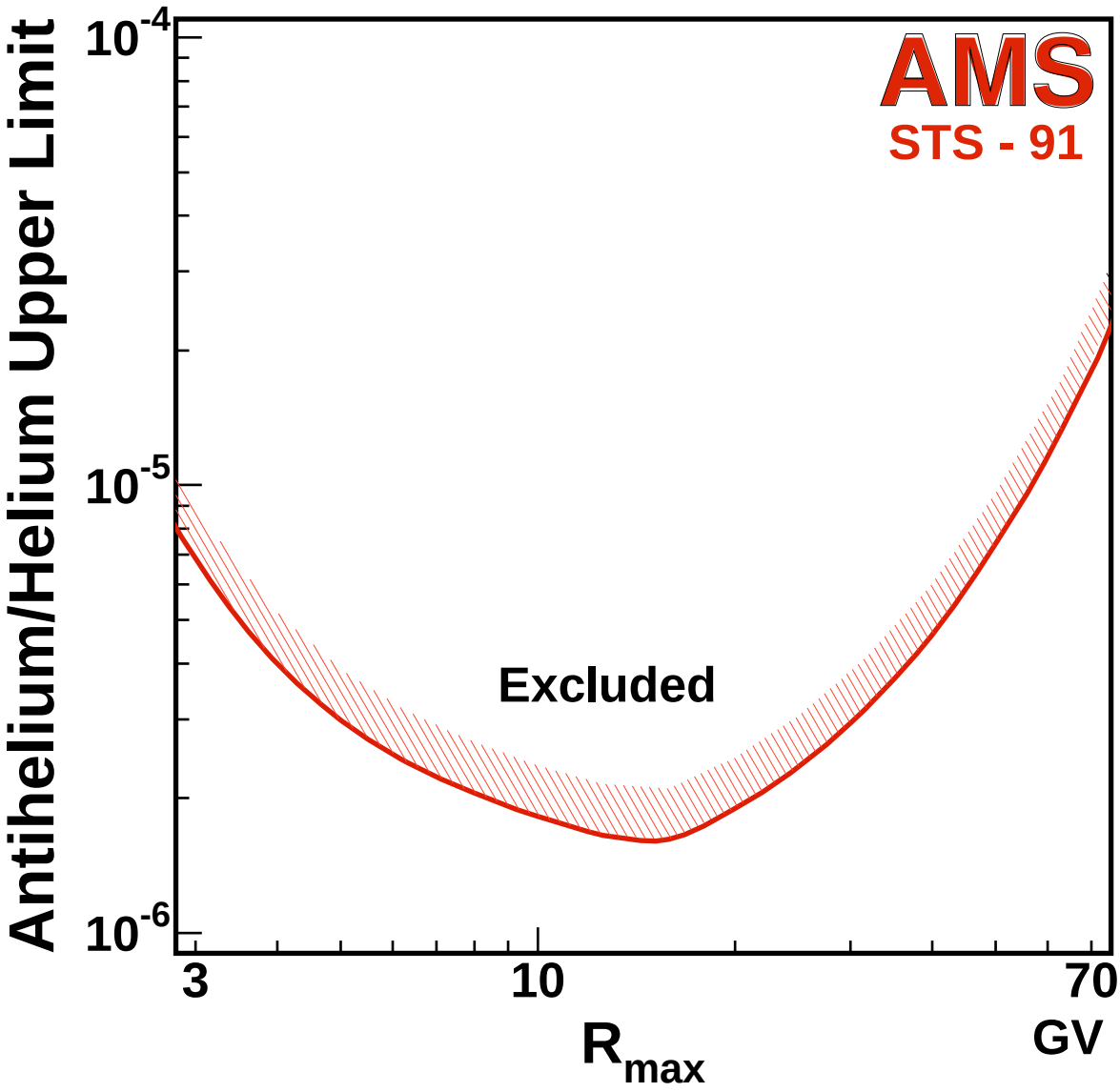

Figure 9: Upper limits on the relative flux of antihelium to helium, at the 95% confidence level, as a function of the rigidity interval R = 1.6 GV to R_{max}. These results are independent of the incident antihelium spectra.

Attachment II

Protons in Near Earth Orbit

The AMS Collaboration

Abstract

The proton spectrum in the kinetic energy range 0.1 to 200 GeV was measured by the Alpha Magnetic Spectrometer (AMS) during space shuttle flight STS–91 at an altitude of 380 km. Above the geomagnetic cutoff the observed spectrum is parameterized by a power law. Below the geomagnetic cutoff a substantial second spectrum was observed concentrated at equatorial latitudes with a flux ~70 $m^{-2}sec^{-1}sr^{-1}$. Most of these second spectrum protons follow a complicated trajectory and originate from a restricted geographic region.

Published in Phys. Lett. B472 (26 Jan 2000) 215-226

Referee's report attached.

Introduction

Protons are the most abundant charged particles in space. The study of cosmic ray protons improves the understanding of the interstellar propagation and acceleration of cosmic rays.

There are three distinct regions in space where protons have been studied by different means:

- The altitudes of 30–40 km above the Earth's surface. This region has been studied with balloons for several decades. Balloon experiments have made important contributions to the understanding of the primary cosmic ray spectrum of protrons and the behavior of atmospheric secondary particles in the upper layer of the atmosphere.

- The inner and outer radiation belts, which extend from altitudes of about 1000 km up to the boundary of the magnetosphere. Small size detectors on satellites have been sufficient to study the high intensities in the radiation belts.

- A region intermediate between the top of the atmosphere and the inner radiation belt. The radiation levels are normally not very high, so satellite-based detectors used so far, *i.e.* before AMS, have not been sensitive enough to systematically study the proton spectrum in this region over a broad energy range.

Reference [1] includes some of the previous studies. The primary feature in the proton spectrum observed near Earth is a low energy drop off in the flux, known as the geomagnetic cutoff. This cutoff occurs at kinetic energies ranging from ~10 MeV to ~10 GeV depending on the latitude and longitude. Above cutoff, from ~10 to ~100 GeV, numerous measurements indicate the spectrum falls off according to a power law.

The Alpha Magnetic Spectrometer (AMS) [2] is a high energy physics experiment scheduled for installation on the International Space Station. In preparation for this long duration mission, AMS flew a precursor mission on board the space shuttle Discovery during flight STS–91 in June 1998. In this report we use the data collected during the flight to study the cosmic ray proton spectrum from kinetic energies of 0.1 to 200 GeV, taking advantage of the large acceptance, the accurate momentum resolution, the precise trajectory reconstruction and the good particle identification capabilities of AMS.

The high statistics (~ 10^7) available allow the variation of the spectrum with position to be measured both above and below the geomagnetic cutoff. Because the incident particle direction and momentum were accurately measured in AMS, it is possible to investigate the origin of protons below cutoff by tracking them in the Earth's magnetic field.

The AMS Detector

The major elements of AMS as flown on STS–91 consisted of a permanent magnet, a tracker, time of flight hodoscopes, a Cerenkov counter and anticoincidence counters [3]. The permanent magnet had the shape of a cylindrical shell with inner diameter 1.1 m, length 0.8 m and provided a central dipole field of 0.14 Tesla across the magnet bore and an analysing power, BL^2, of 0.14 Tm^2 parallel to the magnet, or z–, axis. The six layers of double sided silicon tracker were arrayed transverse to the magnet axis. The outer layers were just outside the magnet cylinder. The tracker measured the trajectory of relativistic singly charged particles with an accuracy of 20 microns in the bending coordinate and 33 microns in the non-bending coordinate, as well as providing multiple measurements of the energy loss. The time of flight system had two planes at each end of the magnet, covering the

outer tracker layers. Together the four planes measured singly charged particle transit times with an accuracy of 120 psec and also yielded multiple energy loss measurements. The Aerogel Cerenkov counter ($n = 1.035$) was used to make independent velocity measurements to separate low energy protons from pions and electrons. A layer of anticoincidence scintillation counters lined the inner surface of the magnet. Low energy particles were absorbed by thin carbon fiber shields. In flight the AMS positive z–axis pointed out of the shuttle payload bay.

For this study the acceptance was restricted to events with an incident angle within 32° of the positive z–axis of AMS and data from two periods are included. In the first period the z–axis was pointing within 1° of the zenith. Events from this period are referred to as "downward" going. In the second period the z–axis pointing was within 1° of the nadir. Data from this period are referred to as "upward" going. The orbital inclination was 51.7° and the geodetic altitude during these two periods ranged from 350 to 390 km. Data taken while orbiting in or near the South Atlantic Anomaly were excluded.

The response of the detector was simulated using the AMS detector simulation program, based on the GEANT package [4]. The effects of energy loss, multiple scattering, interactions, decays and the measured detector efficiency and resolution were included.

The AMS detector was extensively calibrated at two accelerators: at GSI, Darmstadt, with helium and carbon beams at 600 incident angles and locations and 10^7 events, and at the CERN proton-synchrotron in the energy region of 2 to 14 GeV, with 1200 incident angles and locations and 10^8 events. This ensured that the performance of the detector and the analysis procedure were thoroughly understood.

Analysis

Reconstruction of the incident particle type, energy and direction started with a track finding procedure which included cluster finding, cluster coordinate transformation and pattern recognition. The track was then fit using two independent algorithms [5, 6]. For a track to be accepted the fit was required to include at least 4 hits in the bending plane and at least 3 hits in the non-bending plane.

The track was then extrapolated to each time of flight plane and matched with the nearest hit if it was within 60 mm. Matched hits were required in at least three of the four time of flight planes. The velocity, $\beta = v/c$, was then obtained using this time of flight information and the trajectory. For events which passed through the Cerenkov counter sensitive volume an independent velocity measurement, β_C, was also determined. To obtain the magnitude of the particle charge, $|Z|$, a set of reference distributions of energy losses in both the time of flight and the tracker layers were derived from calibration measurements made at the CERN test beam interpolated via the Monte Carlo method. For each event these references were fit to the measured energy losses using a maximum likelihood method. The track parameters were then refit with the measured β and Z and the particle type determined from the resultant Z, β, β_C and rigidity, $R = pc/|Z|e$ (GV).

As protons and helium nuclei are the dominant components in cosmic rays, after selecting events with $Z = +1$ the proton sample has only minor backgrounds which consist of charged pions and deuterons. The estimated fraction of charged pions, which are produced in the top part of AMS, with energy below 0.5 GeV is 1 %. Above this energy the fraction decreases rapidly with increasing energy. The deuteron abundance in cosmic rays above the geomagnetic cutoff is about 2 %. To remove low energy charged pions and deuterons the measured mass was required to be within 3 standard deviations of the proton mass. This rejected about 3 % of the events while reducing the background contamination to negligible levels over all energies.

To determine the differential proton fluxes from the measured counting rates requires the acceptance to be known as a function of the proton momentum and direction. Protons with different momenta and directions were generated via the Monte Carlo method, passed through the AMS detector simulation program and accepted if the trigger and reconstruction requirements were satisfied as for the data. The acceptance was found to be $0.15\,m^2sr$ on average, varying from 0.3 to $0.03\,m^2sr$ with incident angle and location and only weakly momentum dependent. These acceptances were then corrected following an analysis of unbiased trigger events. The corrections to the central value are shown in Table 1 together with their contribution to the total systematic error of 5 %.

Correction	Amount	Uncertainty
Trigger:		
4–Fold Coincidence	−3	1.5
Time of Flight Pattern	−4	2
Tracker Hits	−2	1
Anticoincidence	0	1
Analysis:		
Track and Velocity Fit	−2	1.5
Particle Interactions	+1	1.5
Proton Selection	−2	2
Monte Carlo Statistics	0	2
Differential Acceptance Binning	0	2
Total	**−12**	**5**

Table 1: Acceptance corrections and their systematic uncertainties, in percent

To obtain the incident differential spectrum from the measured spectrum, the effect of the detector resolution was unfolded using resolution functions obtained from the simulation. These functions were checked at several energy points by test beam measurements. The data were unfolded using a method based on Bayes' theorem [7, 8], which used an iterative procedure (and not a "regularized unfolding") to overcome instability of the matrix inversion due to negative terms. Fig. 1 compares the differential proton spectrum before and after unfolding in the geomagnetic equatorial region, defined below.

Results and Interpretation

The differential spectra in terms of kinetic energy for downward and upward going protons integrated over incident angles within 32° of the AMS z–axis, which was within 1° of the zenith or nadir, are presented in Fig. 2 and Tables 2–4. The results have been separated according to the absolute value of the corrected geomagnetic latitude [9], Θ_M (radians), at which they were observed. Figs. 2a, b and c clearly show the effect of the geomagnetic cutoff and the decrease in this cutoff with increasing Θ_M. The spectra above and below cutoff differ. The spectrum above cutoff is refered to as the "primary" spectrum and below cutoff as the "second" spectrum.

I. Properties of the Primary Spectrum

The primary proton spectrum may be parameterized by a power law in rigidity, $\Phi_0 \times R^{-\gamma}$. Fitting [8] the measured spectrum over the rigidity range $10 < R < 200$ GV, *i.e.* well above cutoff, yields:

$$\gamma = 2.79 \pm 0.012\,(\text{fit}) \pm 0.019\,(\text{sys}),$$

$$\Phi_0 = 16.9 \pm 0.2\,(\text{fit}) \pm 1.3\,(\text{sys}) \pm 1.5\,(\gamma)\ \frac{\text{GV}^{2.79}}{\text{m}^2\text{sec sr MV}}\ .$$

The systematic uncertainty in γ was estimated from the uncertainty in the acceptance (0.006), the dependence of the resolution function on the particle direction and track length within one sigma (0.015), variation of the tracker bending coordinate resolution by ± 4 microns (0.005) and variation of the selection criteria (0.010). The third uncertainty quoted for Φ_0 reflects the systematic uncertainty in γ.

II. Properties of the Second Spectrum

As shown in Figs. 2a, b, c, a substantial second spectrum of downward going protons is observed for all but the highest geomagnetic latitudes. Figs. 2d, e, f show that a substantial second spectrum of upward going protons is also observed for all geomagnetic latitudes. The upward and downward going protons of the second spectrum have the following unique properties:

(i) At geomagnetic equatorial latitudes, $\Theta_M < 0.2$, this spectrum extends from the lowest measured energy, 0.1 GeV, to ~6 GeV with a flux ~70 $m^{-2}sec^{-1}sr^{-1}$.

(ii) As seen in Figs. 2a, d, the second spectrum has a distinct structure near the geomagnetic equator: a change in geomagnetic latitude from 0 to 0.3 causes the proton flux to drop by a factor of 2 to 3 depending on the energy.

(iii) Over the much wider interval $0.3 < \Theta_M < 0.8$, the flux is nearly constant.

(iv) In the range $0 \leq \Theta_M < 0.8$, detailed comparison in different latitude bands (Fig. 3) indicates that the upward and downward fluxes are nearly identical, agreeing within 1 %.

(v) At polar latitudes, $\Theta_M > 1.0$, the downward second spectrum (Fig. 2c) is gradually obscured by the primary spectrum, whereas the second spectrum of upward going protons (Fig. 2f) is clearly observed.

To understand the origin of the second spectrum, we traced [10] back 10^5 protons from their measured incident angle, location and momentum, through the geomagnetic field [11] for 10 sec flight time or until they impinged on the top of the atmosphere at an altitude of 40 km, which was taken to be the point of origin. All second spectrum protons were found to originate in the atmosphere, except for few percent of the total detected near the South Atlantic Anomaly (SAA). These had closed trajectories and hence may have been circulating for a very long time and it is obviously difficult to trace back to thier origin. This type of trajectory was only observed near the SAA, clearly influenced by the inner radiation belt. To avoid confusion data taken in the SAA region were excluded though the rest of the protons detected near the SAA had characteristics as the rest of the sample. Defining the flight time as the interval between production and detection, Fig. 4 shows the distribution of momentum versus flight time of the remaining protons.

As seen in Fig. 4, the trajectory tracing shows that about 30 % of the detected protons flew for less than 0.3 sec before detection. The origin of these "short–lived" protons is distributed uniformly around the globe, see Fig. 5a, the apparent structure reflecting the orbits of the space shuttle. In contrast, Fig. 5b shows that the remaining 70 % of protons with flight times greater than 0.3 sec, classified as "long–lived", originate from a geographically restricted zone. Fig. 6 shows the strongly peaked distribution of the point of origin of these long–lived protons in geomagnetic coordinates. Though data is presented only for protons detected at $\Theta_M < 0.3$, these general features hold true up to $\Theta_M \sim 0.7$. Fig. 7 shows the distribution of the number of geomagnetic equator crossings for long–lived and short–lived protons. About 15 % of all the second spectrum protons were detected on their first bounce over the geomagnetic equator.

The measurements by AMS in near Earth orbit (at 380 km from the Earth's surface), between the atmosphere and the radiation belt, show that the particles in this region follow a complicated path in the Earth's magnetic field. This behavior is different from that extrapolated from satellite observations in the radiation belts, where the protons bounce across the equator for a much longer time. It is also different from that extrapolated from balloon observations in the upper layer of the atmosphere, where the protons typically cross the equator once. A striking feature of the second spectrum is that most of the protons originate from a restricted geographic region.

Acknowledgements

The support of INFN, Italy, ETH–Zürich, the University of Geneva, the Chinese Academy of Sciences, Academia Sinica and National Central University, Taiwan, the RWTH–Aachen, Germany, the University of Turku, the University of Technology of Helsinki, Finland, the U.S. DOE and M.I.T., CIEMAT, Spain, LIP, Portugal and IN2P3, France, is gratefully acknowledged.

We thank Professors S. Ahlen, C. Canizares, A. De Rujula, J. Ellis, A. Guth, M. Jacob, L. Maiani, R. Mewaldt, R. Orava, J. F. Ormes and M. Salamon for helping us to initiate this experiment.

The success of the first AMS mission is due to many individuals and organizations outside of the collaboration. The support of NASA was vital in the inception, development and operation of the experiment. The dedication of Douglas P. Blanchard, Mark J. Sistilli, James R. Bates, Kenneth Bollweg and the NASA and Lockheed–Martin Mission Management team, the support of the Max–Plank Institute for Extraterrestrial Physics, the support of the space agencies from Germany (DLR), Italy (ASI), France (CNES) and China and the support of CSIST, Taiwan, made it possible to complete this experiment on time.

The support of CERN and GSI–Darmstadt, particularly of Professor Hans Specht and Dr. Reinhard Simon made it possible for us to calibrate the detector after the shuttle returned from orbit.

The back tracing was made possible by the work of Professors E. Flückiger, D. F. Smart and M. A. Shea.

We are most grateful to the STS–91 astronauts, particularly to Dr. Franklin Chang–Diaz who provided vital help to AMS during the flight.

References

[1] Stanley C. Freden and R. Stephen White, Phys. Rev. Lett. **3** (1959) 9; S.D. Verma, J. Geophys. Res. **72** (1967) 915; B.J. Teegarden, J. Geophys. Res. **72** (1967) 4857; M.J. Ryan, Phys. Rev. Lett. **15** (1972) 985; L.H. Smith *et al.*, ApJ **180** (1973) 987; G.F. Smoot *et al.*, J. Geophys. Res. **10** (1973) 730; W.R. Webber *et al.*, Proc. 20th ICRC **1** (1987) 325; R.E. Steitmatter *et al.*, Proc. 21st ICRC **3** (1990) 277; F.B. McDonald *et al.*, Proc. 21st ICRC **6** (1990) 144; E.S. Seo *et al.*, ApJ **378** (1991) 763; M. Ichimura *et al.*, Phys. Rev. **D48** (1993) 1949; Papini *et al.*, Proc. 23rd ICRC **1** (1993) 579; J. Chen *et al.*, Adv. Space Res. **14** (1994) (10)765; S.P. Swordy *et al.*, Proc. 24th ICRC **2** (1995) 652; W. Menn *et al.*, Proc. 25th ICRC **3** (1997) 409; M. Boesio *et al.*, The Cosmic Ray Proton and Helium Spectra Between 0.2 and 200 GV, INFN/AE 98/06 (1998); B. Wiebel-Sooth, P.L. Biermann and H. Meyer, A&A **330** (1998) 389.

[2] S. Ahlen *et al.*, Nucl. Inst. Meth. **A350** (1994) 351.

[3] AMS Collaboration, The Construction of the Alpha Magnetic Spectrometer, Nucl. Inst. Meth., in preperation G.M. Viertel, M. Capell, Nucl. Inst. Meth. **A419** (1998) 295–299; AMS Collaboration, J. Alcaraz *et al.*, Phys. Lett. **B461** (1999) 387–396; .

[4] R. Brun *et al.*, GEANT 3, CERN DD/EE/84-1 (Revised, 1987); P.A. Aamio *et al.*, FLUKA Users Guide, CERN TIS-RP-190 (1990).

[5] V. Innocente, M. Maire and E. Nagy, GEANE: Average Tracking and Error Propagation Package, CERN Program Library W5013-E (1991).

[6] J.C. Hart and D.H. Saxon, Nucl. Inst. Meth. **220** (1984) 309.

[7] A. Kondor, Nucl. Inst. Meth. **216** (1983) 177; G. D'Agostini, Nucl. Inst. Meth. **A362** (1995) 487.

[8] V. Blobel, Unfolding Methods in High Energy Physics, in Proc. 1984 CERN School of Computing, CERN 85-09 (1985) 88–127.

[9] A. Brekke, Physics of the Upper Polar Atmosphere, pp. 127–145, (Wiley, 1997).

[10] E.O. Flückiger *et al.*, Proc. 22nd ICRC **3** (1991) 648–651; E. Kobel, Zu den magnetosphaerischen Effekten der kosmischen Strahlung, Ph.D. thesis, University of Bern, 1992.

[11] N.A. Tsyganenko and A.V. Usmanov, Planet. Space Sci. **30** (1982) 985–998; N.A. Tsyganenko *et al.*, Software for Computations of Geomagnetic Field and Related Coordinate Systems, Soviet Geophysical Committee, Special Report (1987); N.A. Tsyganenko, Planet. Space Sci. **35** (1987) 1347–1358; N.A. Tsyganenko, Planet. Space Sci. **37** (1989) 5–20; N.A. Tsyganenko, J. Geophys. Res. **100** (1995) 5599–5612; N.A. Tsyganenko and D.P. Stern, J. Geophys. Res. **101** (1996) 27187–27198; R.L. Langel, Chairman, IAGA Div. V working group 8, J. Geomag. Geoelectr. **47** (1995) 1251–1261; G. Gustafsson, N.E. Papitashvili and V.O. Papitashvili, J. Atmos. Terr. Phys. **54** (1992) 1609–1631.

The AMS Collaboration

J.Alcaraz[y], D.Alvisi[j], B.Alpat[ac], G.Ambrosi[r], H.Anderhub[ag], L.Ao[g], A.Arefiev[ab], P.Azzarello[r], E.Babucci[ac], L.Baldini[j,l], M.Basile[j], D.Barancourt[s], F.Barao[w,v], G.Barbier[s], G.Barreira[w], R.Battiston[ac], R.Becker[l], U.Becker[l], L.Bellagamba[j], P.Béné[r], J.Berdugo[y], P.Berges[l], B.Bertucci[ac], A.Biland[ag], S.Bizzaglia[ac], S.Blasko[ac], G.Boella[z], M.Boschini[z], M.Bourquin[r], G.Bruni[j], M.Buenerd[s], J.D.Burger[l], W.J.Burger[ac], X.D.Cai[l], R.Cavalletti[j], C.Camps[b], P.Cannarsa[ag], M.Capell[l], D.Casadei[j], J.Casaus[y], G.Castellini[p], Y.H.Chang[m], H.F.Chen[t], H.S.Chen[i], Z.G.Chen[g], N.A.Chernoplekov[aa], A.Chiarini[j], T.H.Chiueh[m], Y.L.Chuang[ad], F.Cindolo[j], V.Commichau[b], A.Contin[j], A.Cotta–Ramusino[j], P.Crespo[w], M.Cristinziani[r], J.P.da Cunha[n], T.S.Dai[l], J.D.Deus[y], N.Dinu[ac,1], L.Djambazov[ag], I.D'Antone[j], Z.R.Dong[h], P.Emonet[r], J.Engelberg[u], F.J.Eppling[l], T.Eronen[af], G.Esposito[ac], P.Extermann[r], J.Favier[c], C.C.Feng[x], E.Fiandrini[ac], F.Finelli[j], P.H.Fisher[l], R.Flaminio[c], G.Fluegge[b], N.Fouque[c], Yu.Galaktionov[ab,l], M.Gervasi[z], P.Giusti[j], D.Grandi[z], W.Q.Gu[h], K.Hangarter[b], A.Hasan[ag], V.Hermel[c], H.Hofer[ag], M.A.Huang[ad], W.Hungerford[ag], M.Ionica[ac,1], R.Ionica[ac,1], M.Jongmanns[ag], K.Karlamaa[u], W.Karpinski[a], G.Kenney[ag], J.Kenny[ac], W.Kim[ae], A.Klimentov[l,ab], R.Kossakowski[c], V.Koutsenko[l,ab], G.Laborie[s], T.Laitinen[af], G.Lamanna[ac], G.Laurenti[j], A.Lebedev[l], S.C.Lee[ad], G.Levi[j], P.Levtchenko[ac,2], C.L.Liu[x], H.T.Liu[i], M.Lolli[j], I.Lopes[n], G.Lu[g], Y.S.Lu[i], K.Lübelsmeyer[a], D.Luckey[l], W.Lustermann[ag], C.Maña[y], A.Margotti[j], F.Massera[j], F.Mayet[s], R.R.McNeil[e], B.Meillon[s], M.Menichelli[ac], F.Mezzanotte[j], R.Mezzenga[ac], A.Mihul[k], G.Molinari[j], A.Mourao[v], A.Mujunen[u], F.Palmonari[j], G.Pancaldi[j], A.Papi[ac], I.H.Park[ae], M.Pauluzzi[ac], F.Pauss[ag], E.Perrin[r], A.Pesci[j], A.Pevsner[d], R.Pilastrini[j], M.Pimenta[w,v], V.Plyaskin[ab], V.Pojidaev[ab], H.Postema[l,3], V.Postolache[ac,1], E.Prati[j], N.Produit[r], P.G.Rancoita[z], D.Rapin[r], F.Raupach[a], S.Recupero[j], D.Ren[ag], Z.Ren[ad], M.Ribordy[r], J.P.Richeux[r], E.Riihonen[af], J.Ritakari[u], U.Roeser[ag], C.Roissin[s], R.Sagdeev[o], D.Santos[s], G.Sartorelli[j], A.Schultz von Dratzig[a], G.Schwering[a], E.S.Seo[o], V.Shoutko[l], E.Shoumilov[ab], R.Siedling[a], D.Son[ae], T.Song[h], M.Steuer[l], G.S.Sun[h], H.Suter[ag], X.W.Tang[i], Samuel C.C.Ting[l], S.M.Ting[l], M.Tornikoski[u], G.Torromeo[j], J.Torsti[af], J.Trümper[q], J.Ulbricht[ag], S.Urpo[u], I.Usoskin[z], E.Valtonen[af], J.Vandenhirtz[a], F.Velcea[ac,1], E.Velikhov[aa], B.Verlaat[ag,4], I.Vetlitsky[ab], F.Vezzu[s], J.P.Vialle[c], G.Viertel[ag], D.Vité[r], H.Von Gunten[ag], S.Waldmeier Wicki[ag], W.Wallraff[a], B.C.Wang[x], J.Z.Wang[g], Y.H.Wang[ad], K.Wiik[u], C.Williams[j], S.X.Wu[l,m], P.C.Xia[h], J.L.Yan[g], L.G.Yan[h], C.G.Yang[i], M.Yang[i], S.W.Ye[t,5], P.Yeh[ad], Z.Z.Xu[t], H.Y.Zhang[f], Z.P.Zhang[t], D.X.Zhao[h], G.Y.Zhu[i], W.Z.Zhu[g], H.L.Zhuang[i], A.Zichichi[j].

---

[a] I. Physikalisches Institut, RWTH, D-52056 Aachen, Germany[6]

[b] III. Physikalisches Institut, RWTH, D-52056 Aachen, Germany[6]

[c] Laboratoire d'Annecy-le-Vieux de Physique des Particules, LAPP, F-74941 Annecy-le-Vieux CEDEX, France

[e] Louisiana State University, Baton Rouge, LA 70803, USA

[d] Johns Hopkins University, Baltimore, MD 21218, USA

[f] Center of Space Science and Application, Chinese Academy of Sciences, 100080 Beijing, China

[g] Chinese Academy of Launching Vehicle Technology, CALT, 100076 Beijing, China

[h] Institute of Electrical Engineering, IEE, Chinese Academy of Sciences, 100080 Beijing, China

[i] Institute of High Energy Physics, IHEP, Chinese Academy of Sciences, 100039 Beijing, China[7]

[j] University of Bologna and INFN-Sezione di Bologna, I-40126 Bologna, Italy

[k] Institute of Microtechnology, Politechnica University of Bucharest and University of Bucharest, R-76900 Bucharest, Romania

[l] Massachusetts Institute of Technology, Cambridge, MA 02139, USA

[m] National Central University, Chung-Li, Taiwan 32054

[n] Laboratorio de Instrumentacao e Fisica Experimental de Particulas, LIP, P-3000 Coimbra, Portugal

[o] University of Maryland, College Park, MD 20742, USA

[p] INFN Sezione di Firenze, I-50125 Florence, Italy

[q] Max–Plank Institut fur Extraterrestrische Physik, D-85740 Garching, Germany
[r] University of Geneva, CH-1211 Geneva 4, Switzerland
[s] Institut des Sciences Nucleaires, F-38026 Grenoble, France
[t] Chinese University of Science and Technology, USTC, Hefei, Anhui 230 029, China[7]
[u] Helsinki University of Technology, FIN-02540 Kylmala, Finland
[v] Instituto Superior Técnico, IST, P-1096 Lisboa, Portugal
[w] Laboratorio de Instrumentacao e Fisica Experimental de Particulas, LIP, P-1000 Lisboa, Portugal
[x] Chung–Shan Institute of Science and Technology, Lung-Tan, Tao Yuan 325, Taiwan 11529
[y] Centro de Investigaciones Energéticas, Medioambientales y Tecnologícas, CIEMAT, E-28040 Madrid, Spain[8]
[z] INFN-Sezione di Milano, I-20133 Milan, Italy
[aa] Kurchatov Institute, Moscow, 123182 Russia
[ab] Institute of Theoretical and Experimental Physics, ITEP, Moscow, 117259 Russia
[ac] INFN-Sezione di Perugia and Universitá Degli Studi di Perugia, I-06100 Perugia, Italy[9]
[ad] Academia Sinica, Taipei, Taiwan
[ae] Kyungpook National University, 702-701 Taegu, Korea
[af] University of Turku, FIN-20014 Turku, Finland
[ag] Eidgenössische Technische Hochschule, ETH Zürich, CH-8093 Zürich, Switzerland
[1] Permanent address: HEPPG, Univ. of Bucharest, Romania.
[2] Permanent address: Nuclear Physics Institute, St. Petersburg, Russia.
[3] Now at European Laboratory for Particle Physics, CERN, CH-1211 Geneva 23, Switzerland.
[4] Now at National Institute for High Energy Physics, NIKHEF, NL-1009 DB Amsterdam, The Netherlands.
[5] Supported by ETH Zürich.
[6] Supported by the Deutsches Zentrum für Luft– und Raumfahrt, DLR.
[7] Supported by the National Natural Science Foundation of China.
[8] Supported also by the Comisión Interministerial de Ciencia y Tecnología.
[9] Also supported by the Italian Space Agency.

Downward Proton Flux $(m^2\,sec\,sr\,MeV)^{-1}$						
E_{kin} (GeV)		Geomagnetic Latitude Range				
		$\Theta_M < 0.2$	$0.2 \le \Theta_M < 0.3$	$0.3 \le \Theta_M < 0.4$	$0.4 \le \Theta_M < 0.5$	$0.5 \le \Theta_M < 0.6$
0.07 –	0.10	$(16.7\pm4.4)\times10^{-2}$	$(14.2\pm4.0)\times10^{-2}$	$(11.2\pm3.1)\times10^{-2}$	$(13.6\pm3.8)\times10^{-2}$	$(13.4\pm3.6)\times10^{-2}$
0.10 –	0.15	$(12.1\pm1.4)\times10^{-2}$	$(8.2\pm1.0)\times10^{-2}$	$(7.6\pm1.0)\times10^{-2}$	$(7.6\pm1.0)\times10^{-2}$	$(7.7\pm1.0)\times10^{-2}$
0.15 –	0.22	$(97.9\pm4.6)\times10^{-3}$	$(51.2\pm3.2)\times10^{-3}$	$(41.9\pm2.6)\times10^{-3}$	$(44.6\pm3.0)\times10^{-3}$	$(48.4\pm3.3)\times10^{-3}$
0.22 –	0.31	$(86.2\pm2.8)\times10^{-3}$	$(45.6\pm1.8)\times10^{-3}$	$(37.9\pm1.7)\times10^{-3}$	$(34.4\pm1.5)\times10^{-3}$	$(32.7\pm1.6)\times10^{-3}$
0.31 –	0.44	$(70.1\pm3.2)\times10^{-3}$	$(34.6\pm1.5)\times10^{-3}$	$(24.4\pm1.1)\times10^{-3}$	$(21.1\pm1.2)\times10^{-3}$	$(20.2\pm1.2)\times10^{-3}$
0.44 –	0.62	$(50.4\pm2.7)\times10^{-3}$	$(21.2\pm1.2)\times10^{-3}$	$(155.\pm9.3)\times10^{-4}$	$(121.\pm9.3)\times10^{-4}$	$(113.\pm9.0)\times10^{-4}$
0.62 –	0.85	$(32.8\pm1.9)\times10^{-3}$	$(116.\pm6.8)\times10^{-4}$	$(84.9\pm6.5)\times10^{-4}$	$(61.5\pm5.6)\times10^{-4}$	$(50.0\pm6.4)\times10^{-4}$
0.85 –	1.15	$(20.6\pm1.2)\times10^{-3}$	$(57.2\pm4.7)\times10^{-4}$	$(40.0\pm3.8)\times10^{-4}$	$(26.9\pm3.4)\times10^{-4}$	$(24.2\pm4.2)\times10^{-4}$
1.15 –	1.54	$(116.\pm6.9)\times10^{-4}$	$(28.6\pm3.3)\times10^{-4}$	$(17.7\pm2.5)\times10^{-4}$	$(12.7\pm2.9)\times10^{-4}$	$(8.5\pm1.4)\times10^{-4}$
1.54 –	2.02	$(66.9\pm4.2)\times10^{-4}$	$(12.2\pm2.1)\times10^{-4}$	$(8.5\pm2.6)\times10^{-4}$	$(6.9\pm1.4)\times10^{-4}$	$(5.7\pm1.0)\times10^{-4}$
2.02 –	2.62	$(28.6\pm1.9)\times10^{-4}$	$(8.2\pm1.8)\times10^{-4}$	$(5.0\pm1.3)\times10^{-4}$	$(37.3\pm3.3)\times10^{-5}$	$(34.2\pm1.5)\times10^{-5}$
2.62 –	3.38	$(110.\pm9.6)\times10^{-5}$	$(3.6\pm1.1)\times10^{-4}$	$(30.0\pm8.6)\times10^{-5}$	$(204.\pm7.4)\times10^{-6}$	$(29.0\pm1.4)\times10^{-5}$
3.38 –	4.31	$(44.3\pm7.9)\times10^{-5}$	$(20.3\pm6.0)\times10^{-5}$	$(23.2\pm3.6)\times10^{-5}$	$(25.0\pm1.3)\times10^{-5}$	$(10.7\pm1.1)\times10^{-4}$
4.31 –	5.45	$(15.7\pm3.1)\times10^{-5}$	$(13.4\pm4.8)\times10^{-5}$	$(17.6\pm3.2)\times10^{-5}$	$(58.5\pm5.9)\times10^{-5}$	$(62.9\pm6.4)\times10^{-4}$
5.45 –	6.86	$(6.1\pm2.2)\times10^{-5}$	$(105.\pm8.7)\times10^{-6}$	$(31.9\pm2.3)\times10^{-5}$	$(32.1\pm3.0)\times10^{-4}$	$(18.4\pm1.4)\times10^{-3}$
6.86 –	8.60	$(23.7\pm2.1)\times10^{-5}$	$(53.8\pm2.7)\times10^{-5}$	$(19.5\pm1.5)\times10^{-4}$	$(96.2\pm6.4)\times10^{-4}$	$(23.3\pm1.2)\times10^{-3}$
8.60 –	10.73	$(138.\pm6.8)\times10^{-5}$	$(28.6\pm1.7)\times10^{-4}$	$(58.5\pm3.3)\times10^{-4}$	$(128.\pm5.4)\times10^{-4}$	$(193.\pm5.1)\times10^{-4}$
10.73 –	13.34	$(49.5\pm1.8)\times10^{-4}$	$(60.9\pm2.4)\times10^{-4}$	$(85.7\pm3.1)\times10^{-4}$	$(115.\pm2.8)\times10^{-4}$	$(128.\pm3.7)\times10^{-4}$
13.34 –	16.55	$(65.7\pm2.1)\times10^{-4}$	$(63.4\pm1.8)\times10^{-4}$	$(72.1\pm2.1)\times10^{-4}$	$(75.6\pm2.5)\times10^{-4}$	$(75.6\pm2.7)\times10^{-4}$
16.55 –	20.48	$(45.7\pm1.7)\times10^{-4}$	$(45.5\pm1.7)\times10^{-4}$	$(44.4\pm1.5)\times10^{-4}$	$(45.2\pm1.8)\times10^{-4}$	$(43.3\pm1.2)\times10^{-4}$
20.48 –	25.29	$(27.7\pm1.0)\times10^{-4}$	$(25.5\pm1.0)\times10^{-4}$	$(255.\pm9.8)\times10^{-5}$	$(248.\pm9.6)\times10^{-5}$	$(24.0\pm1.0)\times10^{-4}$
25.29 –	31.20	$(155.\pm5.9)\times10^{-5}$	$(147.\pm7.1)\times10^{-5}$	$(144.\pm6.8)\times10^{-5}$	$(142.\pm6.7)\times10^{-5}$	$(138.\pm5.6)\times10^{-5}$
31.20 –	38.43	$(90.5\pm4.1)\times10^{-5}$	$(79.2\pm4.7)\times10^{-5}$	$(80.5\pm4.5)\times10^{-5}$	$(80.0\pm4.3)\times10^{-5}$	$(77.1\pm4.3)\times10^{-5}$
38.43 –	47.30	$(51.4\pm2.2)\times10^{-5}$	$(48.9\pm3.0)\times10^{-5}$	$(48.2\pm2.5)\times10^{-5}$	$(48.2\pm3.0)\times10^{-5}$	$(47.1\pm2.7)\times10^{-5}$
47.30 –	58.16	$(30.0\pm1.7)\times10^{-5}$	$(28.6\pm2.0)\times10^{-5}$	$(28.7\pm1.8)\times10^{-5}$	$(28.4\pm1.8)\times10^{-5}$	$(27.7\pm1.8)\times10^{-5}$
58.16 –	71.48	$(164.\pm8.8)\times10^{-6}$	$(15.4\pm1.2)\times10^{-5}$	$(15.6\pm1.2)\times10^{-5}$	$(154.\pm8.8)\times10^{-6}$	$(149.\pm9.9)\times10^{-6}$
71.48 –	87.79	$(86.1\pm3.9)\times10^{-6}$	$(79.6\pm4.7)\times10^{-6}$	$(81.5\pm6.4)\times10^{-6}$	$(80.2\pm5.9)\times10^{-6}$	$(76.7\pm5.1)\times10^{-6}$
87.79 –	107.78	$(49.4\pm2.9)\times10^{-6}$	$(45.0\pm4.6)\times10^{-6}$	$(46.6\pm4.8)\times10^{-6}$	$(45.8\pm2.8)\times10^{-6}$	$(43.4\pm2.6)\times10^{-6}$
107.78 –	132.27	$(28.6\pm3.1)\times10^{-6}$	$(25.7\pm6.1)\times10^{-6}$	$(26.9\pm7.3)\times10^{-6}$	$(26.4\pm6.2)\times10^{-6}$	$(24.8\pm4.6)\times10^{-6}$
132.27 –	162.29	$(16.2\pm1.8)\times10^{-6}$	$(14.3\pm7.0)\times10^{-6}$	$(15.2\pm5.2)\times10^{-6}$	$(14.9\pm7.9)\times10^{-6}$	$(13.8\pm6.3)\times10^{-6}$
162.29 –	199.06	$(97.2\pm5.1)\times10^{-7}$	$(84.8\pm6.7)\times10^{-7}$	$(9.1\pm2.3)\times10^{-6}$	$(8.9\pm1.8)\times10^{-6}$	$(82.1\pm6.2)\times10^{-7}$

Table 2: Differential downward proton flux spectra for lower latitudes.

Downward Proton Flux $(m^2\,sec\,sr\,MeV)^{-1}$						
E_{kin} (GeV)		Geomagnetic Latitude Range				
		$0.6 \le \Theta_M < 0.7$	$0.7 \le \Theta_M < 0.8$	$0.8 \le \Theta_M < 0.9$	$0.9 \le \Theta_M < 1.0$	$1.0 \le \Theta_M$
0.07 –	0.10	$(12.2\pm3.5)\times10^{-2}$	$(18.5\pm5.9)\times10^{-2}$	$(25.1\pm8.9)\times10^{-2}$	$(\ 4.3\pm1.3)\times10^{-1}$	$(\ 9.2\pm2.6)\times10^{-1}$
0.10 –	0.15	$(\ 9.7\pm1.3)\times10^{-2}$	$(11.8\pm1.6)\times10^{-2}$	$(19.1\pm2.6)\times10^{-2}$	$(41.8\pm5.6)\times10^{-2}$	$(\ 9.8\pm1.2)\times10^{-1}$
0.15 –	0.22	$(66.0\pm3.7)\times10^{-3}$	$(97.3\pm5.9)\times10^{-3}$	$(144.\pm8.9)\times10^{-3}$	$(33.6\pm3.3)\times10^{-2}$	$(109.\pm6.7)\times10^{-2}$
0.22 –	0.31	$(44.4\pm1.6)\times10^{-3}$	$(44.2\pm2.0)\times10^{-3}$	$(92.4\pm6.9)\times10^{-3}$	$(22.6\pm3.9)\times10^{-2}$	$(126.\pm5.3)\times10^{-2}$
0.31 –	0.44	$(24.1\pm1.7)\times10^{-3}$	$(23.8\pm1.3)\times10^{-3}$	$(58.3\pm4.8)\times10^{-3}$	$(29.3\pm7.1)\times10^{-2}$	$(139.\pm4.1)\times10^{-2}$
0.44 –	0.62	$(108.\pm8.8)\times10^{-4}$	$(14.4\pm1.0)\times10^{-3}$	$(36.6\pm3.5)\times10^{-3}$	$(\ 4.7\pm1.1)\times10^{-1}$	$(132.\pm4.8)\times10^{-2}$
0.62 –	0.85	$(47.8\pm6.7)\times10^{-4}$	$(77.2\pm6.9)\times10^{-4}$	$(22.0\pm2.5)\times10^{-3}$	$(\ 7.5\pm1.3)\times10^{-1}$	$(114.\pm4.2)\times10^{-2}$
0.85 –	1.15	$(23.1\pm4.9)\times10^{-4}$	$(60.9\pm6.5)\times10^{-4}$	$(34.9\pm5.8)\times10^{-3}$	$(85.3\pm7.5)\times10^{-2}$	$(92.8\pm3.2)\times10^{-2}$
1.15 –	1.54	$(13.1\pm2.2)\times10^{-4}$	$(23.7\pm2.9)\times10^{-4}$	$(15.4\pm2.4)\times10^{-2}$	$(71.7\pm4.5)\times10^{-2}$	$(72.4\pm2.4)\times10^{-2}$
1.54 –	2.02	$(\ 7.7\pm1.2)\times10^{-4}$	$(44.8\pm6.7)\times10^{-4}$	$(28.1\pm3.3)\times10^{-2}$	$(52.4\pm4.5)\times10^{-2}$	$(51.1\pm1.4)\times10^{-2}$
2.02 –	2.62	$(77.7\pm8.3)\times10^{-5}$	$(43.1\pm5.8)\times10^{-3}$	$(30.9\pm1.8)\times10^{-2}$	$(36.2\pm2.9)\times10^{-2}$	$(37.0\pm1.1)\times10^{-2}$
2.62 –	3.38	$(49.1\pm5.9)\times10^{-4}$	$(11.4\pm1.1)\times10^{-2}$	$(22.6\pm1.4)\times10^{-2}$	$(24.8\pm2.1)\times10^{-2}$	$(241.\pm6.4)\times10^{-3}$
3.38 –	4.31	$(27.9\pm2.9)\times10^{-3}$	$(124.\pm4.6)\times10^{-3}$	$(15.4\pm1.1)\times10^{-2}$	$(16.2\pm1.1)\times10^{-2}$	$(163.\pm3.1)\times10^{-3}$
4.31 –	5.45	$(56.4\pm4.0)\times10^{-3}$	$(88.4\pm4.3)\times10^{-3}$	$(95.3\pm5.9)\times10^{-3}$	$(103.\pm7.7)\times10^{-3}$	$(102.\pm2.9)\times10^{-3}$
5.45 –	6.86	$(52.6\pm1.7)\times10^{-3}$	$(55.6\pm3.2)\times10^{-3}$	$(59.3\pm3.5)\times10^{-3}$	$(63.8\pm5.0)\times10^{-3}$	$(61.4\pm1.3)\times10^{-3}$
6.86 –	8.60	$(35.6\pm1.2)\times10^{-3}$	$(34.0\pm1.8)\times10^{-3}$	$(36.3\pm2.6)\times10^{-3}$	$(39.0\pm2.8)\times10^{-3}$	$(390.\pm8.2)\times10^{-4}$
8.60 –	10.73	$(212.\pm9.0)\times10^{-4}$	$(20.2\pm1.1)\times10^{-3}$	$(21.8\pm1.6)\times10^{-3}$	$(22.5\pm1.6)\times10^{-3}$	$(223.\pm6.5)\times10^{-4}$
10.73 –	13.34	$(129.\pm5.3)\times10^{-4}$	$(121.\pm6.4)\times10^{-4}$	$(128.\pm8.0)\times10^{-4}$	$(14.1\pm1.3)\times10^{-3}$	$(136.\pm4.5)\times10^{-4}$
13.34 –	16.55	$(75.8\pm3.3)\times10^{-4}$	$(69.0\pm3.8)\times10^{-4}$	$(75.2\pm4.3)\times10^{-4}$	$(78.0\pm5.7)\times10^{-4}$	$(76.2\pm2.7)\times10^{-4}$
16.55 –	20.48	$(41.7\pm1.5)\times10^{-4}$	$(40.5\pm2.1)\times10^{-4}$	$(40.2\pm3.0)\times10^{-4}$	$(39.3\pm3.3)\times10^{-4}$	$(39.6\pm1.3)\times10^{-4}$
20.48 –	25.29	$(24.9\pm1.1)\times10^{-4}$	$(22.7\pm1.3)\times10^{-4}$	$(237.\pm8.0)\times10^{-5}$	$(23.8\pm2.0)\times10^{-4}$	$(22.0\pm1.3)\times10^{-4}$
25.29 –	31.20	$(134.\pm5.6)\times10^{-5}$	$(132.\pm8.7)\times10^{-5}$	$(127.\pm6.4)\times10^{-5}$	$(12.3\pm1.4)\times10^{-4}$	$(118.\pm7.9)\times10^{-5}$
31.20 –	38.43	$(75.1\pm4.0)\times10^{-5}$	$(69.2\pm4.5)\times10^{-5}$	$(61.5\pm5.7)\times10^{-5}$	$(78.0\pm8.8)\times10^{-5}$	$(76.7\pm6.5)\times10^{-5}$
38.43 –	47.30	$(46.0\pm2.7)\times10^{-5}$	$(44.7\pm2.8)\times10^{-5}$	$(44.0\pm3.5)\times10^{-5}$	$(44.1\pm4.6)\times10^{-5}$	$(47.7\pm3.7)\times10^{-5}$
47.30 –	58.16	$(27.0\pm1.8)\times10^{-5}$	$(26.3\pm1.9)\times10^{-5}$	$(25.7\pm2.8)\times10^{-5}$	$(27.0\pm2.6)\times10^{-5}$	$(28.5\pm2.6)\times10^{-5}$
58.16 –	71.48	$(14.6\pm1.2)\times10^{-5}$	$(142.\pm9.9)\times10^{-6}$	$(13.9\pm1.3)\times10^{-5}$	$(14.3\pm1.5)\times10^{-5}$	$(154.\pm9.8)\times10^{-6}$
71.48 –	87.79	$(76.0\pm4.6)\times10^{-6}$	$(72.9\pm4.5)\times10^{-6}$	$(71.7\pm6.4)\times10^{-6}$	$(72.5\pm6.5)\times10^{-6}$	$(79.3\pm8.7)\times10^{-6}$
87.79 –	107.78	$(43.5\pm5.8)\times10^{-6}$	$(41.5\pm3.0)\times10^{-6}$	$(41.1\pm4.1)\times10^{-6}$	$(40.3\pm6.3)\times10^{-6}$	$(44.8\pm7.9)\times10^{-6}$
107.78 –	132.27	$(25.2\pm4.5)\times10^{-6}$	$(23.9\pm4.4)\times10^{-6}$	$(23.9\pm4.4)\times10^{-6}$	$(\ 2.3\pm1.2)\times10^{-5}$	$(\ 2.6\pm1.2)\times10^{-5}$
132.27 –	162.29	$(14.3\pm3.9)\times10^{-6}$	$(13.4\pm4.7)\times10^{-6}$	$(13.6\pm6.5)\times10^{-6}$	$(12.3\pm8.9)\times10^{-6}$	$(\ 1.4\pm1.4)\times10^{-5}$
162.29 –	199.06	$(\ 8.6\pm1.5)\times10^{-6}$	$(80.6\pm4.3)\times10^{-7}$	$(\ 8.2\pm1.3)\times10^{-6}$	$(\ 7.2\pm3.7)\times10^{-6}$	$(\ 8.5\pm2.4)\times10^{-6}$

Table 3: Differential downward proton flux spectra for higher latitudes.

Upward Proton Flux $(m^2\,sec\,sr\,MeV)^{-1}$					
E_{kin}	Geomagnetic Latitude Range				
(GeV)	$\Theta_M < 0.2$	$0.2 \le \Theta_M < 0.3$	$0.3 \le \Theta_M < 0.4$	$0.4 \le \Theta_M < 0.5$	$0.5 \le \Theta_M < 0.6$
0.07 – 0.10	$(16.4\pm4.4)\times10^{-2}$	$(13.1\pm3.9)\times10^{-2}$	$(12.6\pm3.5)\times10^{-2}$	$(14.7\pm4.1)\times10^{-2}$	$(15.8\pm4.7)\times10^{-2}$
0.10 – 0.15	$(10.9\pm1.4)\times10^{-2}$	$(\ 7.5\pm1.0)\times10^{-2}$	$(66.0\pm9.2)\times10^{-3}$	$(\ 7.7\pm1.1)\times10^{-2}$	$(\ 8.7\pm1.2)\times10^{-2}$
0.15 – 0.22	$(85.3\pm4.9)\times10^{-3}$	$(48.1\pm3.5)\times10^{-3}$	$(42.7\pm2.8)\times10^{-3}$	$(42.2\pm2.8)\times10^{-3}$	$(46.3\pm2.8)\times10^{-3}$
0.22 – 0.31	$(84.8\pm3.8)\times10^{-3}$	$(44.5\pm2.1)\times10^{-3}$	$(39.3\pm1.9)\times10^{-3}$	$(35.5\pm1.8)\times10^{-3}$	$(34.6\pm1.5)\times10^{-3}$
0.31 – 0.44	$(66.8\pm3.4)\times10^{-3}$	$(33.6\pm1.7)\times10^{-3}$	$(25.4\pm1.1)\times10^{-3}$	$(21.4\pm1.1)\times10^{-3}$	$(21.0\pm1.1)\times10^{-3}$
0.44 – 0.62	$(48.4\pm2.7)\times10^{-3}$	$(20.3\pm1.2)\times10^{-3}$	$(136.\pm8.3)\times10^{-4}$	$(124.\pm9.2)\times10^{-4}$	$(97.6\pm8.1)\times10^{-4}$
0.62 – 0.85	$(32.7\pm2.0)\times10^{-3}$	$(120.\pm8.6)\times10^{-4}$	$(76.4\pm5.6)\times10^{-4}$	$(61.9\pm6.1)\times10^{-4}$	$(34.8\pm4.3)\times10^{-4}$
0.85 – 1.15	$(20.2\pm1.1)\times10^{-3}$	$(53.9\pm4.6)\times10^{-4}$	$(42.0\pm4.5)\times10^{-4}$	$(31.9\pm4.6)\times10^{-4}$	$(17.9\pm3.3)\times10^{-4}$
1.15 – 1.54	$(124.\pm7.1)\times10^{-4}$	$(34.8\pm4.4)\times10^{-4}$	$(14.7\pm1.8)\times10^{-4}$	$(14.0\pm2.3)\times10^{-4}$	$(\ 8.6\pm2.1)\times10^{-4}$
1.54 – 2.02	$(62.0\pm4.2)\times10^{-4}$	$(16.4\pm2.3)\times10^{-4}$	$(12.5\pm2.3)\times10^{-4}$	$(\ 8.8\pm1.8)\times10^{-4}$	$(\ 5.2\pm1.2)\times10^{-4}$
2.02 – 2.62	$(25.9\pm1.8)\times10^{-4}$	$(\ 7.9\pm1.3)\times10^{-4}$	$(\ 5.6\pm1.1)\times10^{-4}$	$(\ 4.6\pm1.2)\times10^{-4}$	$(\ 3.4\pm1.1)\times10^{-4}$
2.62 – 3.38	$(10.7\pm1.5)\times10^{-4}$	$(\ 4.2\pm1.2)\times10^{-4}$	$(29.9\pm8.7)\times10^{-5}$	$(38.3\pm10.)\times10^{-5}$	$(25.9\pm9.6)\times10^{-5}$
3.38 – 4.31	$(29.7\pm5.7)\times10^{-5}$	$(15.6\pm8.3)\times10^{-5}$	$(11.9\pm4.9)\times10^{-5}$	$(13.4\pm5.7)\times10^{-5}$	$(\ 9.4\pm3.7)\times10^{-5}$
4.31 – 5.45	$(11.2\pm4.6)\times10^{-5}$	$(\ 6.4\pm4.2)\times10^{-5}$	$(\ 7.2\pm3.8)\times10^{-5}$	$(\ 6.4\pm3.3)\times10^{-5}$	
5.45 – 6.86	$(\ 3.7\pm2.4)\times10^{-5}$				

E_{kin}	Geomagnetic Latitude Range				
(GeV)	$0.6 \le \Theta_M < 0.7$	$0.7 \le \Theta_M < 0.8$	$0.8 \le \Theta_M < 0.9$	$0.9 \le \Theta_M < 1.0$	
0.07 – 0.10	$(23.1\pm6.8)\times10^{-2}$	$(32.9\pm9.5)\times10^{-2}$	$(\ 3.8\pm1.1)\times10^{-1}$	$(\ 5.1\pm1.5)\times10^{-1}$	
0.10 – 0.15	$(10.5\pm1.5)\times10^{-2}$	$(15.4\pm2.3)\times10^{-2}$	$(18.0\pm2.4)\times10^{-2}$	$(25.5\pm4.1)\times10^{-2}$	
0.15 – 0.22	$(58.1\pm3.8)\times10^{-3}$	$(72.5\pm5.4)\times10^{-3}$	$(91.9\pm6.2)\times10^{-3}$	$(99.8\pm8.4)\times10^{-3}$	
0.22 – 0.31	$(43.0\pm2.1)\times10^{-3}$	$(44.8\pm3.4)\times10^{-3}$	$(57.4\pm3.3)\times10^{-3}$	$(54.0\pm4.9)\times10^{-3}$	
0.31 – 0.44	$(20.7\pm1.1)\times10^{-3}$	$(21.7\pm1.9)\times10^{-3}$	$(25.7\pm2.6)\times10^{-3}$	$(22.5\pm2.9)\times10^{-3}$	
0.44 – 0.62	$(83.4\pm8.0)\times10^{-4}$	$(78.6\pm9.3)\times10^{-4}$	$(\ 8.8\pm1.2)\times10^{-3}$	$(\ 8.8\pm1.7)\times10^{-3}$	
0.62 – 0.85	$(27.3\pm4.0)\times10^{-4}$	$(18.4\pm3.2)\times10^{-4}$	$(17.9\pm4.8)\times10^{-4}$	$(23.4\pm8.0)\times10^{-4}$	
0.85 – 1.15	$(\ 7.2\pm2.3)\times10^{-4}$	$(\ 4.9\pm1.9)\times10^{-4}$	$(\ 7.4\pm4.2)\times10^{-4}$	$(12.6\pm5.1)\times10^{-4}$	
1.15 – 1.54	$(\ 4.0\pm1.3)\times10^{-4}$	$(\ 3.2\pm2.3)\times10^{-4}$	$(\ 2.5\pm1.5)\times10^{-4}$	$(\ 9.1\pm4.0)\times10^{-4}$	
1.54 – 2.02	$(\ 3.0\pm1.4)\times10^{-4}$	$(11.6\pm7.2)\times10^{-5}$	$(\ 1.3\pm1.2)\times10^{-4}$	$(16.8\pm9.3)\times10^{-5}$	
2.02 – 2.62	$(\ 1.7\pm1.2)\times10^{-4}$	$(\ 7.7\pm7.4)\times10^{-5}$			
2.62 – 3.38	$(\ 6.3\pm4.1)\times10^{-5}$	$(\ 4.8\pm3.8)\times10^{-5}$			
3.38 – 4.31	$(\ 2.0\pm1.1)\times10^{-5}$				

Table 4: Differential upward proton flux spectra.

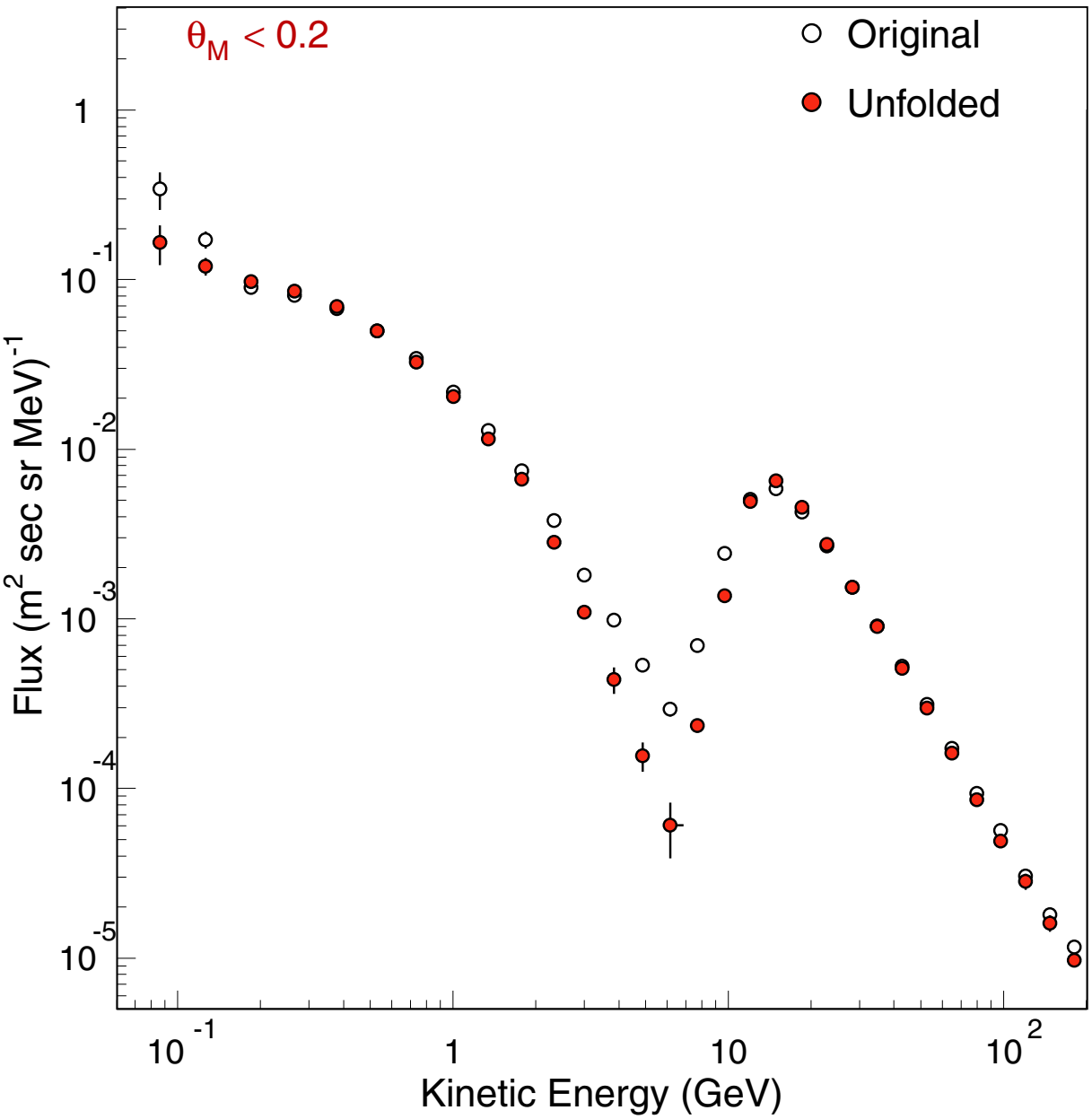

Figure 1: The proton differential flux in the equatorial region. Open circles show the measured distribution, filled circles are the data after unfolding.

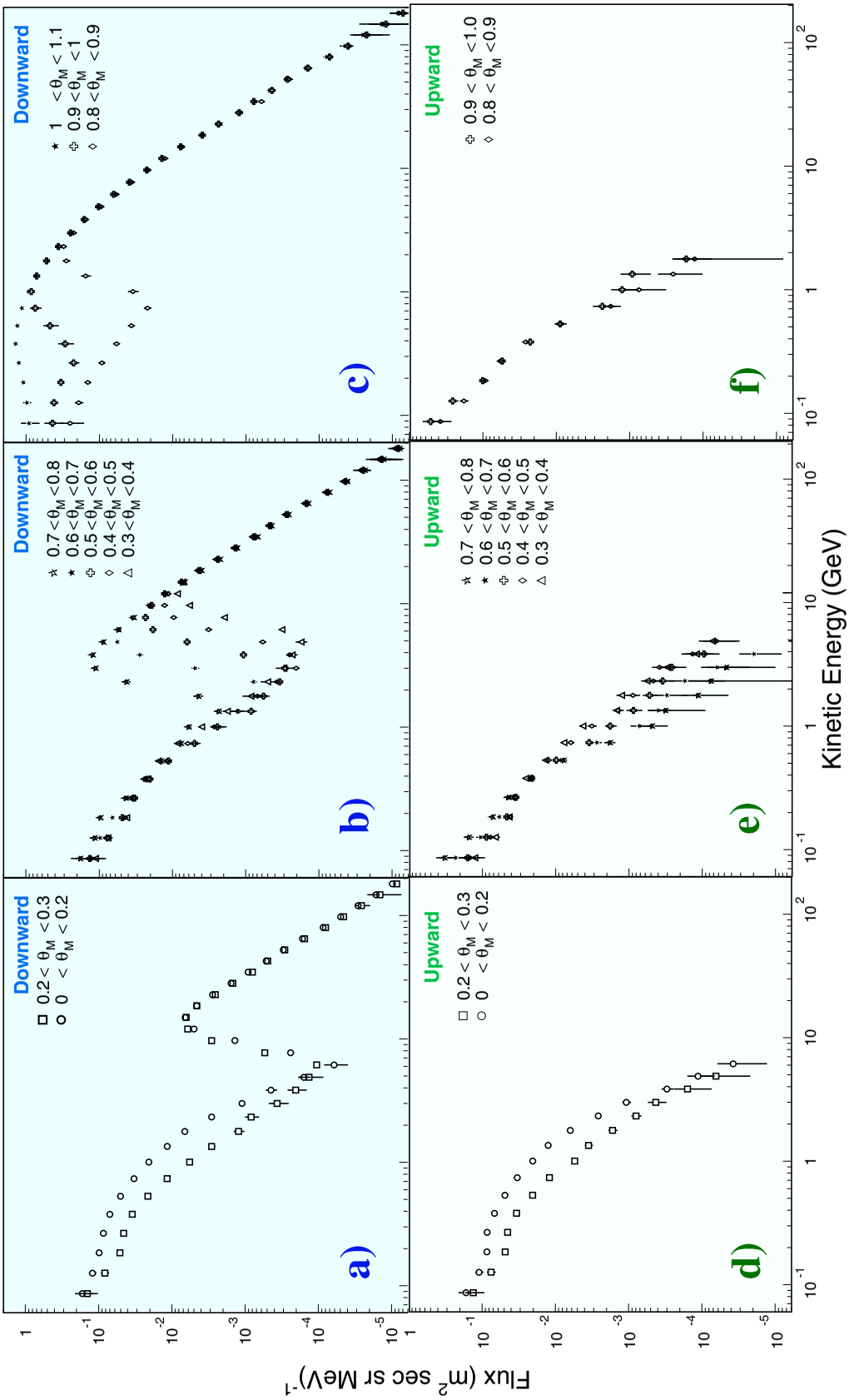

Figure 2: Flux spectra for a,b,c) downward and d,e,f) upward going protons seperated according to the geomagnetic latitude, Θ_M, at which they were detected.

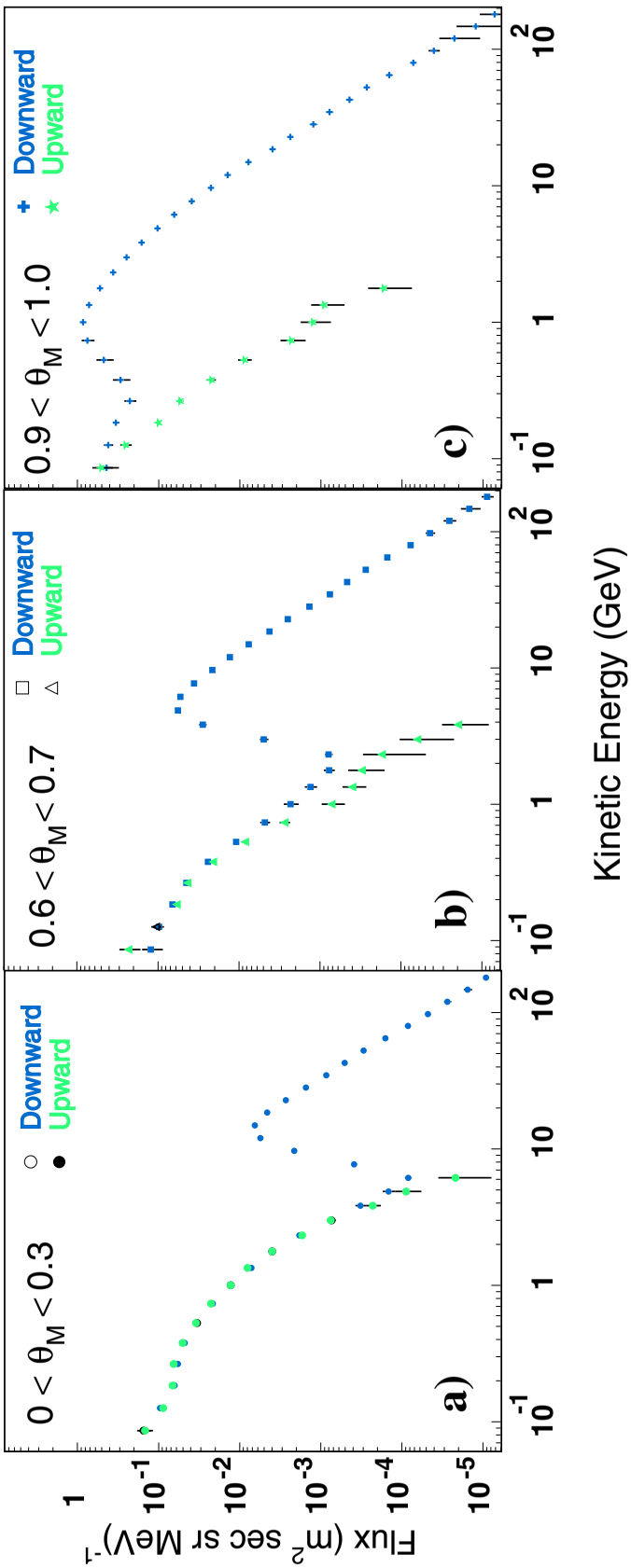

Figure 3: Comparison of upward and downward second spectrum proton at different geomagnetic latitudes. As seen, below cutoff, the upward and downward fluxes agree in the range $0 \leq \Theta_M < 0.8$ (see also Figs. 2b, e).

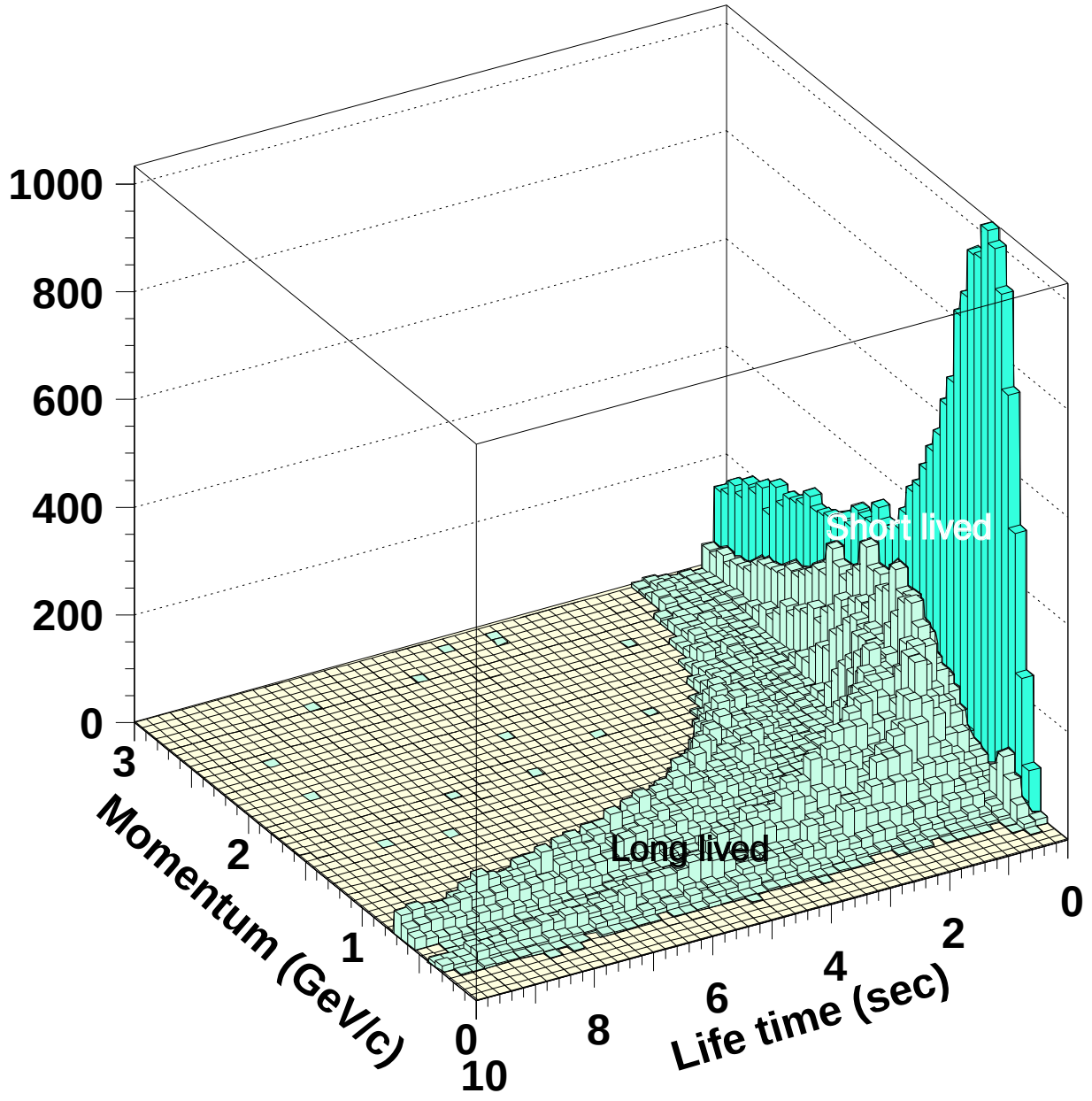

Figure 4: The interval between production and detection, or flight time, versus momentum from the back tracing of protons detected in the region $\Theta_M < 0.3$.

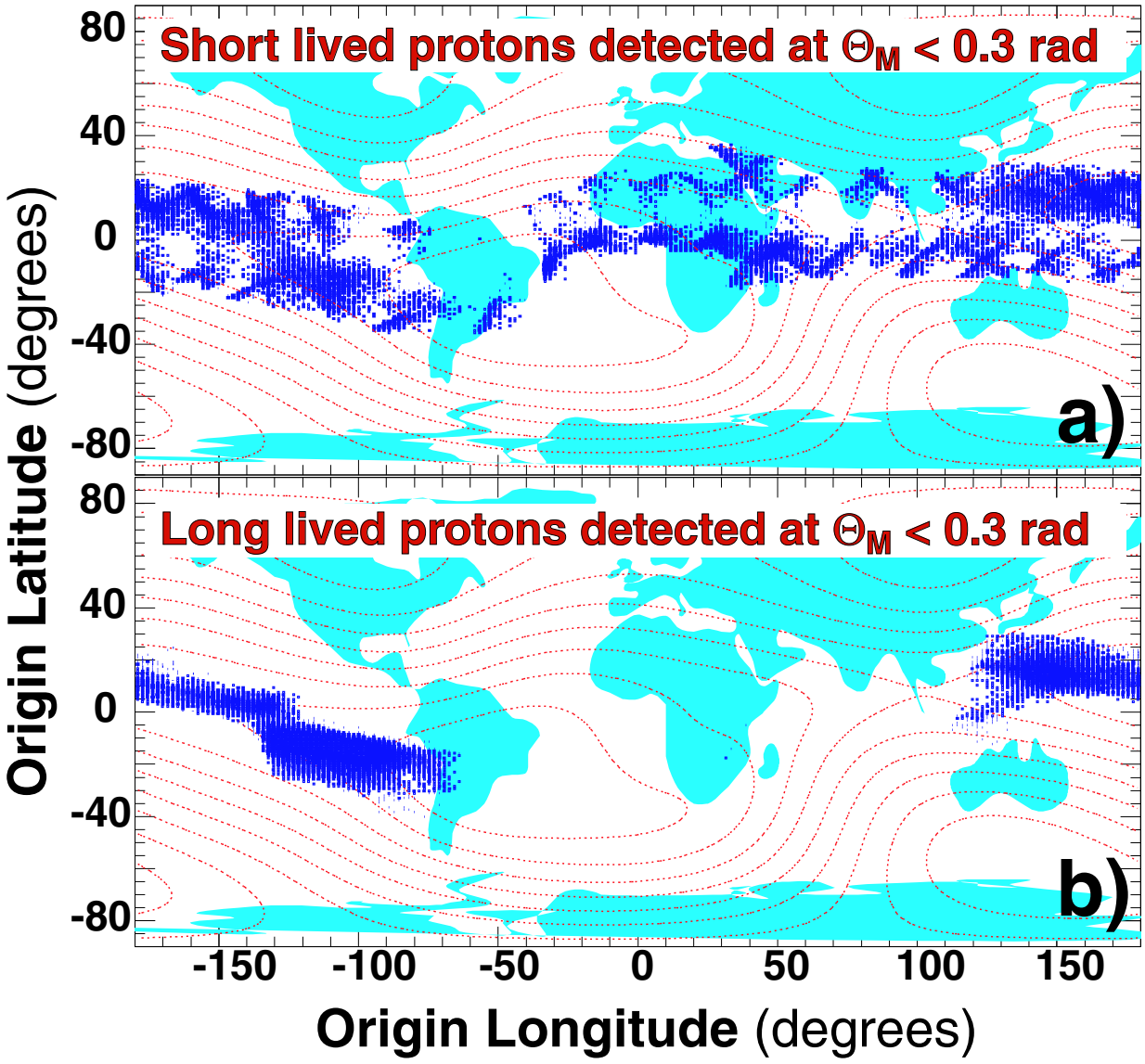

Figure 5: The geographical origin of a) short–lived and b) long–lived protons with $p < 3$ GeV/c. The dashed lines indicate the geomagnetic field countours at 380 km.

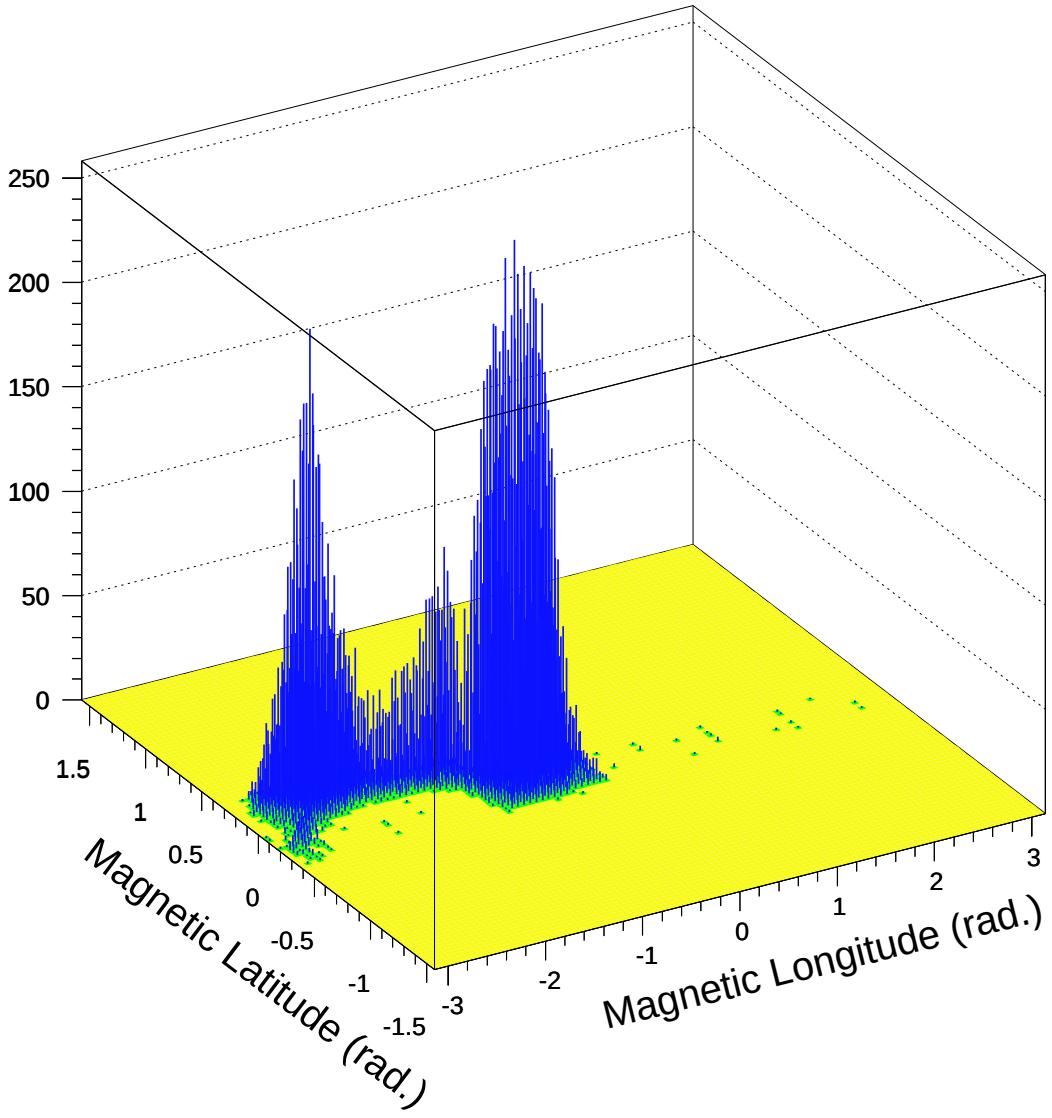

Figure 6: The point of origin of long–lived protons ($\Theta_M < 0.3, p < 3\,\mathrm{GeV/c}$) in geomagnetic coordinates.

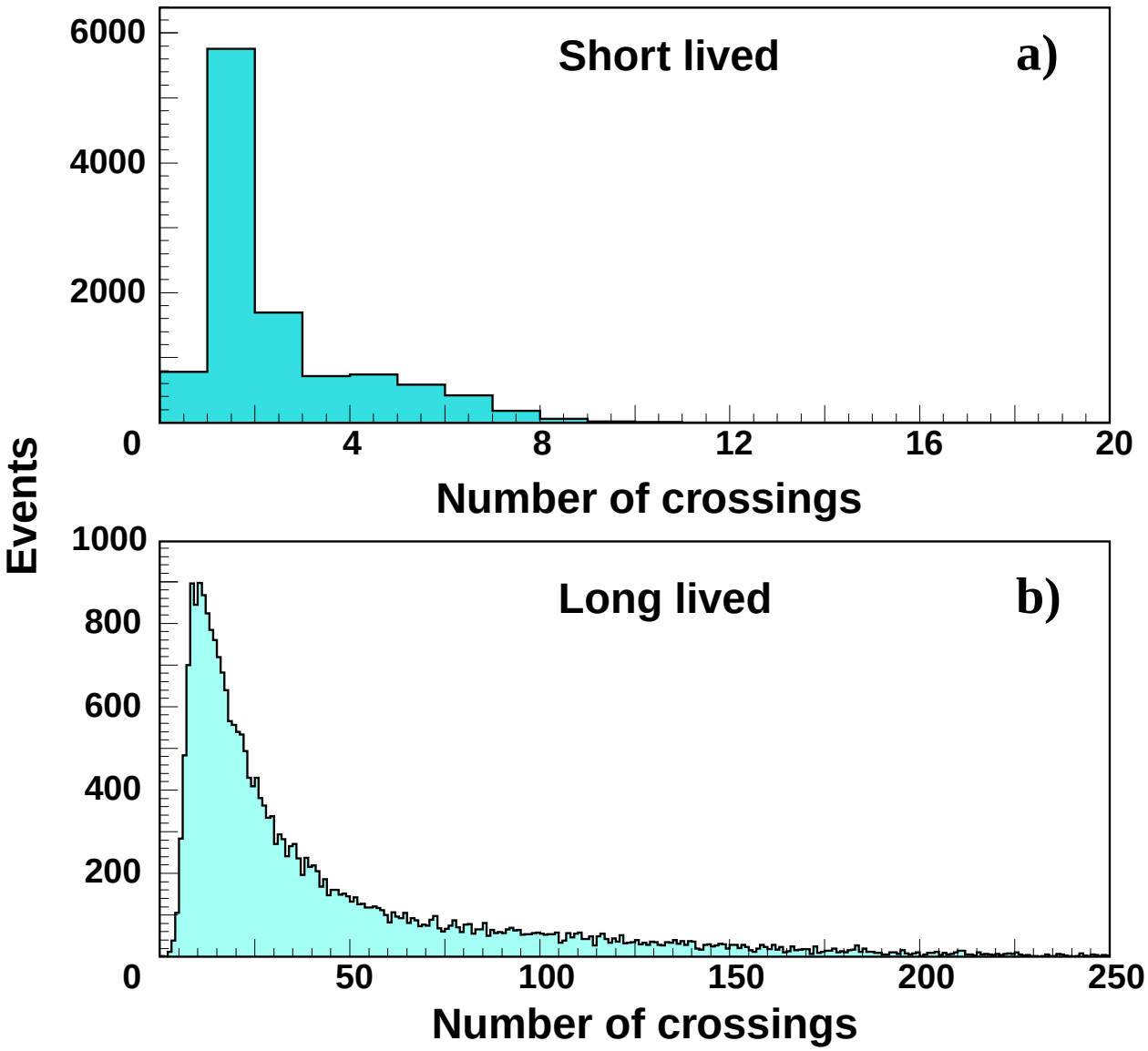

Figure 7: Number of times the back traced trajectory crosses the geomagnetic equator for a) short–lived and b) long–lived protons ($\Theta_M < 0.3, p < 3$ GeV/c).

AMS paper 02 : "Protons in Near Earth Orbit" -
Physics Letters B 472 (2000) 215-226
Referee's report :

"This is a paper with completely new data on the proton flux in the earth magnetosphere between the upper atmosphere and an altitude of 380km. It is of unprecedented quality. The data is certainly of great importance as e.g. input for precise calculations of the atmospheric neutrino flux. It should very soon be published in Phys.Lett.B.

One point however needs clarification, it should be made clear that excluding "data from the South Atlantic Anomaly" has no influence on the distribution of the point of origin of the secondary component and in particular for the "long-lived" protons. Finally as a minor point, Ref[9] appears to me misplaced in the text, and in addition in the citation the report# should read DESY 84-118 (not 85-118)".

Attachment III

Leptons in Near Earth Orbit

The AMS Collaboration

Abstract

The lepton spectra in the kinetic energy ranges 0.2 to 40 GeV for e^- and 0.2 to 3 GeV for e^+ were measured by the Alpha Magnetic Spectrometer (AMS) during space shuttle flight STS–91 at altitudes near 380 km. From the origin of the leptons two distinct spectra were observed: a higher energy spectrum and a substantial second spectrum with positrons much more abundant than electrons. Tracing leptons from the second spectra shows that most of these leptons travel for an extended period of time in the geomagnetic field and that the e^+ and e^- originate from two complementary geographic regions.

Published in Phys. Lett. B484 (27 Jun 2000) 10-22

Referee's report attached.

Introduction

The current understanding of the high energy lepton ($e^{\pm}$) spectra in cosmic rays is that they are dominated by an electron component. High energy electrons are believed to originate from primary acceleration sites, specifically from supernova explosions. High energy electron–positron pairs are thought to be produced from the collisions of cosmic ray hadrons and gamma rays with interstellar gas. Taken together, the expected positron to electron ratio in cosmic rays arriving at Earth is roughly 10% and it decreases with energy. This picture is based on the experimental data collected over 35 years [1, 2] by balloon experiments as well as phenomenological model descriptions developed over the same period [3]. These experiments were performed at altitudes of 30–40 km. Balloon experiments have made important contributions to the understanding of primary cosmic ray spectra and the behavior of atmospheric secondary particles in the upper layer of the atmosphere.

A few pioneering satellite experiments [4] have reported data on low energy electrons and positrons trapped in the geomagnetic field. The satellite based detectors used so far, *i.e.* before this experiment, have not been sensitive enough to systematically study the electron and positron spectra over a broad energy range and their dependence on position and angle.

The electron spectrum observed near Earth shows a low energy drop off due to the geomagnetic cutoff. Previous measurements above the cutoff indicate that the spectrum falls off according to a power law.

The Alpha Magnetic Spectrometer (AMS) [5] is a high energy physics experiment scheduled for installation on the International Space Station. In preparation for this mission, AMS flew a precursor mission on board the space shuttle Discovery during flight STS–91 in June 1998. In this report we use the data collected to study the spectra of electrons and positrons in cosmic rays over the respective kinetic energy ranges of 0.2 to 40 GeV and 0.2 to 3 GeV, the latter range being limited by the proton background.

The large acceptance of AMS and high statistics ($\sim 10^5$) enable us to study the variation of the spectra with position and angle both above and below the geomagnetic cutoff. The accurate momentum resolution, precise trajectory reconstruction and good particle identification of AMS allow an investigation into the origin of particles below cutoff by tracking them in the geomagnetic field.

The AMS detector

The major elements of AMS as flown on STS–91 were a permanent magnet, a tracker, time of flight hodoscopes, a Cerenkov counter and anti-coincidence counters [6, 7]. The permanent magnet had the shape of a cylindrical shell with inner diameter 1.1 m, length 0.8 m. It provided a central dipole field of 0.14 Tesla across the magnet bore and an analyzing power, BL^2, of 0.14 Tm^2 parallel to the magnet, or z–, axis. The six layers of double sided silicon tracker were arrayed transverse to the magnet axis. The outer layers were just outside the magnet bore. The tracker measured the trajectory of relativistic singly charged particles with an accuracy of 20 microns in the bending coordinate and 33 microns in the non-bending coordinate, as well as providing multiple measurements of the energy loss. The time of flight system had two planes at each end of the magnet, covering the outer tracker layers. Together the four planes measured singly charged particle transit times with an accuracy of 120 psec and also yielded multiple energy loss measurements. Two layers of Aerogel threshold Cerenkov counter with an index of refraction $n = 1.035$ were used to make independent velocity measurements allowing the discrimination of lower energy hadrons from electrons and positrons. A layer of anti-coincidence scintillation counters lined the inner surface of the magnet. Low energy particles were absorbed by thin carbon fiber shields. In flight the AMS positive z–axis pointed out of the shuttle payload bay.

For this study the acceptance was restricted to events with an incident angle within 25° of the positive z–axis of AMS and data from four periods are included. In the first period the z–axis was pointing within 1° of the zenith. Events from this period are referred to as "downward" going. In the second period the z–axis pointing was within 1° of the nadir. Data from this period are referred to as "upward" going. In the third and fourth periods the AMS z–axis was pointing within 20° and 45° of the zenith. The orbital inclination was 51.7° and the geodetic altitude during these periods ranged from 350 to 390 km. Data taken while passing through or near the South Atlantic Anomaly were excluded from this analysis.

The response of the detector was simulated using the AMS detector simulation program, which is based on the GEANT package [8]. The effects of energy loss, multiple scattering, interactions, decays and the measured detector efficiency and resolution were included.

After the flight the AMS detector was extensively calibrated at two accelerators: at GSI, Darmstadt, with helium and carbon beams at 600 incident angles and locations and 10^7 events, and at the CERN proton-synchrotron in the energy region of 2 to 14 GeV, with 1200 incident angles and locations and 10^8 events. This ensured that the performance of the detector and the analysis procedure were thoroughly understood.

Analysis

Event reconstruction, analysis and spectrum unfolding are detailed in [9]. Electron candidates were specifically selected by requiring the measured particle charge to be −1 and the particle velocity to be compatible with the speed of light. Backgrounds arose from protons with wrongly measured momentum and secondary pions produced in the detector materials. The two most important cuts used to remove these backgrounds were on the χ^2 value obtained in fitting the particle trajectory, which removed tracks with large single or multiple scattering, and on the number of hits near the reconstructed trajectory in both the tracker and time of flight scintillators.

After the above cuts were applied, the overall probability of a proton event to be accepted as an electron, estimated from Monte Carlo simulations and confirmed in the CERN test beam, was $O(10^{-4})$ with an electron selection efficiency of 75%. To further reduce the pion background only events whose track passed through the active Cerenkov counter area and, therefore, had an independent velocity measurement were accepted.

Positron candidates were selected by requiring the charge to be +1 and, as for electrons, the velocity be compatible with the speed of light and track quality cuts. In contrast to electrons, the main background for the positron sample came from proton events with poorly measured velocity. The rejection power against this background decreased rapidly with increasing proton momentum, therefore tighter quality cuts on the velocity measurements were applied. Above 1 GeV/c protons were rejected by requiring two independent velocity measurements from the two separate Cerenkov counter layers to be compatible with the velocity of a positron. Lower energy protons were rejected by requiring the energy loss measurements in four layers of time of flight counters and six double layers of silicon tracker to be compatible with a positron. These cuts yielded an additional background rejection factor of 5 at the expense of lower positron selection efficiency. Table 1 summarizes the estimated efficiencies.

A convolution of the background rejection function with the measured proton spectra provided an energy dependent background estimation. Fig. 1 shows the measured electron and positron spectra together with the estimated background for the geomagnetic polar regions, where the background conditions were most severe.

Cut	Efficiency (%)
Tracking Quality Cuts	75 ± 3
Common $e^{\pm}$ Velocity Cuts	52 ± 1
Additional e^{+} Velocity Cuts	72 ± 1.5
Total electrons	39 ± 1.7
Total positrons	28 ± 1.3

Table 1: Percentage $e^{\pm}$ selection efficiencies and uncertainties.

The acceptance was determined as a function of particle momentum and direction. The average acceptance was found to rise from about $0.01\,m^2$ sr at 0.15 GeV and level off at $0.1\,m^2$ sr above 0.7 GeV with a systematic uncertainty of 5 % [9]. The incident differential spectrum was obtained from the measured spectrum by using an unfolding method based on Bayes' theorem [10] with resolution functions obtained from the simulation. These functions were confirmed at several energy points with calibration measurements in the CERN proton beams.

Results and interpretation

Fig. 2 presents the downward lepton spectra integrated over incident angles within 25° of the AMS z–axis, which was within 1° of the zenith. In Fig. 3 these spectra are compared with the spectra measured with upward going leptons. The measurements have been binned according to the absolute value of the corrected geomagnetic latitude [11], Θ_M (radians), at which they were detected. The effect of the geomagnetic cutoff and the decrease in this cutoff with increasing Θ_M is particularly visible in the downward electron spectra. The spectra above and below cutoff differ. To understand this difference the trajectory of electrons and positrons were traced [12] back from their measured incident angle, location and momentum, through the geomagnetic field [13]. This was continued until the trajectory was traced to outside the Earth's magnetosphere or until it crossed the top of the atmosphere at an altitude of 40 km. In a refinement from [9], the spectra from particles which were traced to originate far away from Earth are classified as "primary" and those from particles which originate in the atmosphere as "second" spectra. In practice particles below the cutoff are from the second spectra, however this classification provides a cleaner separation in the transition region.

I. Properties of the primary lepton spectra

Fig. 4a shows the primary lepton spectra. The spectra are in reasonable agreement with previous measurements [2]. Fig. 4b shows the the energy dependence of the positron fraction, which exhibits the predominance of electrons over positrons in primary cosmic rays.

II. Properties of the second lepton spectra

As shown in Figs. 2 and 3, substantial second lepton spectra are observed for downward and upward going leptons at all geomagnetic latitudes below the geomagnetic cutoff. These spectra have the following properties:

(i) The second lepton spectra of Fig. 2 exhibit similar qualitative behavior to the proton spectra [9].

(ii) At polar latitudes the downward second spectrum of electrons is gradually obscured by the primary spectrum, whereas the second spectrum of upward going electrons is clearly observed (see Figs. 2 and 3).

(iii) For both electrons and positrons the upward and downward fluxes are nearly identical (see Fig. 3).

(iv) As seen from Fig. 5 the lepton fluxes reach a maximum at the geomagnetic equator. With increasing latitude the positron flux drops off faster than the electron flux.

In addition to the backward tracing mentioned above the leptons were also traced forward until their trajectory would have either escaped or crossed the top of the atmosphere, the location of which was taken as the particle sink. The results show that all second spectrum particles eventually re-enter the atmosphere. Defining the flight time as the sum of forward and backward tracing times, that is the interval between origin and sink, Fig. 6 shows the distribution of flight time versus energy for electrons and positrons. Both e^+ and e^- exhibit two distinct types of trajectories:

- The horizontal bands with flight times < 0.2 sec, defined as "short–lived".
- The diagonal bands with flight times ≥ 0.2 sec defined as "long–lived".

For $\Theta_M < 0.3$, most (75% of e^+, 65% of e^-) leptons are long–lived.

Distinct properties of the second spectra for short–lived leptons

The trajectory tracing shows that leptons travel in cycles across the equator where the trajectories reach maximal altitude and they are reflected at the lowest points at the mid and polar latitudes. For short–lived leptons:

- From Fig. 6 one sees that the flight time is independent of lepton energy.
- The point of origin shows no longitude dependence. They do not originate from near to the geomagnetic equator, $\Theta_M < 0.4$ (see Fig. 7a,b).
- The particle flux is independent of the shuttle attitude and is approximately isotropic (see Fig. 7c,d,e).

Distinct properties of the second spectra for long–lived leptons

- As shown in Fig. 8 long–lived e^- and e^+ originate from well defined, complementary geographic regions. Tracing also shows that the regions of origin for positrons coincide with regions of sink for electrons and vice versa.
- Fig. 9 shows the strongly peaked distributions of the point of origin of the long–lived leptons in geomagnetic coordinates. Within the regions indicated the distributions are strongly peaked and the two diagonal bands (*A, B*) seen in Fig. 6 for the long–lived leptons correspond to the two regions of origin (*A, B*) marked in Figs. 8 and 9.
- The long–lived leptons are reflected across the equator hundreds of times. The number of cycles they can make before being absorbed in the atmosphere decreases with their energy.

- As shown in Fig. 8c,d,e, the long–lived lepton flux reaches a maximum in the equatorial region where they are produced and absorbed.
- At zenith shuttle orientation, 99% of the long–lived leptons are actually detected at $\Theta_M < 0.4$, indicating a strongly anisotropic angular distribution.

We note that the behaviour of protons and positrons is very similar (see [9]).

Lepton charge ratio

An interesting feature of the observed second lepton spectra is the predominance of positrons over electrons. In table 2 the e^+/e^- ratios grouped according to magnetic latitude region and shuttle attitude (0°, 20°, 45°, 180°) are given separately for long–lived and short–lived leptons. As seen from table 2

e^+/e^-	Long–lived (flight time ≥ 0.2 seconds)				
Attitude	$0.0< \Theta_M <0.2$	$0.2< \Theta_M <0.4$	$0.4< \Theta_M <0.6$	$0.6< \Theta_M <0.8$	$0.8< \Theta_M <1.0$
0°	4.27 ± 0.17	3.26 ± 0.37	1.65 ± 1.24		
20°	4.15 ± 0.39	2.75 ± 0.45	2.92 ± 1.00	1.05 ± 0.69	1.46 ± 0.42
45°	4.36 ± 0.40	3.41 ± 0.30	3.81 ± 0.33	2.27 ± 0.18	1.28 ± 0.16
180°	4.27 ± 0.25	4.25 ± 0.65			
e^+/e^-	Short–lived (flight time < 0.2 seconds)				
Attitude	$0.0< \Theta_M <0.2$	$0.2< \Theta_M <0.4$	$0.4< \Theta_M <0.6$	$0.6< \Theta_M <0.8$	$0.8< \Theta_M <1.0$
0°	3.08 ± 0.35	2.43 ± 0.19	1.35 ± 0.11	1.10 ± 0.11	0.83 ± 0.10
20°	2.83 ± 0.67	2.23 ± 0.37	1.95 ± 0.28	1.48 ± 0.22	0.94 ± 0.18
45°	3.22 ± 0.44	2.18 ± 0.32	2.01 ± 0.32	1.08 ± 0.12	0.93 ± 0.19
180°	4.84 ± 0.81	2.79 ± 0.28	1.45 ± 0.18	1.17 ± 0.21	0.68 ± 0.27

Table 2: Lepton charge ratio versus magnetic latitude for the shuttle attitudes 0°, 20°, 45° and 180° for long–lived and short–lived particles.

the ratios:

- Depend at most weakly on the shuttle orientation.
- The ratios for short– and long–lived leptons behave differently. For short–lived leptons the e^+/e^- ratio is maximal at the magnetic equator where it reaches a value of ~ 3 whereas for long–lived leptons the ratio is higher, ≳4 at the magnetic equator, and less dependent on latitude.
- The energy dependence of the e^+/e^- ratio for 0° attitude and $\Theta_M < 0.3$ is shown in Fig. 10. As seen, short–lived and long–lived leptons behave differently. For short-lived leptons the ratio does not depend on the particle energy in the range 0.2 to 3 GeV but for long–lived leptons the ratio does depend on the lepton energy, reaching a maximum value of ~ 5.

The combined (short– and long–lived, all attitudes) dependence on Θ_M of the ratio for all second spectra particles is shown in Fig. 11.

Acknowledgements

The support of INFN, Italy, ETH–Zürich, the University of Geneva, the Chinese Academy of Sciences, Academia Sinica and National Central University, Taiwan, the RWTH–Aachen, Germany, the University of Turku, the University of Technology of Helsinki, Finland, the U.S. DOE and M.I.T., CIEMAT, Spain, LIP, Portugal and IN2P3, France, is gratefully acknowledged.

The success of the first AMS mission is due to many individuals and organizations outside of the collaboration. The support of NASA was vital in the inception, development and operation of the experiment. Support from the Max–Plank Institute for Extraterrestrial Physics, from the space agencies of Germany (DLR), Italy (ASI), France (CNES) and China and from CSIST, Taiwan also played important parts in the success of AMS.

References

[1] R.R. Daniel and S.A. Stephens, Phys. Rev. Lett. **15** (1965) 769; C.J. Bland *et al.*, Phys. Rev. Lett. **17** (1966) 813; S.D. Verma, J. Geophys. Res. **72** (1967) 915; C.J. Bland *et al.*, Nouvo Cim. **LV B** (1968) 451; B. Agrinier *et al.*, Nouvo Cim.Lett. **1** (1969) 54; J.L. Fanselow *et al.*, ApJ **158** (1969) 771; J. Daugherty *et al.*, ApJ **198** (1975) 493; A. Buffington *et al.*, ApJ **199** (1975) 669; R. Hartman and C. Pellerin, ApJ **204** (1976) 927; K.K. Tang, ApJ **278** (1984) 881; R.L. Golden *et al.*, ApJ **287** (1985) 662; D. Muller and K. Tang, ApJ **312** (1987) 183; G. Barbiellini *et al.*, Astronomy and Astrophysics **309** (1996) L15; R.L. Golden *et al.*, ApJ **457** (1996) L103; S.W. Barwick *et al.*, ApJ **482** (1997) L191; S.W. Barwick *et al.*, J. Geophys. Res. **103** (1998) 4817; S. Torii *et al.*, Proc. 26th ICRC **3** (1999) 53; M. Boezio *et al.*, Proc. 26th ICRC **3** (1999) 57; S. Coutu *et al.*, Astropart.Phys. **11** (1999) 429.

[2] R.L. Golden *et al.*, ApJ **436** (1994) 769; S.W. Barwick *et al.*, ApJ **498** (1998) 779; M.A. DuVernois *et al.*, Proc. 26th ICRC **3** (1999) 49.

[3] O.A. Bogdanova *et al.*, 15 ICRC Plovdiv **3** (1977) 176; M. Giler *et al.*, J.Phys.A:Math.Gen. **10** (1977) 843; R.J. Protheroe, ApJ **254** (1982) 391; W.R. Webber, 20 ICRC **2** (1987) 80; I.V. Moskalenko and A.W. Strong, ApJ **493** (1998) 694.

[4] J.B. Cladis *et al.*, J. Geophys. Res. **66** (1961) 2297; L.V. Kurnosova *et al.*, 15 ICRC Plovdiv **4** (1977) 185; R.N. Basilova *et al.*, 16 ICRC Kyoto **3** (1979) 150; N.L. Grigorov *et al.*, Dokl.Akad.Nauk SSSR **282** (1985) 81; Yu.E. Efimov *et al.*, Chechoslovak Journ. of Phys. **35** (1985) 1371; S.A. Voronov *et al.*, Izv.Vysshikh Uchebn.Zavedenii,Fizika **9** (1986) 19–24; S.A. Voronov *et al.*, Geomagnetism and Aeronomy **27** (1987) 424; A.F. Iydin *et al.*, Geomagnetism and Aeronomy **28** (1988) 103; S.V. Koldashov *et al.*, 24 ICRC Roma **4** (1995) 993; A.M. Galper *et al.*, 25 ICRC Durban **4** (1997) 333.

[5] S. Ahlen *et al.*, Nucl. Inst. Meth. **A350** (1994) 351.

[6] G.M. Viertel and M. Capell, Nucl. Inst. Meth. **A419** (1998) 295–299.

[7] AMS Collaboration, J. Alcaraz *et al.*, Phys. Lett. **B461** (1999) 387–396.

[8] R. Brun *et al.*, GEANT 3, CERN DD/EE/84-1 (Revised, 1987); P.A. Aamio *et al.*, FLUKA Users Guide, CERN TIS-RP-190 (1990).

[9] AMS Collaboration, J. Alcaraz *et al.*, Phys. Lett. **B472** (2000) 215–226.

[10] A. Kondor, Nucl. Inst. Meth. **216** (1983) 177; G. D'Agostini, Nucl. Inst. Meth. **A362** (1995) 487.

[11] A. Brekke, Physics of the Upper Polar Atmosphere, pp. 127–145, (Wiley, 1997).

[12] Y.L. Chuang *et al.*, Chinese Journal of Physics, in preparation (2000); N. Zographos, ETHZ-IPP 99-04 (1999).

[13] N.A. Tsyganenko and A.V. Usmanov, Planet. Space Sci. **30** (1982) 985–998; N.A. Tsyganenko *et al.*, Software for Computations of Geomagnetic Field and Related Coordinate Systems, Soviet Geophysical Committee, Special Report (1987); N.A. Tsyganenko, Planet. Space Sci. **35** (1987) 1347–1358; N.A. Tsyganenko, Planet. Space Sci. **37** (1989) 5–20; N.A. Tsyganenko, J. Geophys. Res. **100** (1995) 5599–5612; N.A. Tsyganenko and D.P. Stern, J. Geophys. Res. **101** (1996) 27187–27198; R.L. Langel, Chairman, IAGA Div. V working group 8, J. Geomag. Geoelectr. **47** (1995) 1251–1261; G. Gustafsson, N.E. Papitashvili and V.O. Papitashvili, J. Atmos. Terr. Phys. **54** (1992) 1609–1631.

The AMS Collaboration

J.Alcaraz[y] B.Alpat[ac] G.Ambrosi[r] H.Anderhub[ag] L.Ao[g] A.Arefiev[ab] P.Azzarello[r] E.Babucci[ac] L.Baldini[j,l] M.Basile[j] D.Barancourt[s] F.Barao[w,v] G.Barbier[s] G.Barreira[w] R.Battiston[ac] R.Becker[l] U.Becker[l] L.Bellagamba[j] P.Béné[r] J.Berdugo[y] P.Berges[l] B.Bertucci[ac] A.Biland[ag] S.Bizzaglia[ac] S.Blasko[ac] G.Boella[z] M.Boschini[z] M.Bourquin[r] L.Brocco[j] G.Bruni[j] M.Buenerd[s] J.D.Burger[l] W.J.Burger[ac] X.D.Cai[l] C.Camps[b] P.Cannarsa[ag] M.Capell[l] D.Casadei[j] J.Casaus[y] G.Castellini[p] C.Cecchi[ac] Y.H.Chang[m] H.F.Chen[t] H.S.Chen[i] Z.G.Chen[g] N.A.Chernoplekov[aa] T.H.Chiueh[m] Y.L.Chuang[ad] F.Cindolo[j] V.Commichau[b] A.Contin[j] P.Crespo[w] M.Cristinziani[r] J.P.da Cunha[n] T.S.Dai[l] J.D.Deus[v] N.Dinu[ac,1] L.Djambazov[ag] I.D'Antone[j] Z.R.Dong[h] P.Emonet[r] J.Engelberg[u] F.J.Eppling[l] T.Eronen[af] G.Esposito[ac] P.Extermann[r] J.Favier[c] E.Fiandrini[ac] P.H.Fisher[l] G.Fluegge[b] N.Fouque[c] Yu.Galaktionov[ab,l] M.Gervasi[z] P.Giusti[j] D.Grandi[z] O.Grimm[ag] W.Q.Gu[h] K.Hangarter[b] A.Hasan[ag] V.Hermel[c] H.Hofer[ag] M.A.Huang[ad] W.Hungerford[ag] M.Ionica[ac,1] R.Ionica[ac,1] M.Jongmanns[ag] K.Karlamaa[u] W.Karpinski[a] G.Kenney[ag] J.Kenny[ac] W.Kim[ae] A.Klimentov[l,ab] R.Kossakowski[c] V.Koutsenko[l,ab] M.Kraeber[ag] G.Laborie[s] T.Laitinen[af] G.Lamanna[ac] G.Laurenti[j] A.Lebedev[l] S.C.Lee[ad] G.Levi[j] P.Levtchenko[ac,2] C.L.Liu[x] H.T.Liu[i] I.Lopes[n] G.Lu[g] Y.S.Lu[i] K.Lübelsmeyer[a] D.Luckey[l] W.Lustermann[ag] C.Mañа[y] A.Margotti[j] F.Mayet[s] R.R.McNeil[e] B.Meillon[s] M.Menichelli[ac] A.Mihul[k] A.Mourao[v] A.Mujunen[u] F.Palmonari[j] A.Papi[ac] I.H.Park[ae] M.Pauluzzi[ac] F.Pauss[ag] E.Perrin[r] A.Pesci[j] A.Pevsner[d] M.Pimenta[w,v] V.Plyaskin[ab] V.Pojidaev[ab] V.Postolache[ac,1] N.Produit[r] P.G.Rancoita[z] D.Rapin[r] F.Raupach[a] D.Ren[ag] Z.Ren[ad] M.Ribordy[r] J.P.Richeux[r] E.Riihonen[af] J.Ritakari[u] U.Roeser[ag] C.Roissin[s] R.Sagdeev[o] G.Sartorelli[j] A.Schultz von Dratzig[a] G.Schwering[a] G.Scolieri[ac] E.S.Seo[o] V.Shoutko[l] E.Shoumilov[ab] R.Siedling[a] D.Son[ae] T.Song[h] M.Steuer[l] G.S.Sun[h] H.Suter[ag] X.W.Tang[i] Samuel C.C.Ting[l] S.M.Ting[l] M.Tornikoski[u] J.Torsti[af] J.Trümper[q] J.Ulbricht[ag] S.Urpo[u] I.Usoskin[z] E.Valtonen[af] J.Vandenhirtz[a] F.Velcea[ac,1] E.Velikhov[aa] B.Verlaat[ag,3] I.Vetlitsky[ab] F.Vezzu[s] J.P.Vialle[c] G.Viertel[ag] D.Vité[r] H.Von Gunten[ag] S.Waldmeier Wicki[ag] W.Wallraff[a] B.C.Wang[x] J.Z.Wang[g] Y.H.Wang[ad] K.Wiik[u] C.Williams[j] S.X.Wu[l,m] P.C.Xia[h] J.L.Yan[g] L.G.Yan[h] C.G.Yang[i] M.Yang[i] S.W.Ye[t,4] P.Yeh[ad] Z.Z.Xu[t] H.Y.Zhang[f] Z.P.Zhang[t] D.X.Zhao[h] G.Y.Zhu[i] W.Z.Zhu[g] H.L.Zhuang[i] A.Zichichi[j] B.Zimmermann[ag]

[a] I. Physikalisches Institut, RWTH, D-52056 Aachen, Germany[5]

[b] III. Physikalisches Institut, RWTH, D-52056 Aachen, Germany[5]

[c] Laboratoire d'Annecy-le-Vieux de Physique des Particules, LAPP, F-74941 Annecy-le-Vieux CEDEX, France
[e] Louisiana State University, Baton Rouge, LA 70803, USA
[d] Johns Hopkins University, Baltimore, MD 21218, USA
[f] Center of Space Science and Application, Chinese Academy of Sciences, 100080 Beijing, China
[g] Chinese Academy of Launching Vehicle Technology, CALT, 100076 Beijing, China
[h] Institute of Electrical Engineering, IEE, Chinese Academy of Sciences, 100080 Beijing, China
[i] Institute of High Energy Physics, IHEP, Chinese Academy of Sciences, 100039 Beijing, China[6]
[j] University of Bologna and INFN-Sezione di Bologna, I-40126 Bologna, Italy
[k] Institute of Microtechnology, Politechnica University of Bucharest and University of Bucharest, R-76900 Bucharest, Romania
[l] Massachusetts Institute of Technology, Cambridge, MA 02139, USA
[m] National Central University, Chung-Li, Taiwan 32054
[n] Laboratorio de Instrumentacao e Fisica Experimental de Particulas, LIP, P-3000 Coimbra, Portugal
[o] University of Maryland, College Park, MD 20742, USA
[p] INFN Sezione di Firenze, I-50125 Florence, Italy
[q] Max–Plank Institut fur Extraterrestrische Physik, D-85740 Garching, Germany
[r] University of Geneva, CH-1211 Geneva 4, Switzerland
[s] Institut des Sciences Nucleaires, F-38026 Grenoble, France
[t] Chinese University of Science and Technology, USTC, Hefei, Anhui 230 029, China[6]
[u] Helsinki University of Technology, FIN-02540 Kylmala, Finland
[v] Instituto Superior Técnico, IST, P-1096 Lisboa, Portugal
[w] Laboratorio de Instrumentacao e Fisica Experimental de Particulas, LIP, P-1000 Lisboa, Portugal
[x] Chung–Shan Institute of Science and Technology, Lung-Tan, Tao Yuan 325, Taiwan
[y] Centro de Investigaciones Energéticas, Medioambientales y Tecnologícas, CIEMAT, E-28040 Madrid, Spain[7]
[z] INFN-Sezione di Milano, I-20133 Milan, Italy
[aa] Kurchatov Institute, Moscow, 123182 Russia
[ab] Institute of Theoretical and Experimental Physics, ITEP, Moscow, 117259 Russia
[ac] INFN-Sezione di Perugia and Universitá Degli Studi di Perugia, I-06100 Perugia, Italy[8]
[ad] Academia Sinica, Taipei 11529, Taiwan
[ae] Kyungpook National University, 702-701 Taegu, Korea
[af] University of Turku, FIN-20014 Turku, Finland
[ag] Eidgenössische Technische Hochschule, ETH Zürich, CH-8093 Zürich, Switzerland
[1] Permanent address: HEPPG, Univ. of Bucharest, Romania.
[2] Permanent address: Nuclear Physics Institute, St. Petersburg, Russia.
[3] Now at National Institute for High Energy Physics, NIKHEF, NL-1009 DB Amsterdam, The Netherlands.
[4] Supported by ETH Zürich.
[5] Supported by the Deutsches Zentrum für Luft– und Raumfahrt, DLR.
[6] Supported by the National Natural Science Foundation of China.
[7] Also supported by the Comisión Interministerial de Ciencia y Tecnología.
[8] Also supported by the Italian Space Agency.

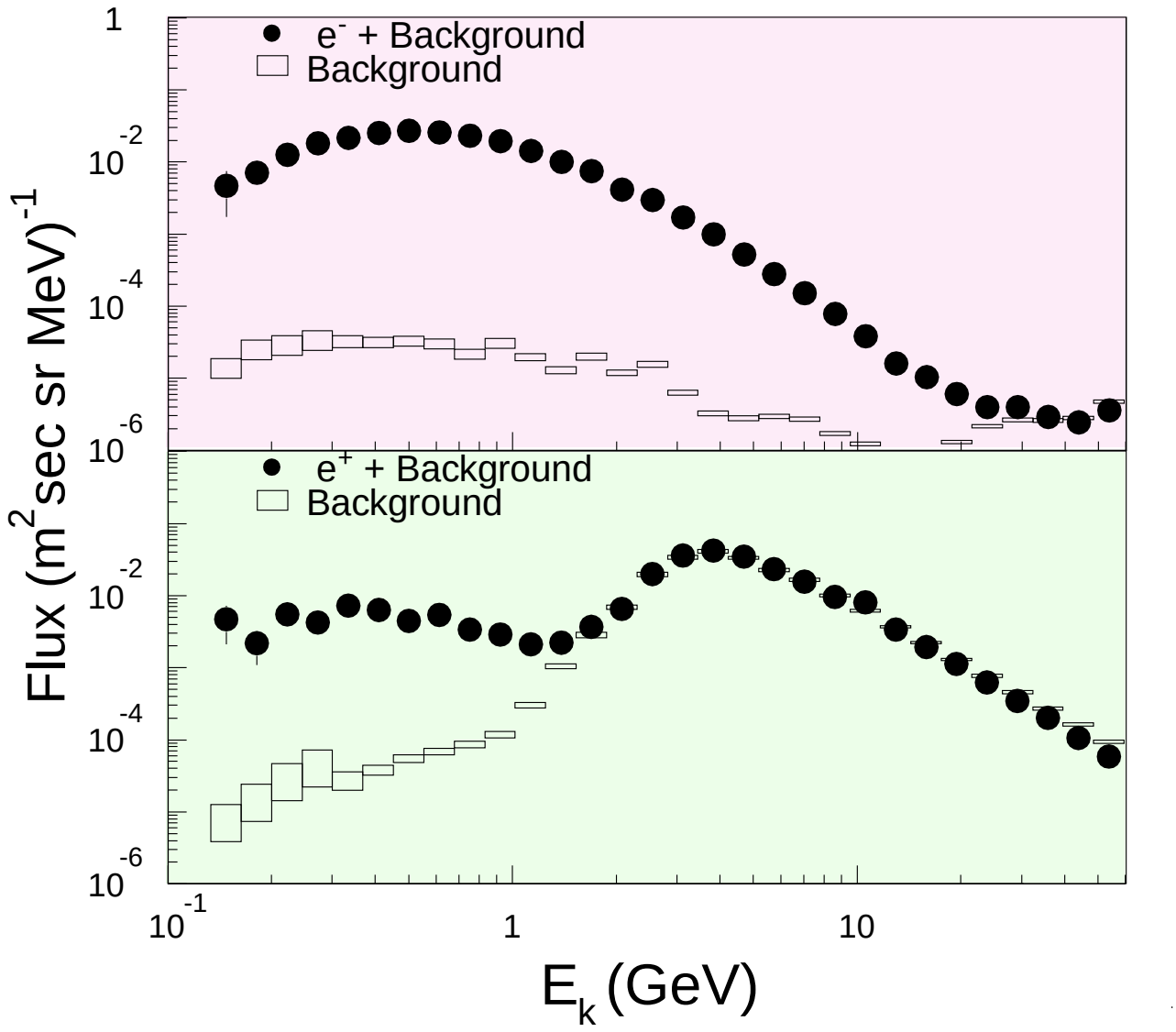

Figure 1: The primary $e^{\pm}$ fluxes and background in the geomagnetic polar region ($\Theta_M > 0.9$).

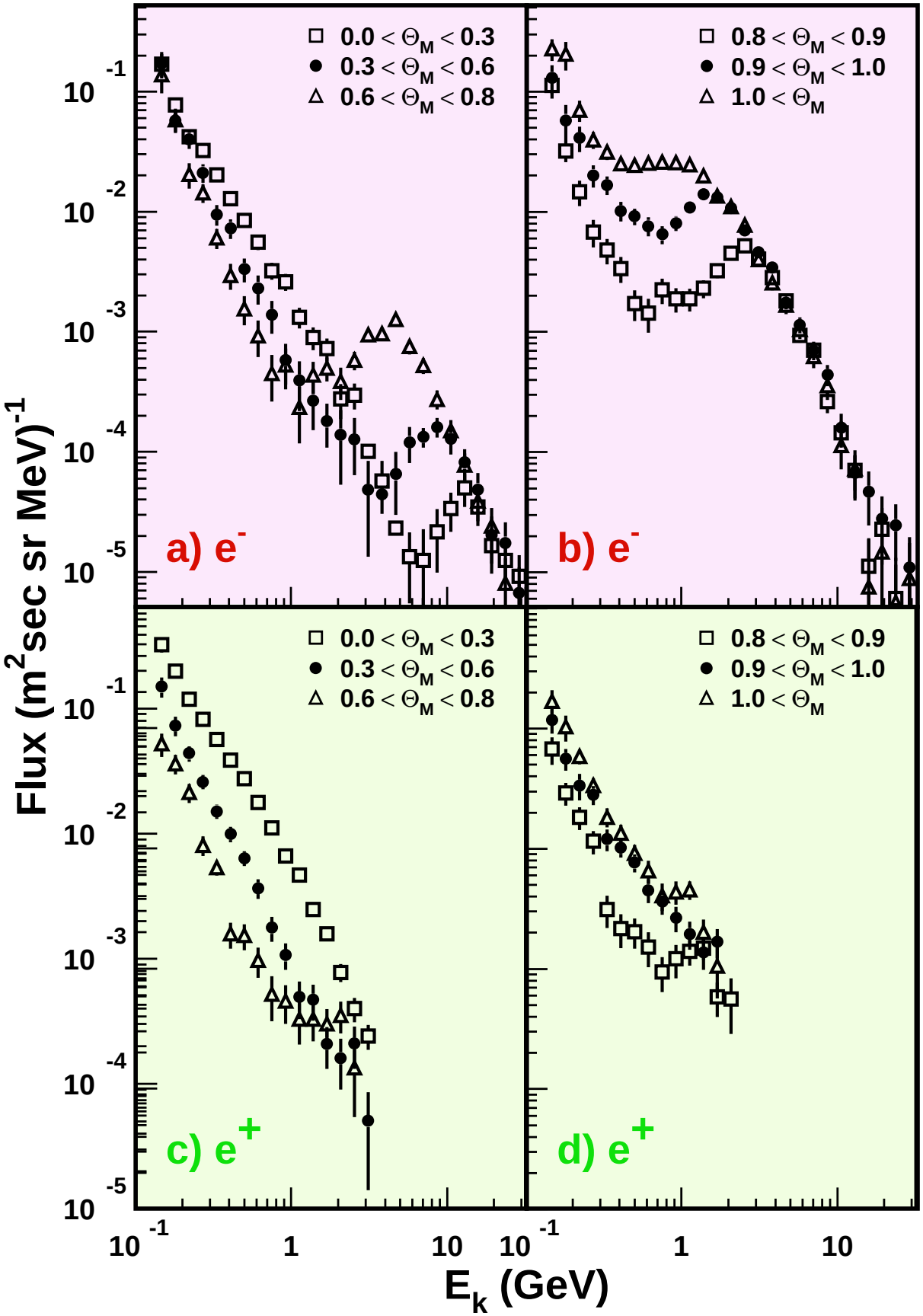

Figure 2: (a,b) Flux spectra for downward going electrons and (c,d) positrons, separated according to the geomagnetic latitude at which they were detected.

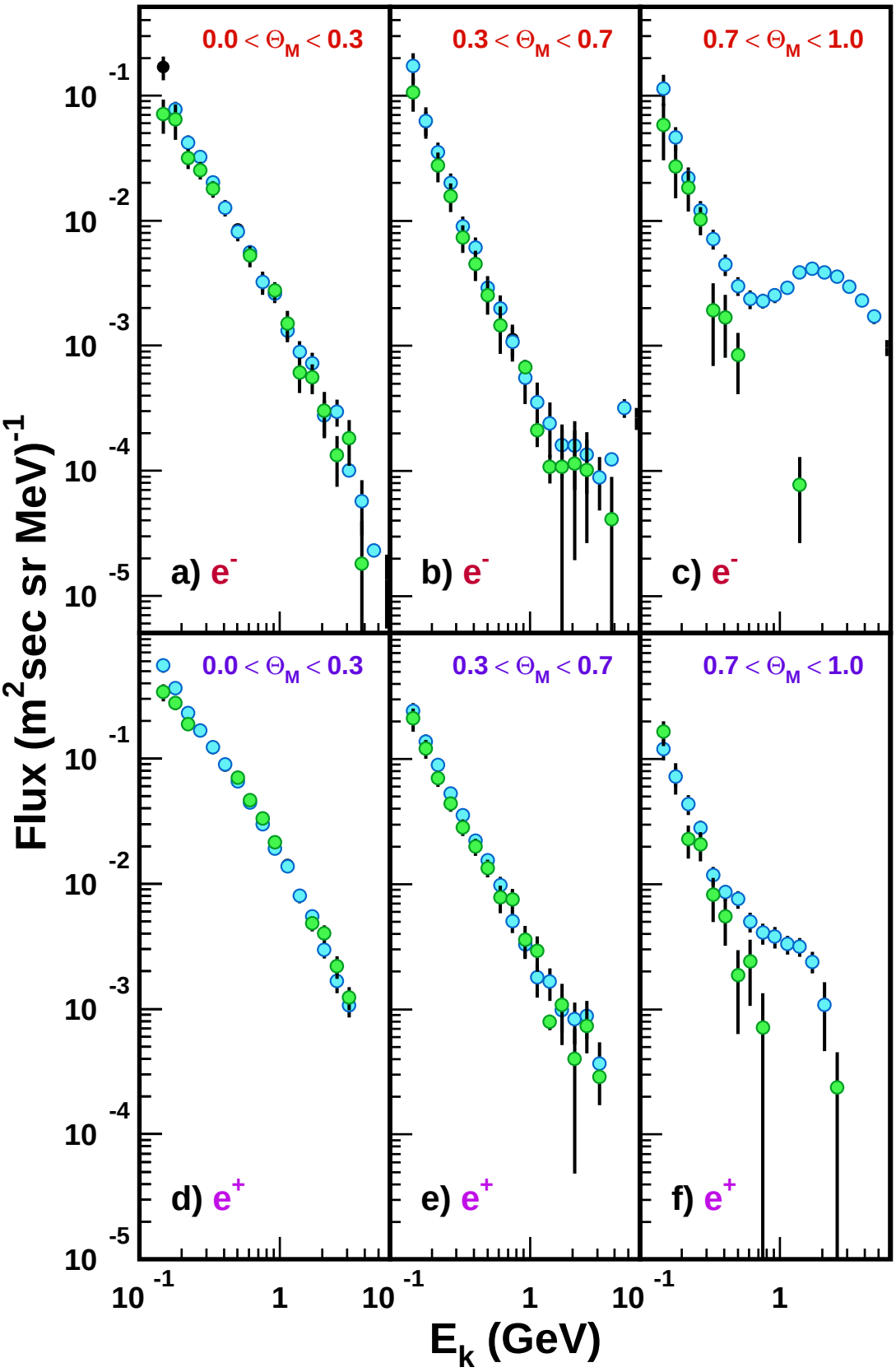

Figure 3: (a,b,c) Flux spectra for downward (blue circles) and upward (green circles) going electrons and (d,e,f) positrons, separated according to the geomagnetic latitude, Θ_M, at which they were detected.

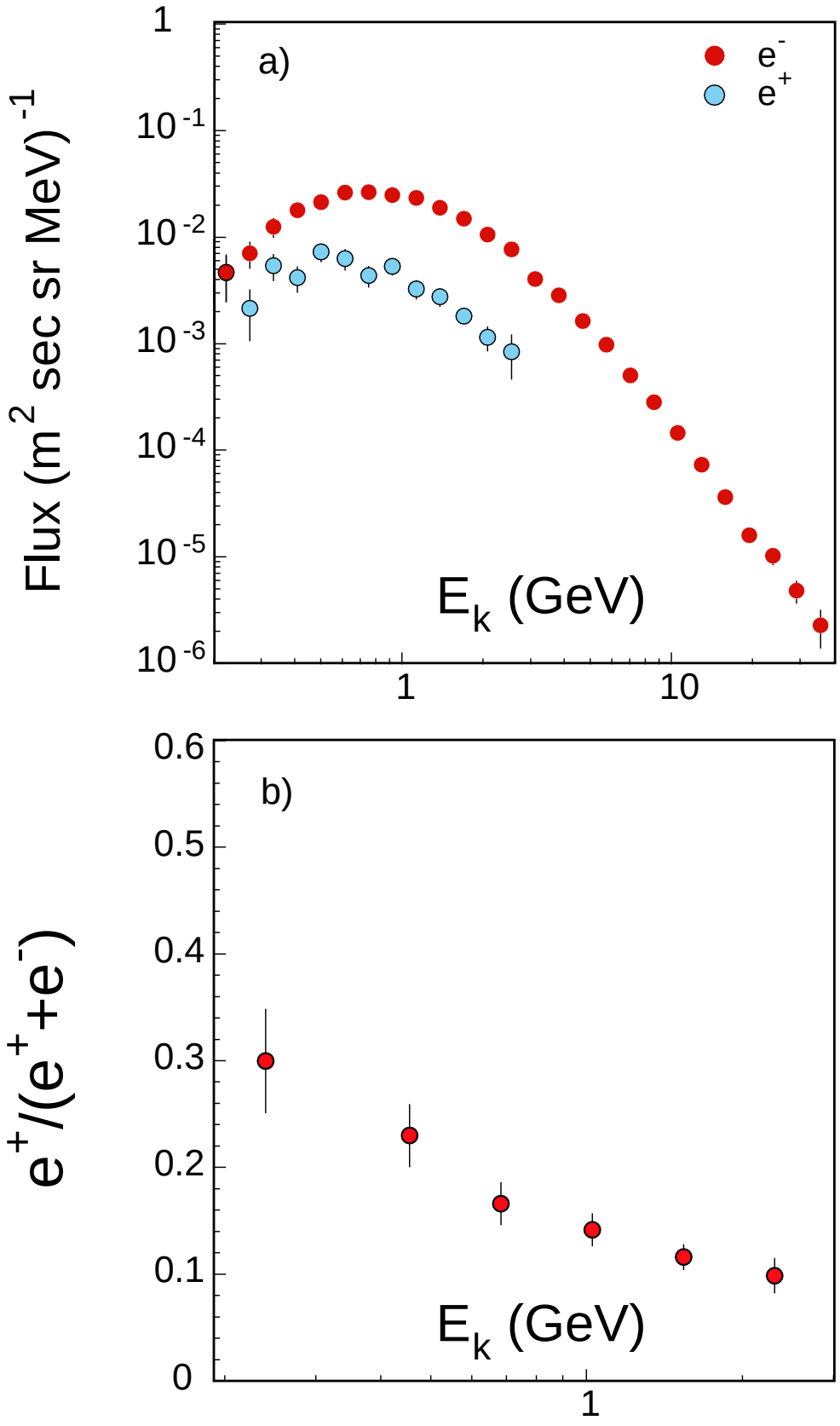

Figure 4: (a) Flux spectra for primary leptons. Particle direction within 25° of zenith. (b) Positron fraction for primary leptons versus energy.

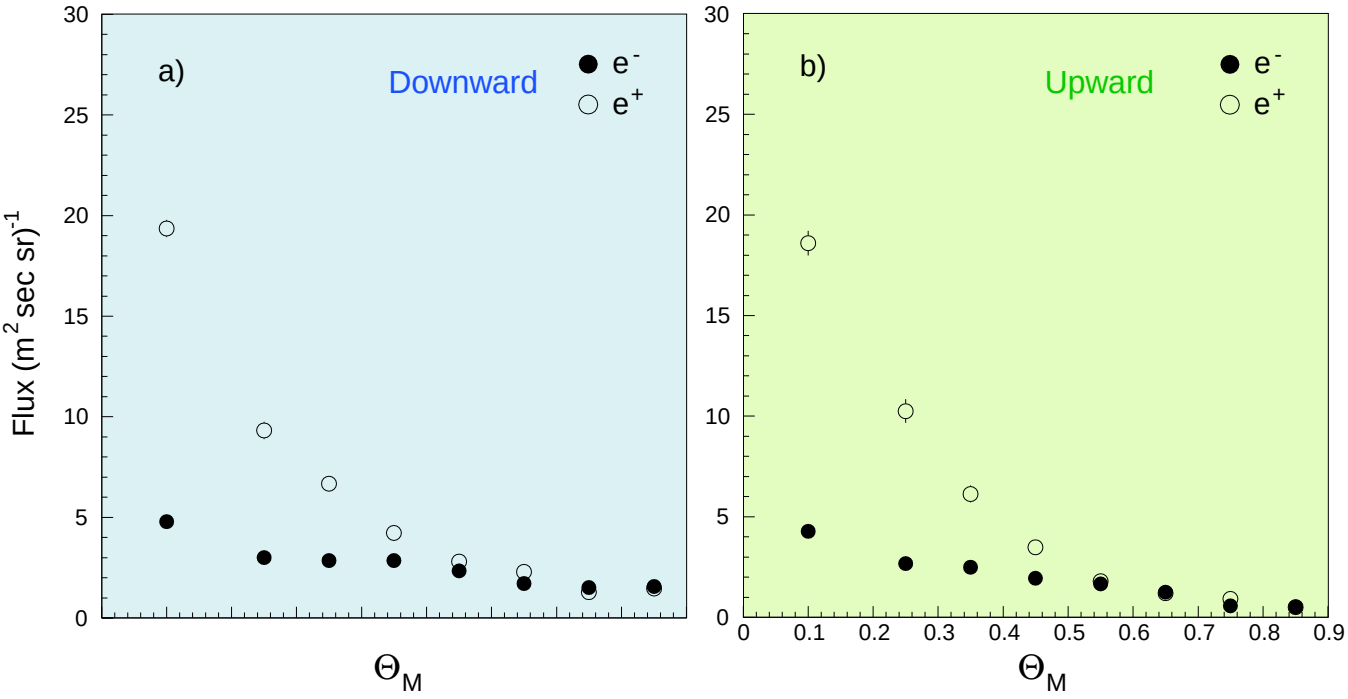

Figure 5: Properties of second lepton spectra flux: (a) downward and (b) upward going electrons and positrons as functions of the geomagnetic latitude, Θ_M, at which they were detected integrated over the range 0.2-2.5 GeV.

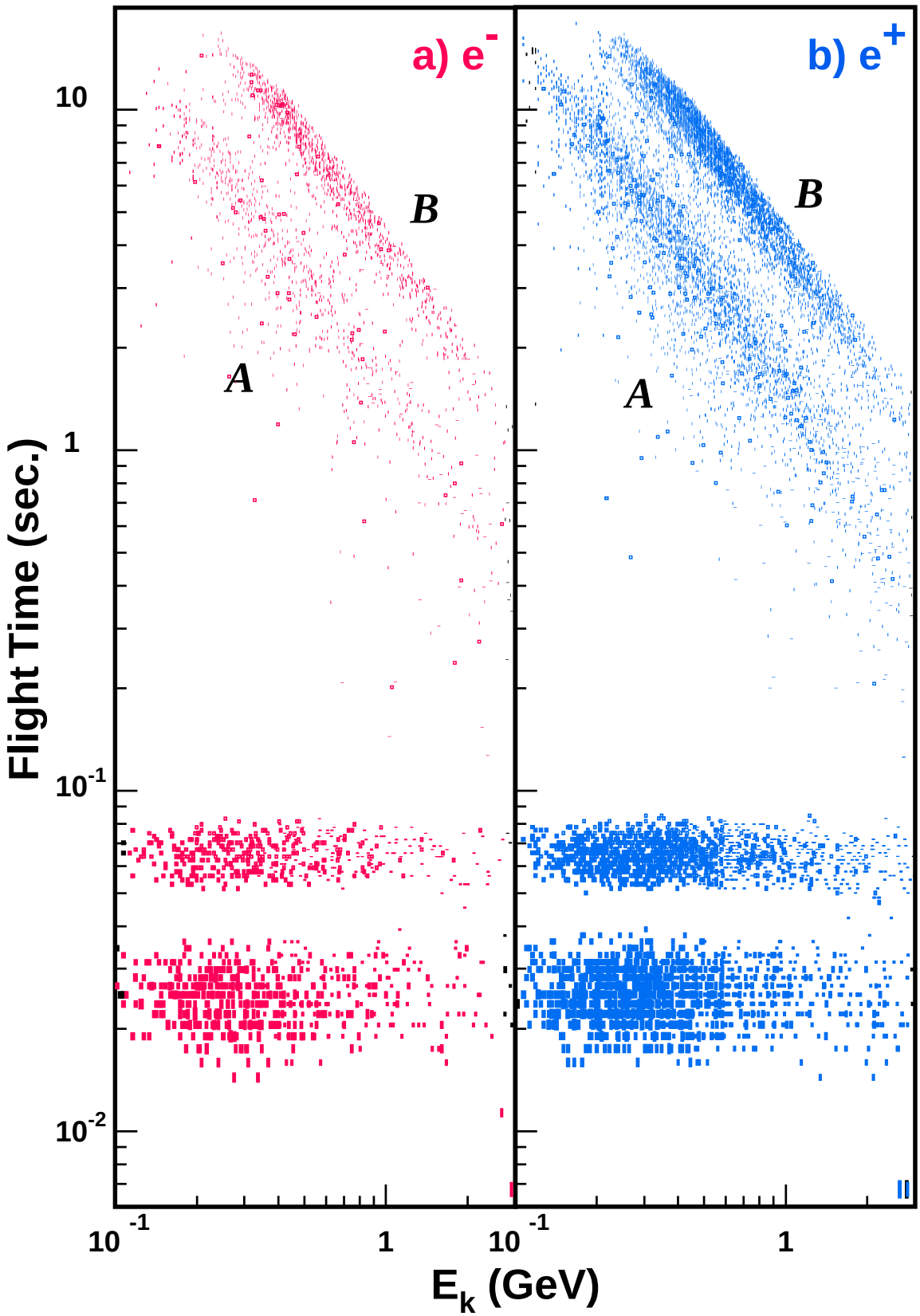

Figure 6: The flight time versus energy from the tracing of leptons detected in the region $\Theta_M < 0.3$. From the flight time distribution there are two distinct types of trajectories: For "short–lived", flight times < 0.2 sec, the flight time is independent of lepton energy. For "long–lived", flight times ≥ 0.2 sec, there are two bands *A* and *B*. In both *A* and *B* the flight time depends on energy: it decreases with increasing energy.

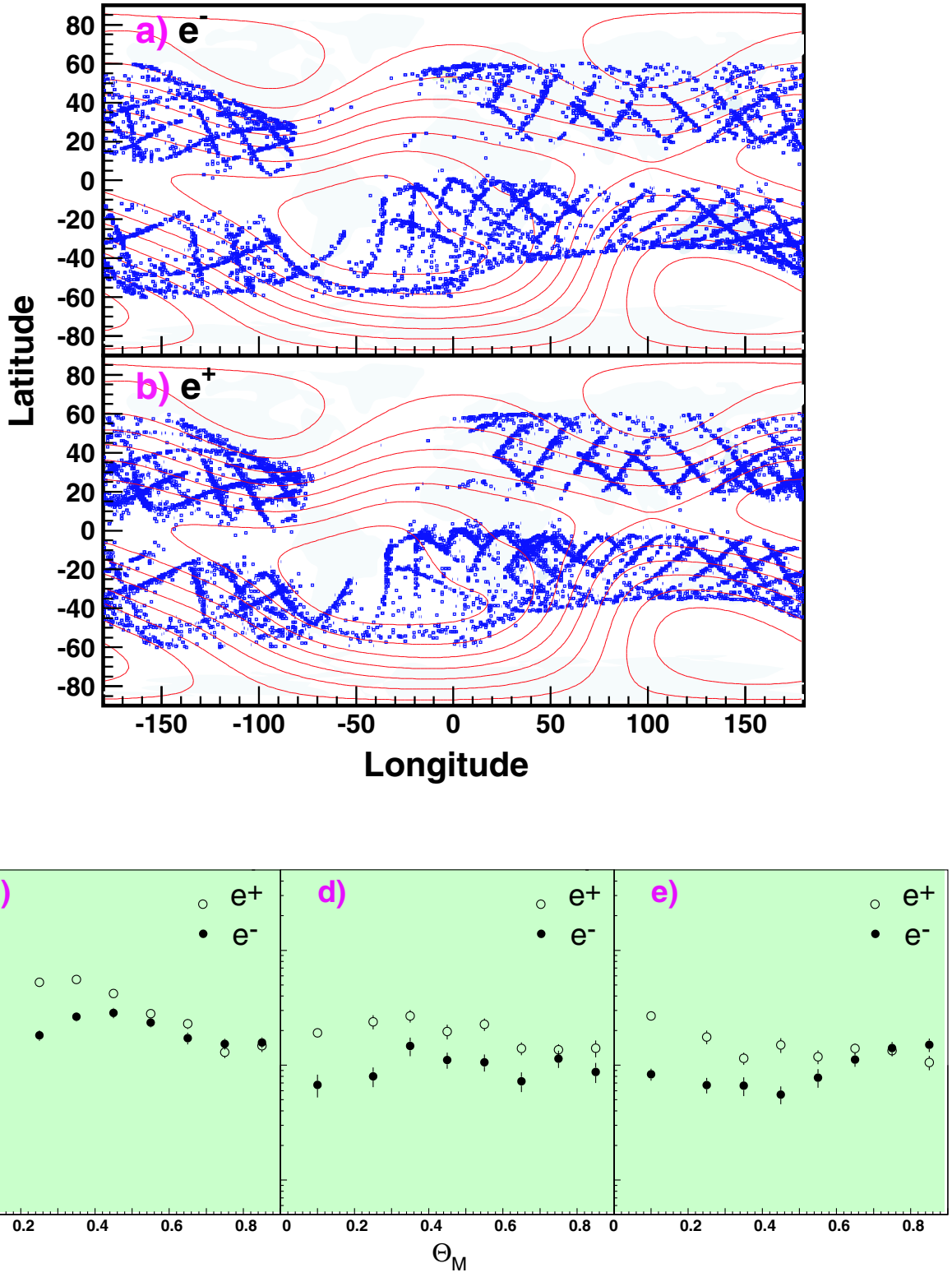

Figure 7: Properties of short–lived second spectra leptons (< 3 GeV): (a) The geographic origin of electrons and (b) positrons. Note that the point of origin shows no longitudinal dependence and that the short–lived leptons do not originate from the region $\Theta_M < 0.4$. The lines indicate the geomagnetic field contours at 380 km. (c) The e^- (full circles) and e^+ (open circles) fluxes integrated over the range 0.2-2.5 GeV as a function of magnetic latitude for zenith, (d) 20° and (e) 45° shuttle attitude.

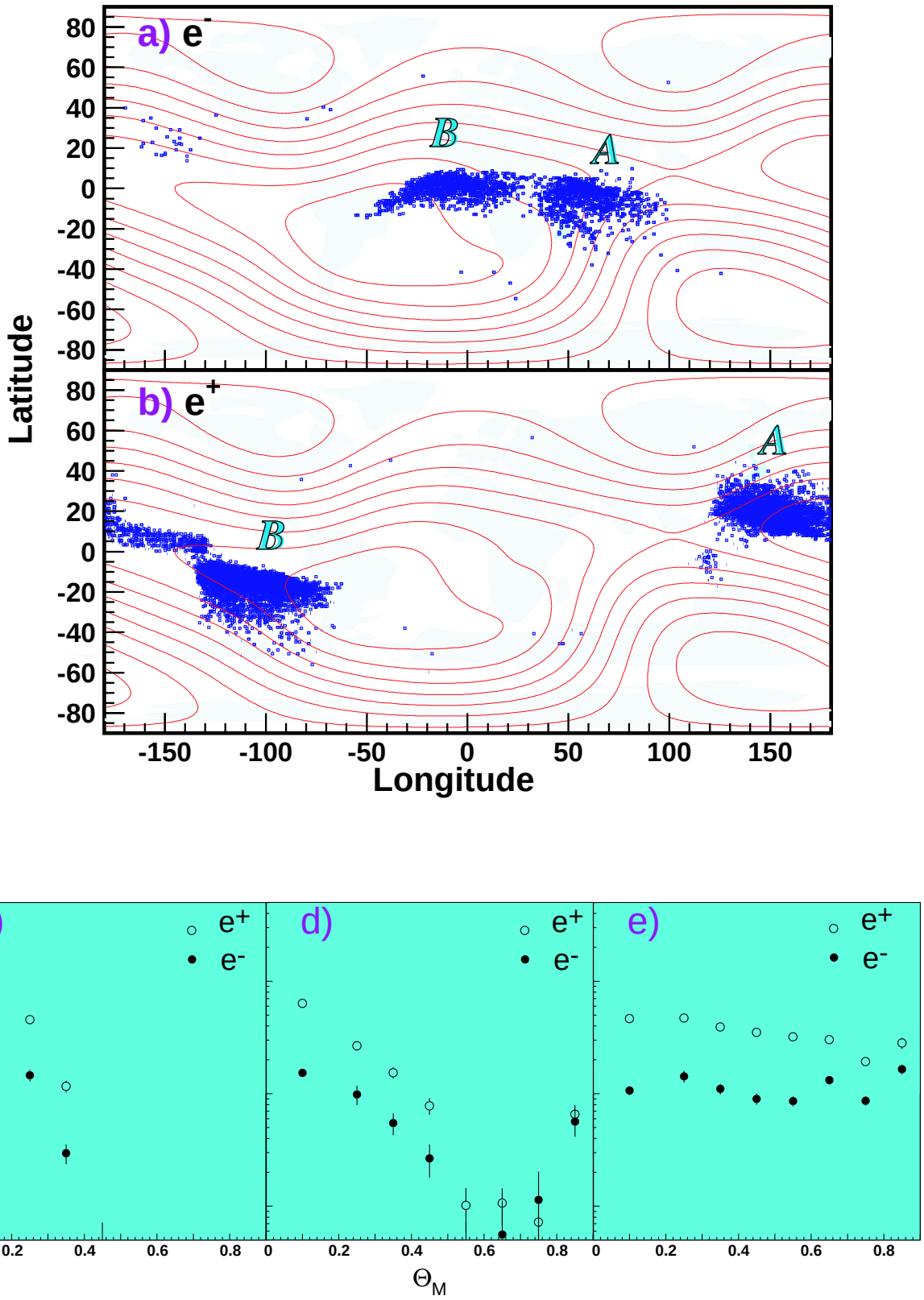

Figure 8: Properties of long–lived second spectra leptons (< 3 GeV): (a) The geographical origin of electrons and (b) positrons. The lines indicate the geomagnetic field contours at 380 km. The regions *A* and *B* correspond to the bands *A* and *B* marked in Fig. 6. (c) The e^- (full circles) and e^+ (open circles) fluxes integrated over the range 0.2-2.5 GeV as a function of magnetic latitude for zenith, (d) 20° and (e) 45° shuttle attitude.

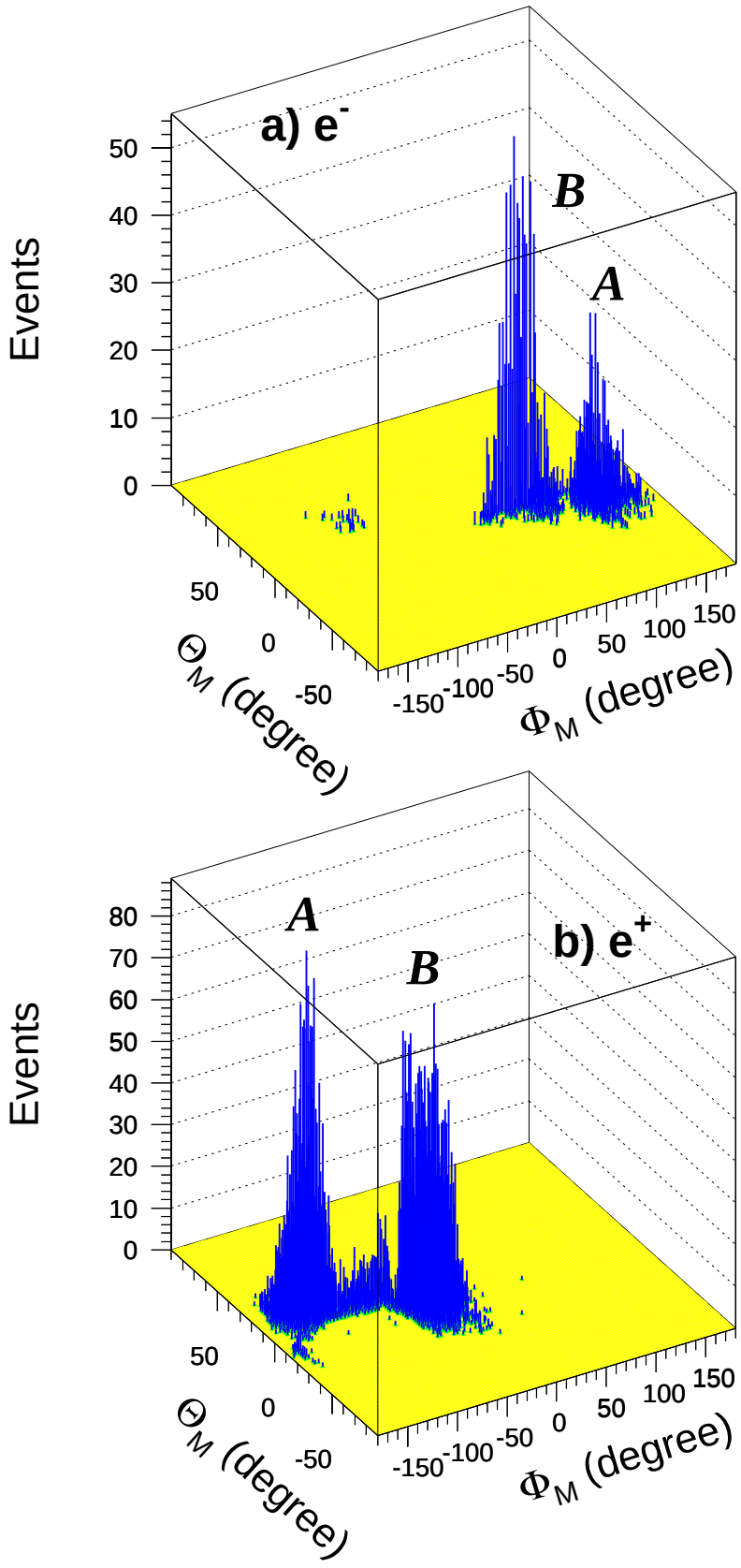

Figure 9: Property of second spectra: The point of origin of long–lived leptons with energies < 3 GeV and $\Theta_M < 0.7$ in geomagnetic coordinates. The regions *A* and *B* correspond to those in Fig. 8 and the bands marked *A* and *B* in Fig. 6.

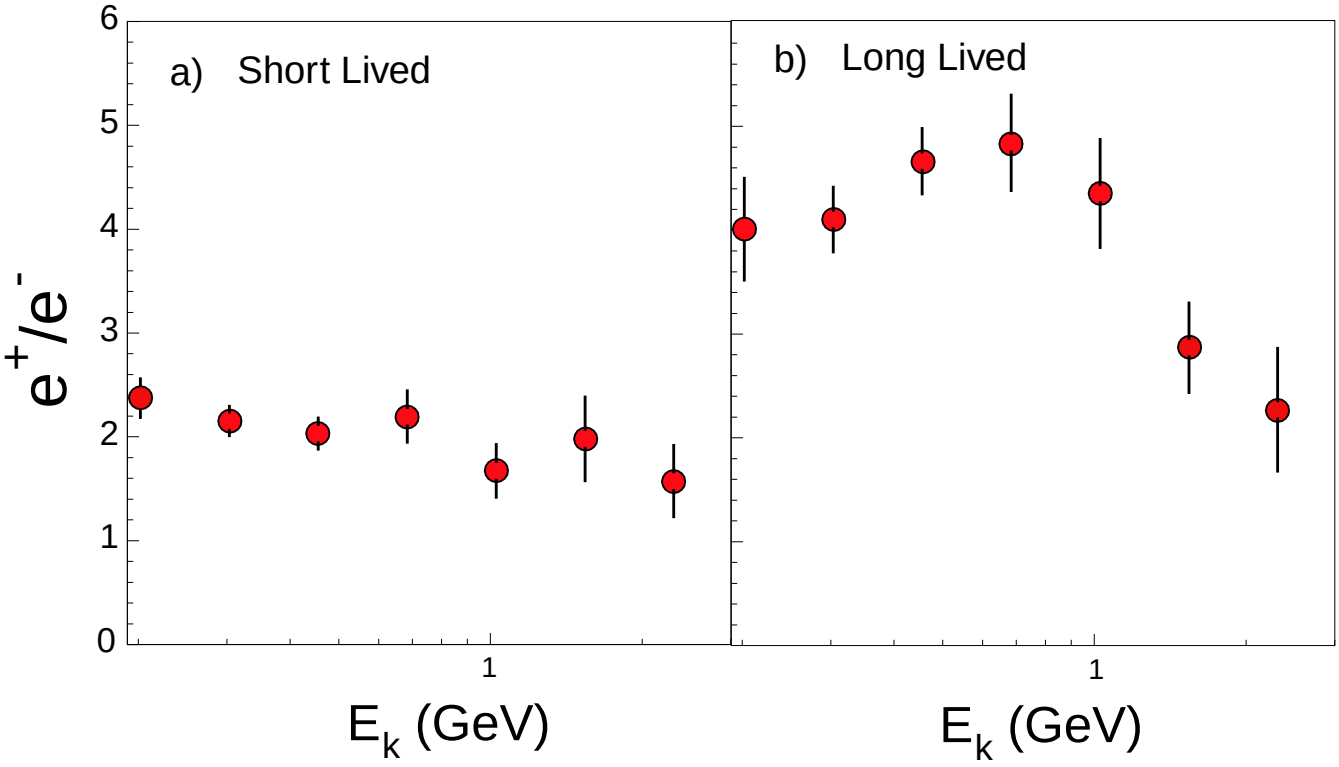

Figure 10: Property of second spectra: The e^+/e^- ratio as a function of energy for (a) short–lived and (b) long–lived particles. Shuttle attitude 0° and $\Theta_M < 0.3$.

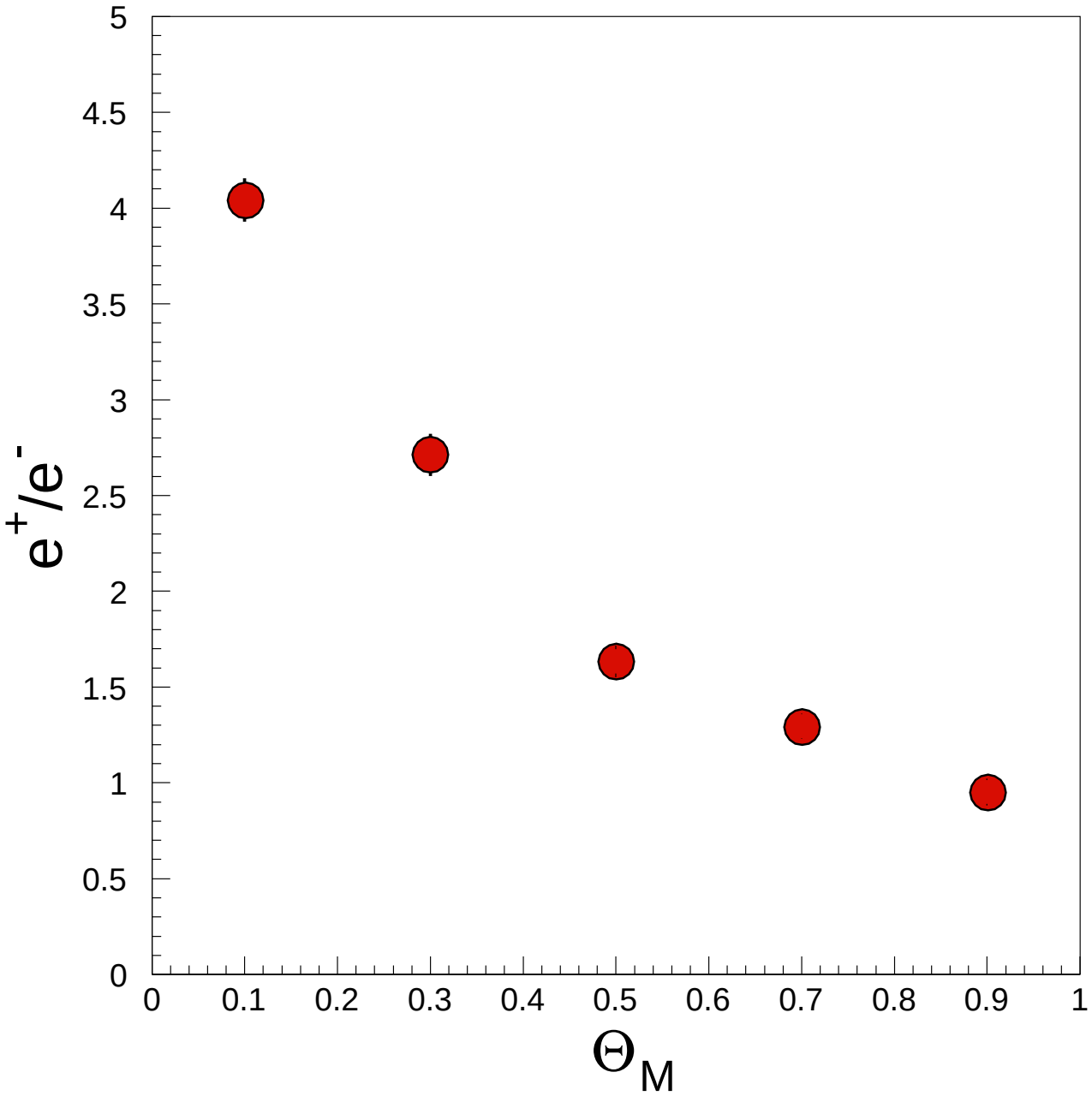

Figure 11: Property of second spectra: The e^+/e^- ratio as a function of magnetic latitude integrated over the range 0.2-2.5 GeV and combined for short–lived and long–lived leptons independent of shuttle attitude.

AMS paper 03 "Leptons in Near Earth Orbit"
Physics Letters B 484 (2000) 10-22
Referee report :

"This paper supplies entirely new data of the highest quality on electrons and positrons of cosmic rays in the magnetosphere and it is surely worth immediate publication. I do have a few recommendations as follows:

Page 5 and 6 and figure 8 and figure 9: --- I consider it very appropriate for the authors to point out that the behaviour of positrons and protons in the magnetosphere is very similar if not identical as can be seen by comparison to the AMS paper (ref. 9, Physics Letter B 472, 215, 2000) in particular figures 5 and 6 there.

Page 6, third line from below: --- reaching a maximum value of ~ 5 ... add: at ~ 700 MeV.

Page 17, figure 8a) e-: --- at latitude ~ 30 and longitude ~ -160 there is a little particle cluster shown, which appears also in figure 9a) at the appropriate geomagnetic position --- my question is: is this a real effect or should the reader consider this as background since neither in the text nor in the figure caption there is any comment on those particles."

Attachment IV

Cosmic Protons

The AMS Collaboration

Abstract

The primary proton spectrum in the kinetic energy range 0.2 to 200 GeV was measured by the Alpha Magnetic Spectrometer (AMS) during space shuttle flight STS–91 at an altitude of 380 km. The complete data set combining three shuttle attitudes and including all known systematic effects is presented.

Published in Phys. Lett. B490 (28 Sep 2000) 27-35

Referee's report attached.

Introduction

Accurate measurements of primary cosmic ray spectra, particularly of protons, are important for atmospheric neutrinos studies and studies of neutrino oscillation phenomenon [1, 2].

The Alpha Magnetic Spectrometer (AMS) [3] is a high energy physics experiment scheduled for installation on the International Space Station. In preparation for this long duration mission, AMS flew a precursor mission on board of the space shuttle Discovery during flight STS–91 in June 1998. The high statistic measurements of the primary proton spectra by AMS, free from atmospheric corrections, provide reliable information for atmospheric neutrino flux calculations.

In a previous paper [4] we presented the general features of protons in near Earth orbit. Measuring the distribution as a function of energy and latitude enabled us to study the behaviour of the proton flux near Earth. Above the geomagnetic cutoff the observed spectrum can be parameterized by a power law [5]. Below the cutoff a substantial second spectrum concentrated at equatorial latitudes with a flux of $\sim 70\,\mathrm{m^{-2}sec^{-1}sr^{-1}}$ is observed. In near Earth orbit, between the atmosphere and the radiation belts, these second spectrum particles follow a complicated path in the Earth's magnetic field. This behaviour is different from that extrapolated from satellite observations in the radiation belts. It is also different from that extrapolated from balloon observations in the upper layer of the atmosphere. A striking feature of the second spectrum is that most of the protons originate from a very restricted geographic region.

In this paper all the available events are used to determine the primary proton spectrum. This increase in statistics enables us to present an accurate determination of the primary proton flux.

The AMS experiment on STS–91

The major elements of AMS as flown on STS–91 consisted of a permanent magnet, a six plane tracker, time of flight hodoscopes, a Cerenkov counter and anticoincidence counters. The AMS detector has been described elsewhere [4, 6].

For this study, events were collected in three periods during which the shuttle attitude was constrained, within 1°, to keep the AMS positive z–axis pointing within 0°, 20° and 45° of the zenith. The acceptance was restricted to events with an incident angle, θ, within 38° of the positive z–axis of AMS. The orbital inclination was 51.7° and the geodetic altitude during these periods ranged from 350 to 390 km. Data taken while orbiting in or near the South Atlantic Anomaly were excluded.

The response of the detector was simulated using the AMS detector simulation program, based on the GEANT package [7]. The effects of energy loss, multiple scattering, interactions, decays and the measured detector efficiency and resolution were included.

After the flight, the AMS detector was extensively calibrated at two accelerators: at GSI, Darmstadt, with helium and carbon beams at 600 incident angles and locations and 10^7 events, and at the CERN proton-synchrotron machine in the energy region of 2 to 14 GeV, with 1200 incident angles and locations and 10^8 events. This ensured that the performance of the detector and the analysis procedure were thoroughly understood.

Analysis

Proton events were reconstructed and selected as described in our earlier paper [4]. Then events with rigidity, $\mathrm{R} = pc/|Z|e$, well above the geomagnetic cutoff were selected:

$$\mathrm{R} > \mathrm{R}_C \times (1.2 + 2\sigma(\mathrm{R}_C))$$

where R_C was the maximum cutoff rigidity and $\sigma(R_C)$ was the measurement uncertainty at that rigidity. R_C was calculated in the dipole approximation for one second time intervals along the shuttle trajectory for the measured shuttle attitude. As protons are the dominant components in cosmic rays, after selecting events with $Z = +1$, the proton sample has only minor backgrounds which consist of charged pions and deuterons. The estimated fraction of charged pions, which are produced in the top part of AMS, with energy below 0.5 GeV is 1 %. Above this energy the fraction decreases rapidly with increasing energy. The deuteron abundance in cosmic rays above the geomagnetic cutoff is about 2 %. To remove low energy charged pions and deuterons, the measured mass was required to be within 3 standard deviations of the proton mass. This rejected about 3 % of the events while reducing the background contamination to negligible levels over all energies.

The proton fluxes were derived from the measured counting rates using the acceptance as a function of the proton momentum. Protons with different momenta and directions were generated via the Monte Carlo method, passed through the AMS detector simulation program and accepted if the trigger and reconstruction requirements were satisfied as for the data. The acceptance was found to be 0.15 m^2sr on average and only weakly momentum dependent. The acceptance was then corrected following an analysis of unbiased trigger events [1)] [4].

The observed primary proton spectrum was verified to be isotropic as seen in Fig. 1a where the spectra in kinetic energy, E_K, scaled by $E_K^{2.75}$ are compared for two intervals of incident angle to the detector, θ, and in Fig 1b, where the average fluxes are shown as functions of the incident angle. Both are in agreement with an isotropic distribution. Therefore the three data collection periods are combined to obtain a data set having a total of 5.6 million primary protons. Given the resulting small statistical errors, further detailed studies of the systematic effects were performed.

The first source of systematic error, ε_{sys1}, was due to trigger efficiency variations and event reconstruction accuracy variations, both of which are related to the background rates and detector temperatures at different times and at different shuttle locations and orientations and to the energy deposited by the proton in each detector layer. Above ~ 20 GeV this systematic error is nearly energy independent. The calculated average contributions are shown in Table 1, the total error from this origin is 3.5 %.

Source	Error (%)
Fast Trigger	1.5
Anti Trigger	1
Level3 TOF	2
Level3 Tracker	1.5
Track and Velocity Fit	1.5
Total	3.5

Table 1: Average systematics of the trigger and reconstruction, ε_{sys1}.

A second source of systematic effects, ε_{sys2}, arose from Monte Carlo corrections. These errors are energy dependent but uncorrelated between energy bins. The calculated average contributions are shown in Table 2 and total to 3 %. The contributions of ε_{sys1} and ε_{sys2} versus energy are detailed in Table 3.

A third source of systematics, ε_{sys3}, is from the unfolding used to obtain the incident differential spectrum from the measured spectrum based on resolution functions obtained by simulation. These

[1)] This analysis removes possible systematics of the Monte Carlo method [7]

Source	Error (%)
Particle interactions	1.5
Monte Carlo Statistics	1.5
Proton Selection	2
Geomagnetic Cutoff	0.5
Total	3.0

Table 2: Systematics of the Monte Carlo corrections leading to the energy dependent ε_{sys2}.

errors are bin to bin correlated. As detailed in Table 3, they are typically 1 % below ~ 20 GeV and reach 5 % at ~ 100 GeV.

Fig. 2 shows the primary proton spectrum with the statistical and three systematic errors combined in quadrature.

Verification of the systematic errors

A careful experimental verification of the calculated systematic errors was performed. The calculated error took into account the propagation of the statistical and three systematic errors. We present 6 examples:

(1) Fig. 3 shows the flux variation, $\delta \equiv$ (flux/average flux) $- 1$ as a function of energy, for the three data collection periods, corresponding to the three different shuttle orientations, compared with the systematic error calculated for this case.

(2) Fig. 4 shows the flux averaged above 20 GeV versus different intervals of the corrected geomagnetic latitude [8], Θ_M, at which the protons were detected compared with the systematic error calculated for this case.

(3) Fig. 5 shows the ratio of the flux with and without proton selection quality cuts. As seen, the variation is within the systematic error for this case.

(4) Fig. 6 shows the variation of the flux, δ, for events which had different lever arms in the tracker, corresponding to the number of tracker planes used in the fit. Again, the variation is within the range of the systematic errors for this case.

(5) The systematic error assigned to the unfolding was checked at several energies using the test beam measurements. Fig. 7a shows how the spectrum changes if the unfolding matrix is artificially varied by smearing the alignment between different tracker ladders by an additional 10 μm. At ~ 100 GeV this corresponds to varying the momentum resolution by 15 %.

(6) Fig. 7b gives an estimate of the accuracy of the unfolding method by comparing two completely different deconvolution techniques [9–11]:

A: The solution of an overdetermined system of linear equations by a method of converged weights [4].

B: "Classical" unfolding by regularization, namely minimization of the function [11]:

$$\left(\frac{\int f(x')K(x,x')dx' - g(x)}{\varepsilon(x)}\right)^2 + \alpha\left(\frac{d^2 f}{dx^2}\right)^2$$

where $g(x)$ is the measurement, $\varepsilon(x)$ its error, $K(k,x')$ is the resolution matrix, $f(x)$ is the solution and α is a regularization parameter. This method tends to give a smoother solution, since the searched function is *a priori* assumed to be a "smooth" one, with the most probable "smoothness" estimated from Bayes' theorem.

Up to ~ 100 GeV the two methods agree within 2-3 %. As the unfolding systematics were understood for both methods, the average of the two procedures was used. The input errors for both procedures were the corresponding statistical errors and the systematics of the resolution matrix used.[2)]

In these examples, and in all other cases, the assigned systematic errors were found to be correct.

Results

The primary proton spectrum together with the statistical and three systematic errors are presented in Table 3. For comparision with balloon measurements [12–15] the data has been scaled by $E_K^{2.5}$ as shown in Fig. 8. The flux scaled by $E_K^{2.75}$ is shown in Fig. 9. As seen from Fig. 9, our data is a smooth function which is flat above 20 GeV. This is a substantial deviation from the current estimates used to calculate atmospheric neutrinos [2].

Acknowledgements

The support of INFN, Italy, ETH–Zürich, the University of Geneva, the Chinese Academy of Sciences, Academia Sinica and National Central University, Taiwan, the RWTH–Aachen, Germany, the University of Turku, the University of Technology of Helsinki, Finland, the U.S. DOE and M.I.T., CIEMAT, Spain, LIP, Portugal and IN2P3, France, is gratefully acknowledged.

References

[1] Y. Fukuda *et al.,* Phys. Lett. **B436** (1998) 33–41.

[2] M. Honda *et al.,* Phys.Rev.D **52** (1995) 4985; G. Battistoni *et al.,* hep-ph/9907408 (1999); Y. Tserkovnyak *et al.,* hep-ph/9907450 (1999); P. Lipari, hep-ph/9905506 (1999); T. Gaisser, hep-ph/0001027 (2000); N. Fornengo *et al.,* hep-ph/0002147 (2000).

[3] S. Ahlen *et al.,* Nucl. Inst. Meth. **A350** (1994) 351.

[4] AMS Collaboration, J. Alcaraz *et al.,* Phys. Lett. **B472** (2000) 215–226.

[5] A. D. Erlykin *et al.,* Phys. Lett. **B482** (2000) 337–342.

[6] AMS Collaboration, J. Alcaraz *et al.,* Phys. Lett. **B461** (1999) 387–396.

[7] R. Brun *et al.,* GEANT 3, CERN DD/EE/84-1 (Revised, 1987); P. A. Aamio *et al.,* FLUKA Users Guide, CERN TIS-RP-190 (1990).

[2)] In our previous publication [4] the flux dependence on energy and latitude was presented. These fluxes cannot be combined as such since the errors are correlated through the systematics of the resolution matrix.

[8] A. Brekke, Physics of the Upper Polar Atmosphere, pp. 127–145, (Wiley, 1997).

[9] A. Kondor, Nucl. Inst. Meth. **216** (1983) 177; G. D'Agostini, Nucl. Inst. Meth. **A362** (1995) 487.

[10] V. Blobel, Unfolding Methods in High Energy Physics, in Proc. 1984 CERN School of Computing, CERN 85-09 (1985) 88–127.

[11] V. F. Turchin and V. A. Nozik, Izv. Acad. Nauk USSR ser. Fiz **5** (1969) 29; V. F. Turchin, V. P. Kozlov and M. S. Malkevich, Phys. Usp. **102, chap.4** (1970) 345.

[12] M. Boesio *et al.,* ApJ **518** (1999) 457.

[13] E. S. Seo *et al.,* ApJ **378** (1991) 763.

[14] T. Sanuki *et al.,* astro-ph/0002481 (2000).

[15] W. Menn *et al.,* ApJ **533** (2000) 281.

The AMS Collaboration

J.Alcaraz[y], B.Alpat[ac], G.Ambrosi[r], H.Anderhub[ag], L.Ao[g], A.Arefiev[ab], P.Azzarello[r], E.Babucci[ac], L.Baldini[j,l], M.Basile[j], D.Barancourt[s], F.Barao[w,v], G.Barbier[s], G.Barreira[w], R.Battiston[ac], R.Becker[l], U.Becker[l], L.Bellagamba[j], P.Béné[r], J.Berdugo[y], P.Berges[l], B.Bertucci[ac], A.Biland[ag], S.Bizzaglia[ac], S.Blasko[ac], G.Boella[z], M.Boschini[z], M.Bourquin[r], L.Brocco[j], G.Bruni[j], M.Buenerd[s], J.D.Burger[l], W.J.Burger[ac], X.D.Cai[l], C.Camps[b], P.Cannarsa[ag], M.Capell[l], D.Casadei[j], J.Casaus[y], G.Castellini[p], C.Cecchi[ac], Y.H.Chang[m], H.F.Chen[t], H.S.Chen[i], Z.G.Chen[g], N.A.Chernoplekov[aa], T.H.Chiueh[m], Y.L.Chuang[ad], F.Cindolo[j], V.Commichau[b], A.Contin[j], P.Crespo[w], M.Cristinziani[r], J.P.da Cunha[n], T.S.Dai[l], J.D.Deus[y], N.Dinu[ac,1], L.Djambazov[ag], I.D'Antone[j], Z.R.Dong[h], P.Emonet[r], J.Engelberg[u], F.J.Eppling[l], T.Eronen[af], G.Esposito[ac], P.Extermann[r], J.Favier[c], E.Fiandrini[ac], P.H.Fisher[l], G.Fluegge[b], N.Fouque[c], Yu.Galaktionov[ab,l], M.Gervasi[z], P.Giusti[j], D.Grandi[z], O.Grimm[ag], W.Q.Gu[h], K.Hangarter[b], A.Hasan[ag], V.Hermel[c], H.Hofer[ag], M.A.Huang[ad], W.Hungerford[ag], M.Ionica[ac,1], R.Ionica[ac,1], M.Jongmanns[ag], K.Karlamaa[u], W.Karpinski[a], G.Kenney[ag], J.Kenny[ac], W.Kim[ae], A.Klimentov[l,ab], R.Kossakowski[c], V.Koutsenko[l,ab], M.Kraeber[ag], G.Laborie[s], T.Laitinen[af], G.Lamanna[ac], G.Laurenti[j], A.Lebedev[l], S.C.Lee[ad], G.Levi[j], P.Levtchenko[ac,2], C.L.Liu[x], H.T.Liu[i], I.Lopes[n], G.Lu[g], Y.S.Lu[i], K.Lübelsmeyer[a], D.Luckey[l], W.Lustermann[ag], C.Mañ[y], A.Margotti[j], F.Mayet[s], R.R.McNeil[e], B.Meillon[s], M.Menichelli[ac], A.Mihul[k], A.Mourao[y], A.Mujunen[u], F.Palmonari[j], A.Papi[ac], I.H.Park[ae], M.Pauluzzi[ac], F.Pauss[ag], E.Perrin[r], A.Pesci[j], A.Pevsner[d], M.Pimenta[w,v], V.Plyaskin[ab], V.Pojidaev[ab], M.Pohl[r], V.Postolache[ac,1], N.Produit[r], P.G.Rancoita[z], D.Rapin[r], F.Raupach[a], D.Ren[ag], Z.Ren[ad], M.Ribordy[r], J.P.Richeux[r], E.Riihonen[af], J.Ritakari[u], U.Roeser[ag], C.Roissin[s], R.Sagdeev[o], G.Sartorelli[j], A.Schultz von Dratzig[a], G.Schwering[a], G.Scolieri[ac], E.S.Seo[o], V.Shoutko[l], E.Shoumilov[ab], R.Siedling[a], D.Son[ae], T.Song[h], M.Steuer[l], G.S.Sun[h], H.Suter[ag], X.W.Tang[i], Samuel C.C.Ting[l], S.M.Ting[l], M.Tornikoski[u], J.Torsti[af], J.Trümper[q], J.Ulbricht[ag], S.Urpo[u], I.Usoskin[z], E.Valtonen[af], J.Vandenhirtz[a], F.Velcea[ac,1], E.Velikhov[aa], B.Verlaat[ag,3], I.Vetlitsky[ab], F.Vezzu[s], J.P.Vialle[c], G.Viertel[ag], D.Vité[r], H.Von Gunten[ag], S.Waldmeier Wicki[ag], W.Wallraff[a], B.C.Wang[x], J.Z.Wang[g], Y.H.Wang[ad], K.Wiik[u], C.Williams[j], S.X.Wu[l,m], P.C.Xia[h], J.L.Yan[g], L.G.Yan[h], C.G.Yang[i], M.Yang[i], S.W.Ye[t,4], P.Yeh[ad], Z.Z.Xu[t], H.Y.Zhang[f], Z.P.Zhang[t], D.X.Zhao[h], G.Y.Zhu[i], W.Z.Zhu[g], H.L.Zhuang[i], A.Zichichi[j], B.Zimmermann[ag]

---

[a] I. Physikalisches Institut, RWTH, D-52056 Aachen, Germany[5]

[b] III. Physikalisches Institut, RWTH, D-52056 Aachen, Germany[5]

[c] Laboratoire d'Annecy-le-Vieux de Physique des Particules, LAPP, F-74941 Annecy-le-Vieux CEDEX, France

[e] Louisiana State University, Baton Rouge, LA 70803, USA

[d] Johns Hopkins University, Baltimore, MD 21218, USA

[f] Center of Space Science and Application, Chinese Academy of Sciences, 100080 Beijing, China

[g] Chinese Academy of Launching Vehicle Technology, CALT, 100076 Beijing, China

[h] Institute of Electrical Engineering, IEE, Chinese Academy of Sciences, 100080 Beijing, China

[i] Institute of High Energy Physics, IHEP, Chinese Academy of Sciences, 100039 Beijing, China[6]

[j] University of Bologna and INFN-Sezione di Bologna, I-40126 Bologna, Italy

[k] Institute of Microtechnology, Politechnica University of Bucharest and University of Bucharest, R-76900 Bucharest, Romania

[l] Massachusetts Institute of Technology, Cambridge, MA 02139, USA

[m] National Central University, Chung-Li, Taiwan 32054

[n] Laboratorio de Instrumentacao e Fisica Experimental de Particulas, LIP, P-3000 Coimbra, Portugal

[o] University of Maryland, College Park, MD 20742, USA

[p] INFN Sezione di Firenze, I-50125 Florence, Italy

[q] Max–Plank Institut fur Extraterrestrische Physik, D-85740 Garching, Germany

[r] University of Geneva, CH-1211 Geneva 4, Switzerland

[s] Institut des Sciences Nucleaires, F-38026 Grenoble, France
[t] Chinese University of Science and Technology, USTC, Hefei, Anhui 230 029, China[6]
[u] Helsinki University of Technology, FIN-02540 Kylmala, Finland
[v] Instituto Superior Técnico, IST, P-1096 Lisboa, Portugal
[w] Laboratorio de Instrumentacao e Fisica Experimental de Particulas, LIP, P-1000 Lisboa, Portugal
[x] Chung–Shan Institute of Science and Technology, Lung-Tan, Tao Yuan 325, Taiwan
[y] Centro de Investigaciones Energéticas, Medioambientales y Tecnologícas, CIEMAT, E-28040 Madrid, Spain[7]
[z] INFN-Sezione di Milano, I-20133 Milan, Italy
[aa] Kurchatov Institute, Moscow, 123182 Russia
[ab] Institute of Theoretical and Experimental Physics, ITEP, Moscow, 117259 Russia
[ac] INFN-Sezione di Perugia and Universitá Degli Studi di Perugia, I-06100 Perugia, Italy[8]
[ad] Academia Sinica, Taipei 11529, Taiwan
[ae] Kyungpook National University, 702-701 Taegu, Korea
[af] University of Turku, FIN-20014 Turku, Finland
[ag] Eidgenössische Technische Hochschule, ETH Zürich, CH-8093 Zürich, Switzerland
[1] Permanent address: HEPPG, Univ. of Bucharest, Romania.
[2] Permanent address: Nuclear Physics Institute, St. Petersburg, Russia.
[3] Now at National Institute for High Energy Physics, NIKHEF, NL-1009 DB Amsterdam, The Netherlands.
[4] Supported by ETH Zürich.
[5] Supported by the Deutsches Zentrum für Luft– und Raumfahrt, DLR.
[6] Supported by the National Natural Science Foundation of China.
[7] Also supported by the Comisión Interministerial de Ciencia y Tecnología.
[8] Also supported by the Italian Space Agency.

Kinetic Energy	Flux $\pm \varepsilon_{stat} \pm \varepsilon_{sys1} \pm \varepsilon_{sys2} \pm \varepsilon_{sys3}$
0.22 – 0.31	$(154. \pm 1.6 \pm 5.9 \pm 4.0 \pm 1.9) \times 10^{-2}$
0.31 – 0.44	$(156. \pm .99 \pm 6.0 \pm 3.8 \pm 1.3) \times 10^{-2}$
0.44 – 0.62	$(143. \pm .59 \pm 6.0 \pm 3.6 \pm 1.0) \times 10^{-2}$
0.62 – 0.85	$(120. \pm .39 \pm 4.6 \pm 3.1 \pm .82) \times 10^{-2}$
0.85 – 1.15	$(966. \pm 2.6 \pm 37. \pm 24. \pm 6.7) \times 10^{-3}$
1.15 – 1.54	$(738. \pm 1.8 \pm 28. \pm 18. \pm 5.1) \times 10^{-3}$
1.54 – 2.02	$(533. \pm 1.2 \pm 20. \pm 13. \pm 3.4) \times 10^{-3}$
2.02 – 2.62	$(372. \pm .80 \pm 14. \pm 8.9 \pm 2.7) \times 10^{-3}$
2.62 – 3.38	$(247. \pm .53 \pm 9.5 \pm 5.8 \pm 1.8) \times 10^{-3}$
3.38 – 4.31	$(161. \pm .33 \pm 6.2 \pm 3.7 \pm 1.3) \times 10^{-3}$
4.31 – 5.45	$(101. \pm .20 \pm 3.9 \pm 2.3 \pm .74) \times 10^{-3}$
5.45 – 6.86	$(630. \pm 1.3 \pm 24. \pm 14. \pm 5.2) \times 10^{-4}$
6.86 – 8.60	$(378. \pm .84 \pm 14. \pm 8.6 \pm 3.3) \times 10^{-4}$
8.60 – 10.7	$(226. \pm .54 \pm 8.7 \pm 5.2 \pm 2.0) \times 10^{-4}$
10.7 – 13.3	$(135. \pm .36 \pm 5.2 \pm 3.1 \pm 1.5) \times 10^{-4}$
13.3 – 16.5	$(786. \pm 2.3 \pm 30. \pm 18. \pm 10.) \times 10^{-5}$
16.5 – 20.5	$(449. \pm 1.5 \pm 17. \pm 11. \pm 6.6) \times 10^{-5}$
20.5 – 25.3	$(266. \pm .98 \pm 10. \pm 6.4 \pm 4.3) \times 10^{-5}$
25.3 – 31.2	$(148. \pm .61 \pm 5.7 \pm 3.7 \pm 2.7) \times 10^{-5}$
31.2 – 38.4	$(856. \pm 4.0 \pm 33. \pm 22. \pm 16.) \times 10^{-6}$
38.4 – 47.3	$(496. \pm 2.7 \pm 19. \pm 13. \pm 9.2) \times 10^{-6}$
47.3 – 58.2	$(284. \pm 1.8 \pm 11. \pm 7.9 \pm 5.7) \times 10^{-6}$
58.2 – 71.5	$(154. \pm 1.2 \pm 5.9 \pm 4.4 \pm 3.0) \times 10^{-6}$
71.5 – 87.8	$(86.2 \pm .80 \pm 3.3 \pm 2.4 \pm 1.7) \times 10^{-6}$
87.8 – 108.	$(49.4 \pm .55 \pm 1.9 \pm 1.3 \pm .94) \times 10^{-6}$
108. – 132.	$(29.0 \pm .40 \pm 1.1 \pm .78 \pm 1.1) \times 10^{-6}$
132. – 162.	$(16.4 \pm .27 \pm .63 \pm .44 \pm .80) \times 10^{-6}$
162. – 199.	$(9.39 \pm .18 \pm .36 \pm .25 \pm 1.0) \times 10^{-6}$

Table 3: Primary proton spectrum. Data collected during the three periods with different zenith pointing criteria are combined. Kinetic Energy is in GeV, flux in $(m^2 \cdot sr \cdot sec \cdot \ MeV)^{-1}$, ε_{stat} stands for the statistical error and $\varepsilon_{sys1,2,3}$ for the systematic errors.

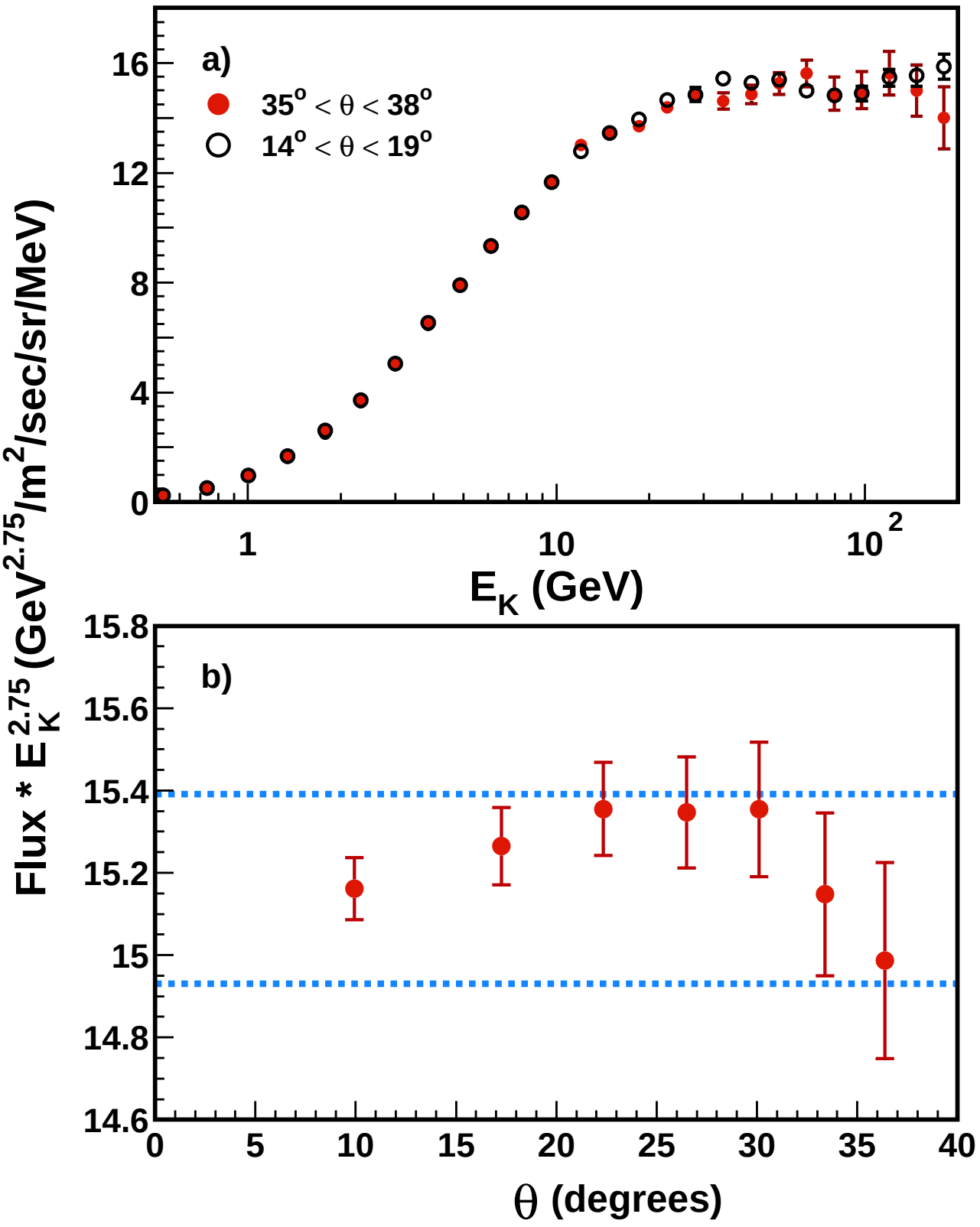

Figure 1: Isotropy: a) Comparison of the energy spectra for two angular acceptance ranges. b) Fluxes averaged above 20 GeV as a function of the incident particle angle. Error bars show statistical errors. The dashed lines in b) indicate the estimated range of systematic errors for this case. As seen, the data are independent of θ.

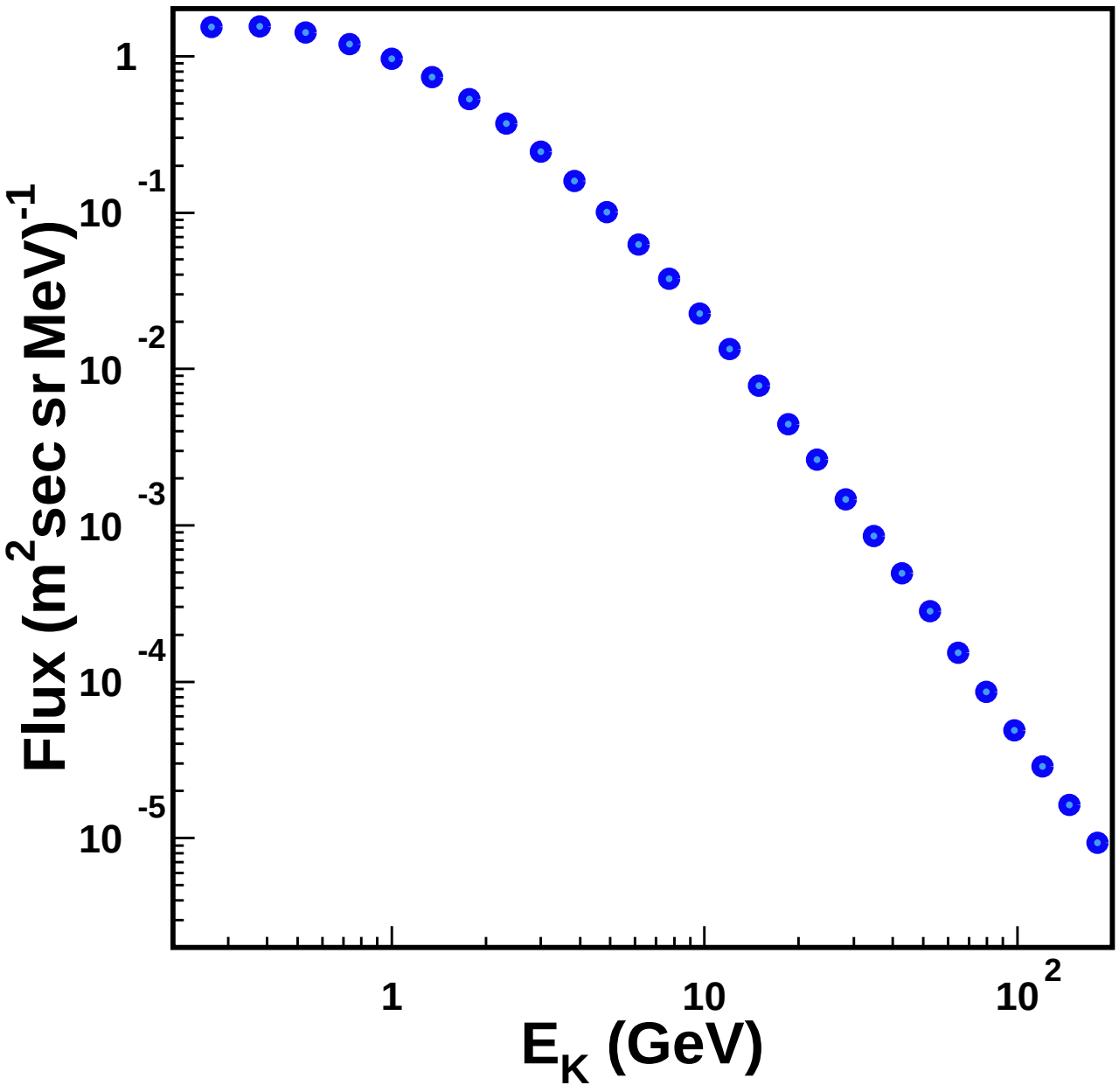

Figure 2: The primary proton flux. Fitting this spectrum to a power law in rigidity, $\Phi = \Phi_0 R^{-\gamma}$, over the range 10 GV< R < 200 GV yields $\gamma = 2.78 \pm 0.009$ (fit) $\pm$ 0.019 (sys) and $\Phi_0 = 17.1 \pm 0.15$ (fit) $\pm$ 1.3 (sys) $\pm$ 1.5 (γ) GV$^{2.78}$/(m^{2}sec sr MV), in good agreement with our previous result [4].

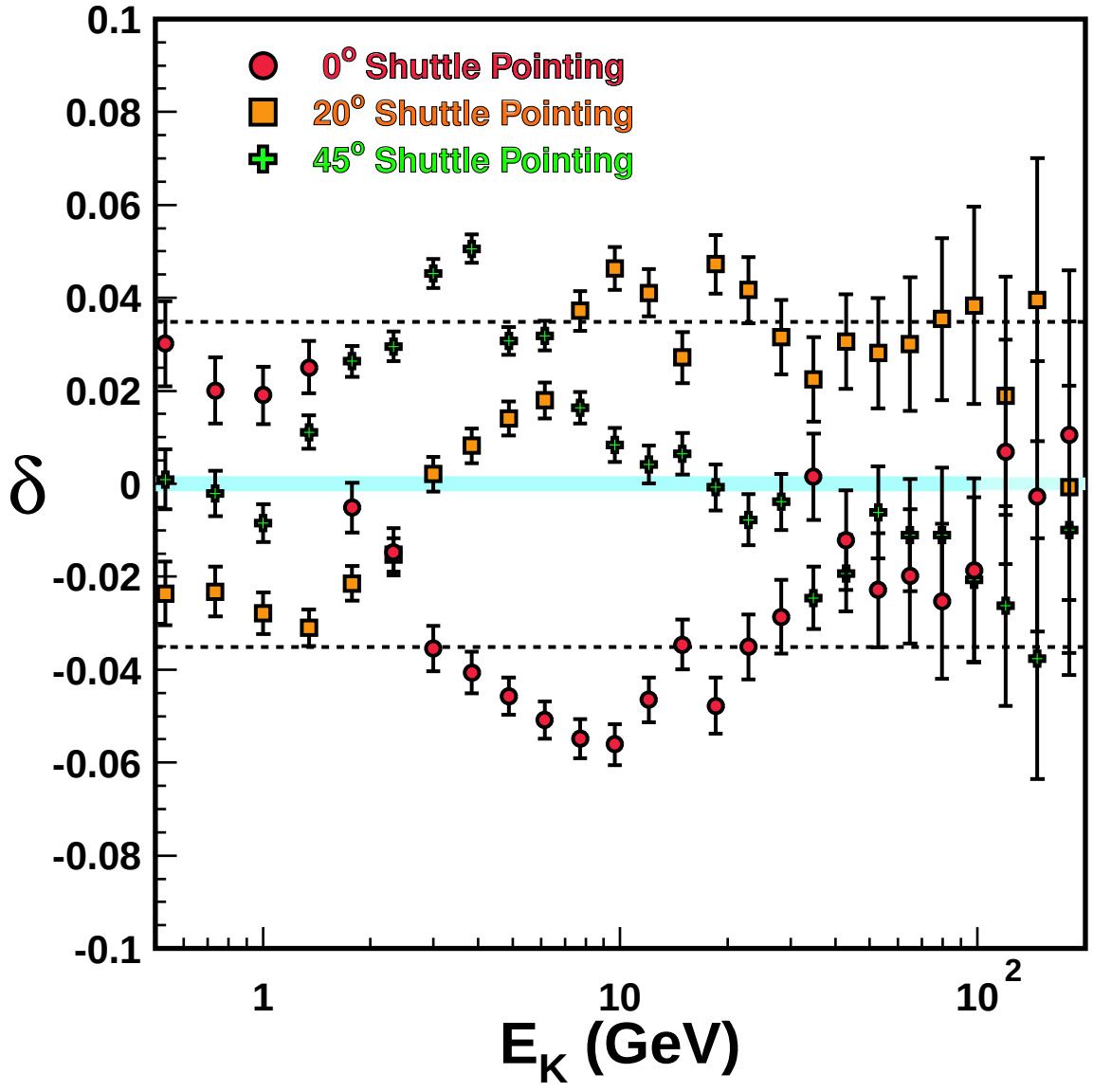

Figure 3: Systematic error verification: Flux variation, δ, as a function of proton energy for different shuttle orientations. Errors shown are statistical. The dashed lines show the range of systematic error calculated for this case.

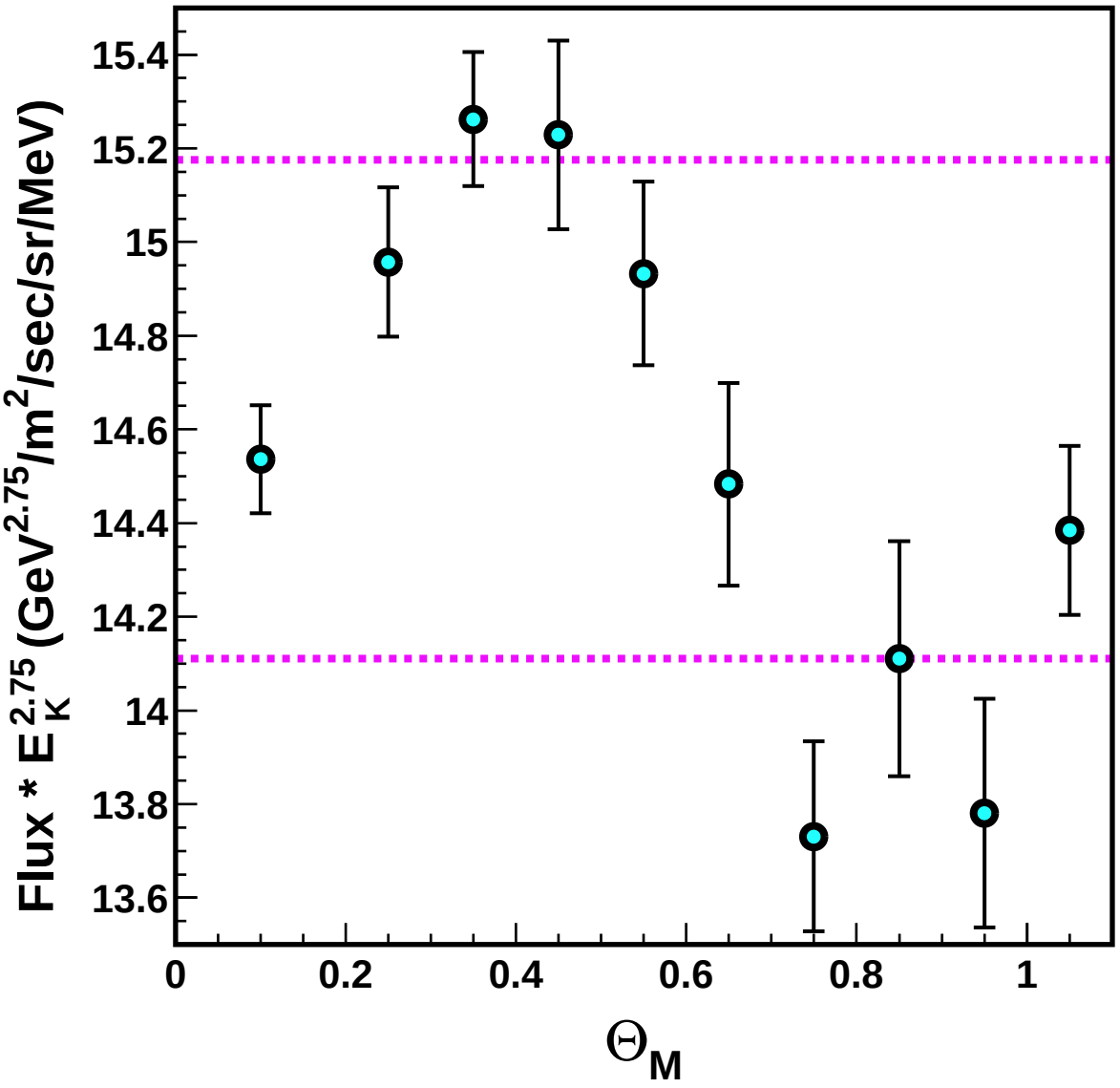

Figure 4: Systematic error verification: Fluxes averaged above 20 GeV scaled by $E_K^{2.75}$ as a function of magnetic latitude. Errors shown are statistical. The dashed lines show the range of the systematic error calculated for this case.

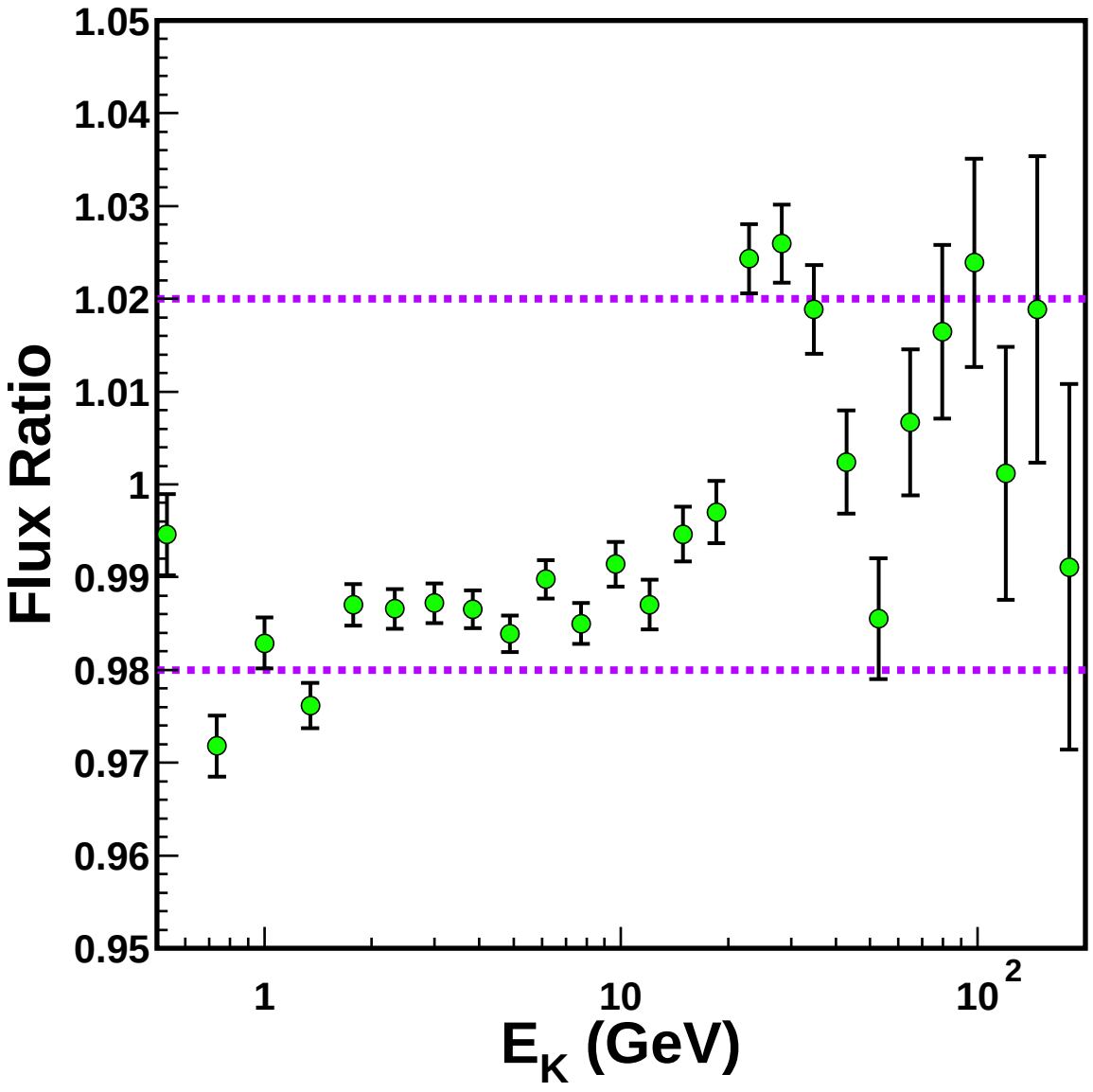

Figure 5: Verification of systematics: Ratio of the fluxes computed with and without proton selection quality cuts. The dashed lines show the range of the average systematic error calculated for this case.

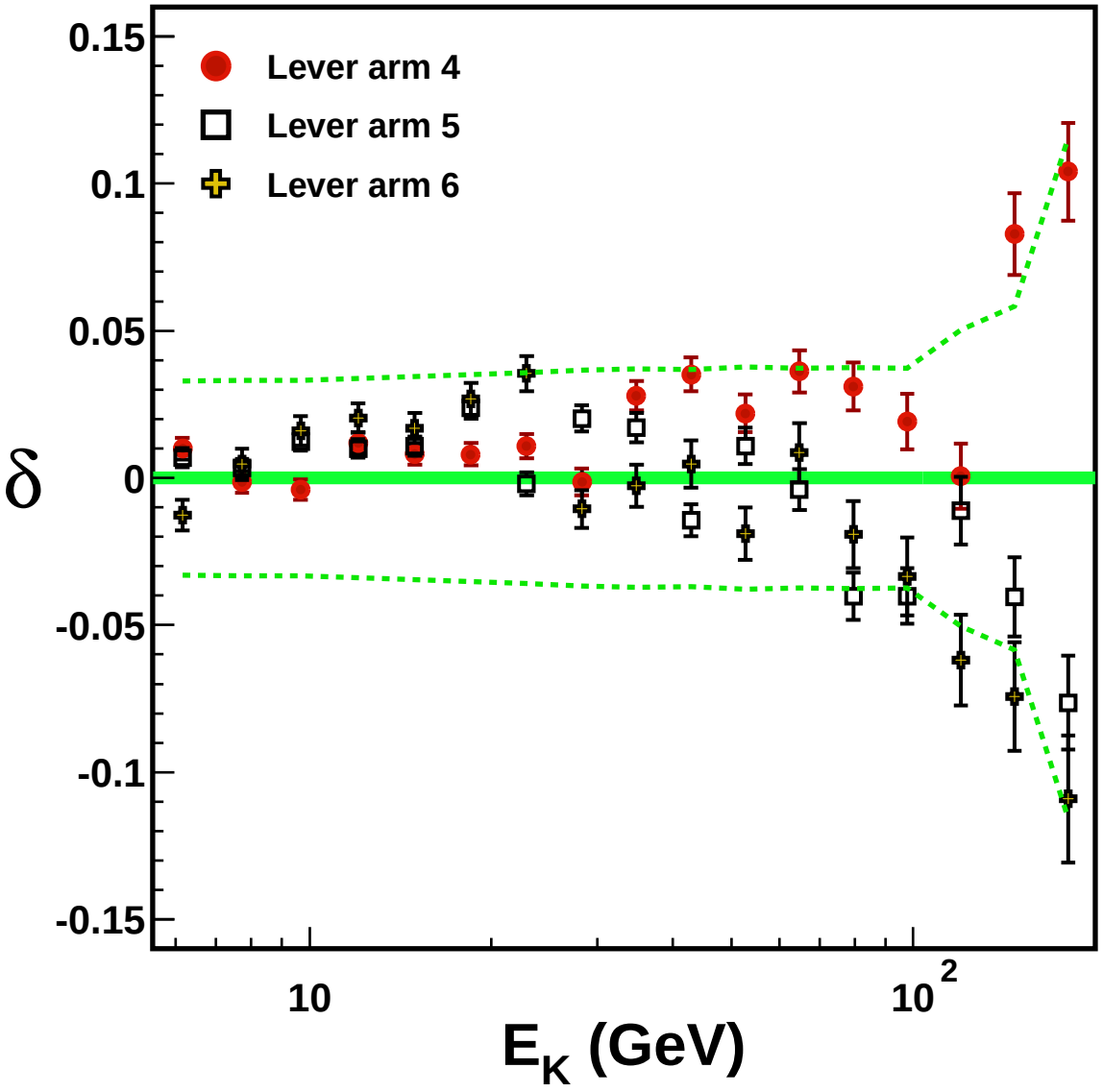

Figure 6: Verification of systematics: Flux variation, δ, for events with lever arms in the tracker which correspond to 4, 5 or 6 planes. The dashed lines show the range of the calculated systematic errors.

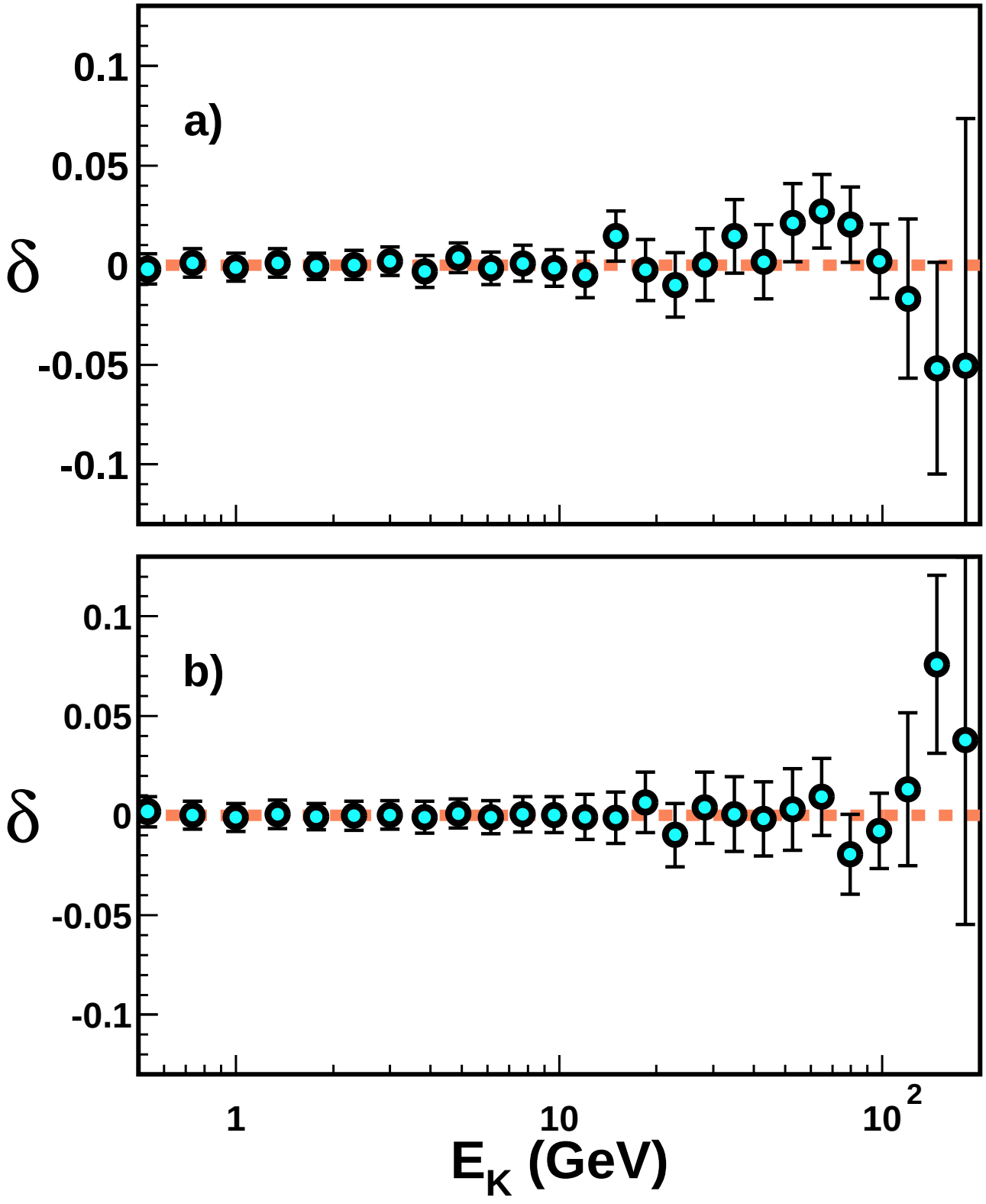

Figure 7: Verification of systematics: a) Variation of the flux, δ, computed with a resolution matrix including an artificial smearing of the alignment by an additional 10 μm. b) Variation of the flux, δ, calculated with two different unfolding methods.

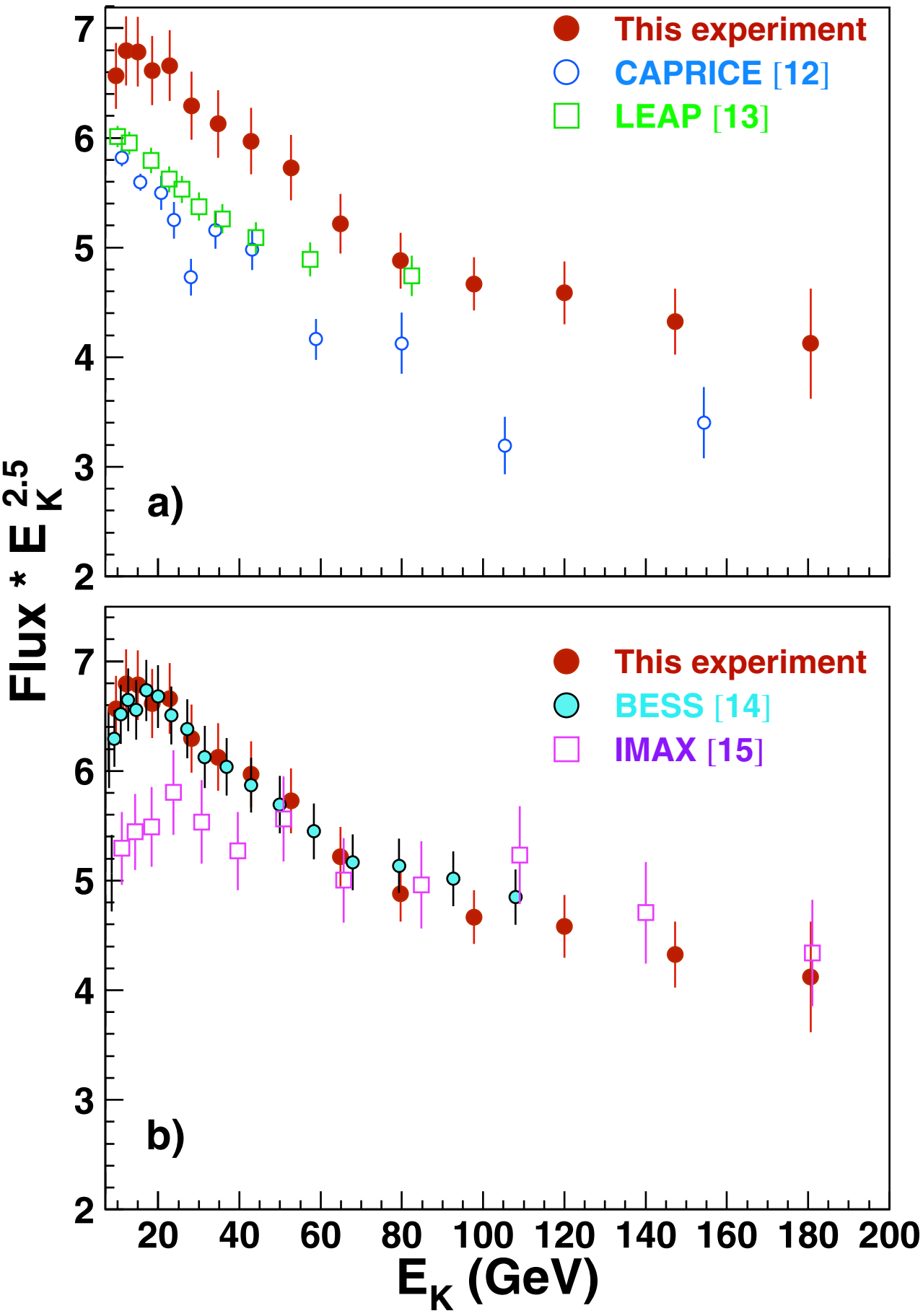

Figure 8: The primary proton spectrum multiplied by $E_K^{2.5}$ in units of $GeV^{2.5}/(m^2\,sec\,sr\,MeV)$ as measured by this experiment (total errors shown) in comparison with some recent balloon based measurements.

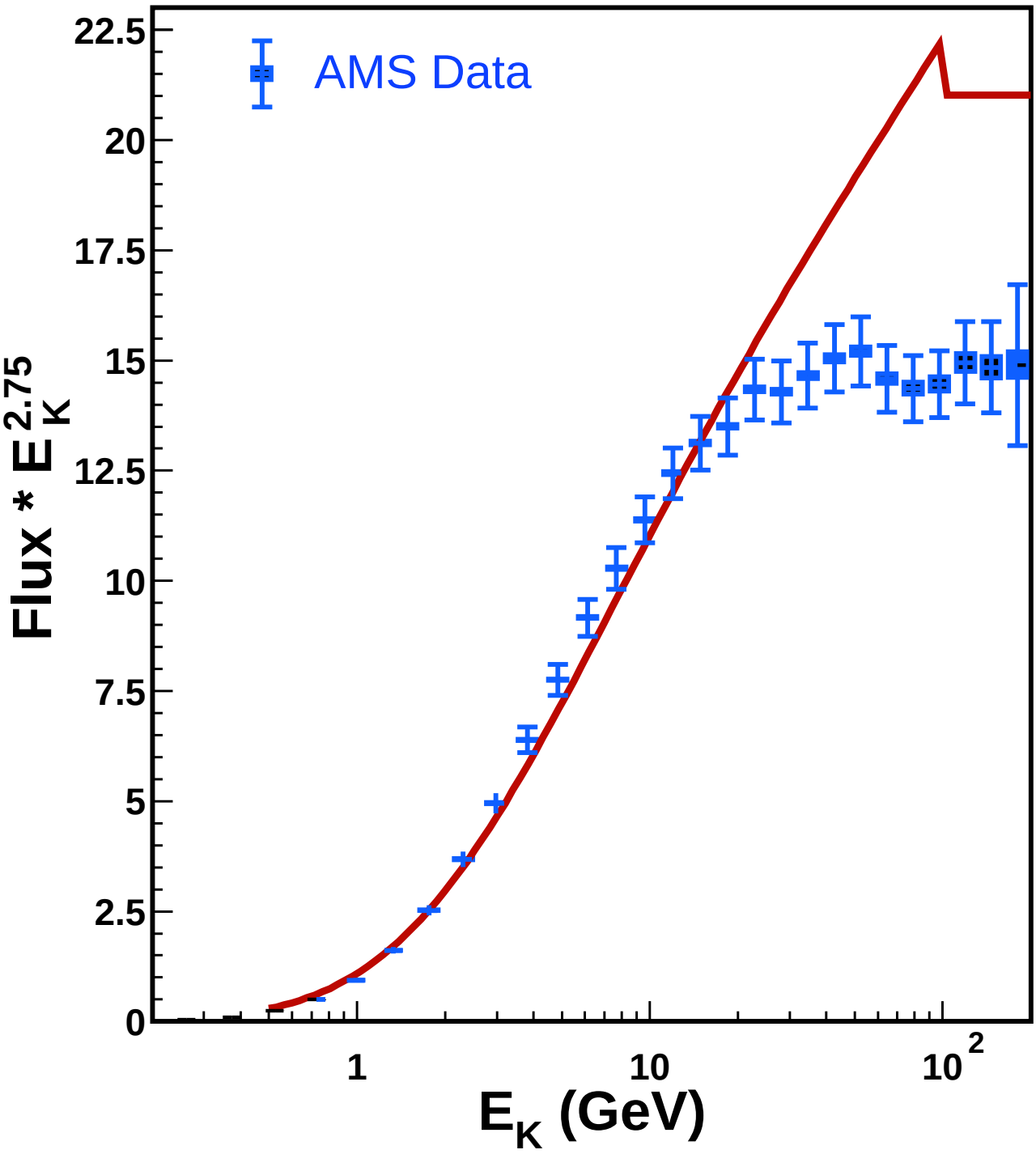

Figure 9: The primary proton flux multiplied by $E_K^{2.75}$ in units of $GeV^{2.75}/(m^2\,sec\,sr\,MeV)$. The solid rectangles indicate the statistical errors, the error bars indicate the total error. The solid line is the flux used to calculate atmospheric neutrinos [2] scaled by $E_K^{2.75}$.

AMS paper 04 "Cosmic Protons"
Published in Physics Letters B vol.490 (2000) p.27-35.
Referee report :

"This paper is very important and highly relevant. It should be published with only minor corrections and a few notes of verification:

1) I have heard from several scientists who work on the codes that are part of GEANT, that there are systematic errors, now corrected, that are especially acute for protons. This was especially worrisome for GEISHA, but not for FLUKA. One of the problem arose from the use of a multiplicity function for the creation of pions in a collison, that did not extrapolate well from nuclei to single protons. The corrections were made just a few years ago, and may not be relevant here. It would be good to include a footnote that makes it obvious, that these problems do not affect the data analysis done here.

2) p. 2 there is the expression "CERN proton-synchrotron"; I think the language would sound a bit better if one were to write "CERN proton-synchrotron machine" or something like that. Otherwise it is just lingo.
3) There is a typo in the footnote on p. 5 "dependence"

4) There is a probably trivial point: Looking at fig. 9, it appears that the spectrum used by Gaisser and others in present day neutrino calculations is too high, whereas the graph 8 shows that all the best data in recent years were at the same level or too low compared to AMS. That does not look consistent, but may be correct of course. This should be clarified in a brief sentence."

AMS paper 04 "Cosmic Protons"
Published in Physics Letters B vol.490 (2000) p.27-35.
Referee report :

"This paper is very important and highly relevant. It should be published with only minor corrections and a few notes of verification:

1) I have heard from several scientists who work on the codes that are part of GEANT, that there are systematic errors, now corrected, that are especially acute for protons. This was especially worrisome for GEISHA, but not for FLUKA. One of the problem arose from the use of a multiplicity function for the creation of pions in a collison, that did not extrapolate well from nuclei to single protons. The corrections were made just a few years ago, and may not be relevant here. It would be good to include a footnote that makes it obvious, that these problems do not affect the data analysis done here.

2) p. 2 there is the expression "CERN proton-synchrotron"; I think the language would sound a bit better if one were to write "CERN proton-synchrotron machine" or something like that. Otherwise it is just lingo.
3) There is a typo in the footnote on p. 5 "dependence"

4) There is a probably trivial point: Looking at fig. 9, it appears that the spectrum used by Gaisser and others in present day neutrino calculations is too high, whereas the graph 8 shows that all the best data in recent years were at the same level or too low compared to AMS. That does not look consistent, but may be correct of course. This should be clarified in a brief sentence."

Attachment V

Helium in Near Earth Orbit

The AMS Collaboration

Abstract

The helium spectrum from 0.1 to 100 GeV/nucleon was measured by the Alpha Magnetic Spectrometer (AMS) during space shuttle flight STS–91 at altitudes near 380 km. Above the geomagnetic cutoff the spectrum is parameterized by a power law. Below the geomagnetic cutoff a second helium spectrum was observed. In the second helium spectra over the energy range 0.1 to 1.2 GeV/nucleon the flux was measured to be $(6.3 \pm 0.9) \times 10^{-3} (\mathrm{m}^2\,\mathrm{sec}\,\mathrm{sr})^{-1}$ and more than ninety percent of the helium was determined to be ^{3}He (at the 90 % CL). Tracing helium from the second spectrum shows that about half of the ^{3}He travel for an extended period of time in the geomagnetic field and that they originate from restricted geographic regions similar to protons and positrons.

Published in Phys. Lett. B494 (30 Nov 2000) 193-202

Referee's report attached.

Introduction

Helium nuclei are the second most abundant element in cosmic rays. Helium rigidity spectrum measurements carried out over the past several decades (see [1] and references therein) have yielded insight into the origin of cosmic rays [2]. Since no difference in the rigidity spectra of protons and helium has been detected the same sources and propagation histories were inferred for both species [3]. However, recent and more accurate measurements [4, 5] suggest protons and helium may have different spectral indices in the range 10 to 100 GV. The most accurate experiments to date were balloon based [4,6–9], however in balloon experiments the ~ 5 g/cm^2 of residual atmosphere was an important source of systematic errors. Above ~ 1000 GV emulsion experiments [10, 11] have indicated a more pronounced difference. Geomagnetically trapped low energy light isotopes have been studied with satellites [12].

The Alpha Magnetic Spectrometer (AMS) [13] is a high energy physics experiment scheduled for installation on the International Space Station. In preparation for this mission, AMS flew a precursor mission in June 1998 on board the space shuttle Discovery during flight STS–91 at altitudes between 320 and 390 km. In this report the data collected during that flight are used to study the cosmic ray helium spectra in the kinetic energy range 0.1 to 100 GeV/nucleon.

The high statistics (~ 10^6) available allow measurement of the helium spectrum over a range of geomagnetic latitudes. With the incident particle direction and momentum accurately measured in AMS, the origin of particles below geomagnetic cutoff is studied by tracking them in the Earth's magnetic field.

The AMS experiment

The major elements of AMS as flown on STS–91 were a permanent magnet, a tracker, time of flight hodoscopes, a Cerenkov counter and anti-coincidence counters [14, 15]. The permanent magnet had the shape of a cylindrical shell with inner diameter 1.1 m and length 0.8 m. It provided a central dipole field of 0.14 Tesla across the magnet bore and an analyzing power, BL^2, of 0.14 Tm^2 parallel to the magnet, or z–, axis. The six layers of double sided silicon tracker were arrayed transverse to the magnet axis. The outer layers were just outside the magnet bore. The tracker measured the trajectory of relativistic unit charge particles with an accuracy of 10 microns in the bending coordinate and 30 microns in the non-bending coordinate, as well as providing multiple energy loss measurements. The time of flight system had two orthogonal planes at each end of the magnet, covering the outer tracker layers. Together the four planes measured doubly charged particle transit times with an accuracy of 105 psec and they also yielded multiple energy loss measurements. A layer of anti-coincidence scintillation counters lined the inner surface of the magnet. Low energy particles were absorbed by thin carbon fiber shields. In flight the AMS positive z–axis pointed out of the shuttle payload bay.

Data collection started on 3 June 1998. The orbital inclination was 51.7° and the geodetic altitude ranged from 320 to 390 km. For this study the data was collected in three periods:

(a) 25 hours before docking with the MIR space station, during which the shuttle attitude was constrained to keep the AMS z–axis pointing within 45° of the zenith.

(b) Four days while docked to MIR. The AMS z–axis pointing varied between 40° and 145° of the zenith.

(c) After MIR undocking. Within 1 degree, the pointing was kept within 0°, 20° and 45° of the

zenith for 19, 25 and 20 hours. Before descending, the shuttle was turned over for approximately 9 hours and the pointing was towards the nadir.

Data collected while passing through the South Atlantic Anomaly were excluded from the analysis and the acceptance was restricted to events with an incident angle within 32° of the positive z–axis of AMS.

The response of the detector was simulated using the AMS detector simulation program, which is based on the GEANT package [16]. The effects of energy loss, multiple scattering, interactions [17], decays and the measured detector efficiency and resolution were included.

Postflight, the AMS detector was extensively calibrated [15] with helium and carbon beams at GSI, Darmstadt and with proton beams at the CERN PS. The helium calibration analyzed 30 million events at four different kinetic energy points from E_K = 1.0 to 6.5 GeV/nucleon and at over six hundred incident angles and positions.

Analysis

The incident particle rigidity, R = $pc/|Z|e$, was fit using two independent algorithms from the deflection of the trajectory measured using hits in at least 4 planes of the tracker. The velocity of the particle, β = v/c, was determined using the information of the time of flight hits matching the reconstructed track. The mass of the particle was then determined from the measured velocity and momentum. To obtain $|Z|$, a reference set of energy loss distributions was obtained from the data samples and the energy measurements of the hits associated to the reconstructed particle were then fit to these reference distributions independently for the tracker layers and for the time of flight planes. For particles with $|Z| > 1$ the reconstruction was repeated requiring a higher threshold on the tracker hits. The particle type was then determined by combining the velocity, momentum and Z measurements.

A particle was selected as a helium candidate if the determination of the charge magnitude from the measurements of energy losses in the tracker planes was $|Z| = 2$ and the particle type was compatible with a $|Z| > 1$ particle.

The main potential source of background to the helium sample were protons wrongly reconstructed as $|Z| = 2$ particles. Using the independent measurement of the charge magnitude obtained from the time of flight counters, as detailed in our earlier publication [15], this background was estimated to be less than 10^{-4} over all energies.

Differential helium flux

The differential helium flux was determined by correcting the measured rates for the detector acceptance as a function of the particle momentum and direction. The acceptance was determined via the Monte Carlo method using simulated helium samples which were required to pass through a trigger simulation and the same reconstruction and selection chain as for data. The average acceptance was determined to be 0.10 m^2 sr for rigidities above 20 GV, increasing at lower rigidities to 0.16 m^2 sr.

Corrections to the acceptance were studied with a sample of events collected with an unbiased trigger and by comparing data and Monte Carlo samples. The average contributions to the uncertainty in these corrections were 4 % from the trigger, 3 % from the track reconstruction, and 2 % each from the modeling of particle interactions and from the selection; leading to an overall systematic error of 6% in the acceptance. The incident differential helium flux was obtained from an unfolding of the measured spectrum based on Bayes' theorem [18].

For the differential flux analysis, only the data sample from period (c) was considered. The differential spectra for three ranges of the corrected geomagnetic latitude [19], $|\Theta_M|$, are presented in Fig. 1 for the 0° attitude subsample.

The figure shows the effect of the geomagnetic cutoff which decreases with increasing $|\Theta_M|$. In addition to the above cutoff, or primary, spectrum, Fig. 1 also shows the presence of a second spectrum below cutoff for $|\Theta_M| < 0.8$, which is discussed in detail below.

This cutoff effect varies weakly for the different attitudes (0°, 20°, 45°) due to the anisotropy of the flux at these rigidity ranges. Above cutoff the flux spectra are identical. The differential primary helium spectrum versus rigidity using the combined above cutoff data from the three attitudes is presented in table 1 and in Fig. 2 scaled by $R^{2.74}$. For comparision, Fig. 2 also shows the helium flux used in atmospheric neutrino calculations [20].

R	Flux
.76 – .91	(32 ± 16)
.91 – 1.10	48.9 ± 2.9
1.10 – 1.32	58.4 ± 3.2
1.32 – 1.58	62.8 ± 3.4
1.58 – 1.91	63.9 ± 3.5
1.91 – 2.29	58.2 ± 3.2
2.29 – 2.75	49.4 ± 2.7
2.75 – 3.31	39.6 ± 2.1
3.31 – 3.98	30.8 ± 1.7
3.98 – 4.79	22.6 ± 1.2

R	Flux
4.79 – 5.75	$(159. \pm 8.6) \times 10^{-1}$
5.75 – 6.92	$(110. \pm 5.9) \times 10^{-1}$
6.92 – 8.32	$(72.8 \pm 3.9) \times 10^{-1}$
8.32 – 10.00	$(47.1 \pm 2.5) \times 10^{-1}$
10.00 – 12.02	$(29.9 \pm 1.6) \times 10^{-1}$
12.02 – 14.45	$(18.9 \pm 1.0) \times 10^{-1}$
14.45 – 17.38	$(119. \pm 6.4) \times 10^{-2}$
17.38 – 20.89	$(73.7 \pm 4.0) \times 10^{-2}$
20.89 – 25.12	$(47.0 \pm 2.6) \times 10^{-2}$
25.12 – 30.20	$(28.9 \pm 1.6) \times 10^{-2}$

R	Flux
30.20 – 36.31	$(172. \pm 9.4) \times 10^{-3}$
36.31 – 43.65	$(101. \pm 5.6) \times 10^{-3}$
43.65 – 52.48	$(63.2 \pm 3.5) \times 10^{-3}$
52.48 – 63.10	$(38.0 \pm 2.1) \times 10^{-3}$
63.10 – 75.86	$(22.2 \pm 1.2) \times 10^{-3}$
75.86 – 91.20	$(137. \pm 8.0) \times 10^{-4}$
91.20 – 109.65	$(82.9 \pm 5.0) \times 10^{-4}$
109.65 – 131.83	$(49.1 \pm 3.3) \times 10^{-4}$
131.83 – 158.49	$(27.8 \pm 1.9) \times 10^{-4}$
158.49 – 190.55	$(16.5 \pm 1.4) \times 10^{-4}$
190.55 – 229.09	$(118. \pm 8.0) \times 10^{-5}$

Table 1: Differential primary helium flux in units of $(m^2\,sec\,sr\,GV)^{-1}$ versus rigidity, R, in GV. The errors quoted are the combination in quadrature of the statistical and systematic errors.

Analysis of the primary spectrum

The primary cosmic ray spectrum may be parametrized by a power law in rigidity as $\Phi_0 \times R^{-\gamma}$. The spectrum has been fit [21] over the rigidity range $20 < R < 200$ GV. To avoid cutoff effects, data collected in regions where the expected cutoff in the direction of the AMS z–axis was larger than 12 GV were excluded from the fit. The results obtained on the three different attitude samples were the same within the errors. The combined fit yields:

$$\gamma = 2.740 \pm 0.010\,(\text{stat}) \pm 0.016\,(\text{sys}),$$

$$\Phi_0 = 2.52 \pm 0.09\,(\text{stat}) \pm 0.13\,(\text{sys}) \pm 0.14\,(\gamma)\ \frac{\text{GV}^{2.74}}{\text{m}^2\,\text{sec}\,\text{sr}\,\text{MV}}\,.$$

The systematic uncertainty in γ was estimated from the uncertainty in the track resolution (0.014) and the variation of the selection criteria (0.009). The third uncertainty quoted for Φ_0 reflects the systematic uncertainty in γ. This fit is shown with the data in Fig. 2. In Fig. 3 the primary spectrum is compared to the recent balloon measurements [5, 7–9] [1)].

[1)] A ^{3}He fraction of 0.15±0.05 was assumed.

Analysis of the second spectrum

As shown in Fig. 1 a second spectrum is observed for $|\Theta_M| < 0.8$. This spectrum extends from the lowest measured rigidity, 0.8 GV, up to 3 GV with an integrated flux of $\sim 10^{-3}(\,\mathrm{m}^2\,\mathrm{sec\,sr})^{-1}$.

To ensure these events are not due to resolution effects at low energies or to contamination from single scattering inside the detector, more stringent reconstruction criteria were applied in the examination of the second spectrum. Those $|Z| = 1$ events with a wrongly reconstructed charge magnitude were reduced by an additional factor of 100 by requiring the combined time of flight and tracker charge magnitude determinations to be $|Z| = 2$. Tails in the velocity reconstruction were reduced by requiring at least three matched hits in the four time of flight planes. In this energy range, the accuracy of the velocity measurement is 2.4%. Any large angle scattering in a tracker plane was identified and removed by requiring that the particle was also measured by the tracker in the non-bending projection and by requiring agreement between the rigidity measured with the first three hits along the track, with the last three hits and with all the hits. Events with collinear delta rays, which create additional energy depositions in the tracker planes along the trajectory of the particle, were identified and rejected by an isolation criteria on the amount of energy observed within 10 mm of the track. Finally, extrapolation of the fit track was required to match the location of the used time of flight counter hits within 60 mm.

These criteria were applied to the data samples from periods (a), (b) and (c). Compared to the looser cuts used in the analysis of the differential rigidity spectrum, the selection efficiency is ~ 65 % up to 3 GV. The average mass resolution for helium nuclei in the kinetic energy range 0.1 to 1.2 GeV/nucleon (*i.e.* $\beta < 0.9$) is ~ 12 %. Fig. 4 shows the reconstructed mass distribution for events above cutoff at $|\Theta_M| > 0.9$ in this energy range. As shown, the data are in agreement with a Monte Carlo simulation which contains 11.5 % ^{3}He.

Fig. 5 shows the correlation between rigidity, R, and velocity, β, for events with $|\Theta_M| < 0.6$, together with the expectations for ^{3}He and ^{4}He nuclei. Primary spectrum events are clustered at $\beta > 0.9$ with rigidities in the range of 3 to 200 GV. A population of 115 events with rigidities below the local geomagnetic cutoff are marked in the figure with open circles. As seen, this population follows the ^{3}He mass line. Fig. 6 shows a scatter plot of rigidity versus Θ_M for events with $\beta < 0.9$. The two symmetric clusters at $|\Theta_M| > 0.6$ correspond to nuclei from the primary helium spectrum. The same 115 events marked in Fig. 5 form a clear and isolated low energy band (R < 3 GV). This second population has the following properties:

- The reconstructed mass distribution given in Fig. 7 shows that most of the events are consistent with ^{3}He. At the 90 % confidence level, the fraction of ^{3}He exceeds ninety percent.
- As shown in Fig. 8, their spectrum extends from the lowest measured kinetic energy, E_K = 0.1 GeV/nucleon, to ~ 1.2 GeV/nucleon, yielding an average flux of $(6.3 \pm 0.9) \times 10^{-3}(\mathrm{m}^2\,\mathrm{sec\,sr})^{-1}$.
- As shown in Fig. 9, the flux tends to a maximum at the geomagnetic equator.
- Within the statistics, there is no preferred direction and the fluxes measured separately with data from the three periods (a), (b) and (c) are equal.

To understand the origin of these events, the trajectories have been traced both backward and forward from their incident angle, location and momentum, through the Earth's magnetic field, following the same procedure as described in [21, 22]. All events were found to originate in the atmosphere. Analysis of the sum of their forward and backward flight times yields two distinct classes: "short–lived" and "long–lived" for flight times below and above 0.3 sec respectively.

As shown in Fig. 10 the origins of the “short-lived” helium nuclei are distributed uniformly around the globe whereas the “long-lived” particles originate from two geographically restricted regions. These regions match those from which the second proton flux and second positron flux originate [21, 22]. Within the statistics, ^{3}He is equally predominate in events from both the “short–lived” and “long–lived” classes.

Conclusions

The helium spectrum between 0.1 and 100 GeV/nucleon was measured in near Earth orbit. The primary helium rigidity spectrum has been fit to a power law with a spectral index $\gamma = 2.740 \pm 0.010\,(\text{stat}) \pm 0.016\,(\text{sys})$. Below the geomagnetic cutoff a second spectrum of helium was observed with a flux of $(6.3 \pm 0.9) \times 10^{-3}(\text{m}^2\,\text{sec}\,\text{sr})^{-1}$. Over ninety percent of this second flux is ^{3}He (at the 90 % CL). This second flux has been traced to originate from the same locations as the corresponding second proton and positron fluxes, with the long lived component originating from two restricted geographic regions.

Acknowledgements

The support of INFN, Italy, ETH–Zürich, the University of Geneva, the Chinese Academy of Sciences, Academia Sinica and National Central University, Taiwan, the RWTH–Aachen, Germany, the University of Turku, the University of Technology of Helsinki, Finland, the U.S. DOE and M.I.T., CIEMAT, Spain, LIP, Portugal and IN2P3, France, is gratefully acknowledged.

The success of the first AMS mission is due to many individuals and organisations outside of the collaboration. The support of NASA was vital in the inception, development and operation of the experiment. Support from the Max–Planck Institute for Extraterrestrial Physics, from the space agencies of Germany (DLR), Italy (ASI), France (CNES) and China and from CSIST, Taiwan also played important roles in the success of AMS.

References

[1] B. Wiebel-Sooth, P. L. Biermann and H. Meyer, Astr. and Astrophys **330** (1998) 389.

[2] P. L. Biermann *et al.*, Phys. Rev. **D51** (1995) 3450.

[3] W. R. Webber and J. A. Lezniak, Astrophys. Space Sci. **30** (1974) 361.

[4] E. S. Seo *et al.*, ApJ **378** (1991) 763.

[5] J. Buckley *et al.*, ApJ **429** (1994) 736–747.

[6] P. Papini *et al.*, Proc. 23rd ICRC Calgary **1** (1993) 579.

[7] M. Boezio *et al.*, ApJ **518** (1999) 457.

[8] T. Sanuki *et al.*, astro-ph/0002481 (2000).

[9] W. Menn *et al.*, ApJ **533** (2000) 281.

[10] K. Asakimori *et al.*, Proc. 23rd ICRC Calgary **2** (1993) 25.

[11] K. Asakimori *et al.*, ApJ **502** (1998) 278.

[12] J. P. Wefel *et al.*, Proc. 24th ICRC **4** (1995) 1021; J. Chen *et al.*, Geophys. Res. Lett. **21** (1994) 1583; M. D. Looper *et al.*, Radiation Measurements **26** (1996) 967; R. S. Selesnick and R. A. Mewaldt, JGR **101** (1996) 19745–19757.

[13] S. Ahlen *et al.*, Nucl. Inst. Meth. **A350** (1994) 351.

[14] G. M. Viertel and M. Capell, Nucl. Inst. Meth. **A419** (1998) 295–299.

[15] AMS Collaboration, J. Alcaraz *et al.*, Phys. Lett. **B461** (1999) 387–396.

[16] R. Brun *et al.*, GEANT 3, CERN DD/EE/84-1 (Revised, 1987); P. A. Aamio *et al.*, FLUKA Users Guide, CERN TIS-RP-190 (1990).

[17] R. J. Glauber, in: Lectures in Theoretical Physics, eds. W. E. Brittin *et al.***1** (N.Y. 1959) 315; S. Forte, Nucl. Phys. **A467** (1987) 665; S. Yu. Shmakov *et al.*, Comp. Phys. Comm. **54** (1988) 125; A. S. Pak *et al.*, Sov. J. Nucl. Phys. **30(2)** (1979) 178; I. V. Andreev and A. V. Chernov, Sov. J. Nucl. Phys. **28(2)** (1978) 243; Z. Omboo *et al.*, (1990), JINR-E. 90-21; G. Faldt and I. Hulthage, Nucl. Phys. **A316** (1979) 251; L. S. Azhgirei *et al.*, Sov. J. Nucl. Phys. **30(6)** (1979) 818; J. P. Burg *et al.*, Nucl. Phys. **B187** (1981) 205; A. Bujak *et al.*, Phys. Rev. **D23** (1981) 1895; V. Franco, Phys. Rev. **C6** (1972) 748; G. D. Alkhazov *et al.*, Nucl. Phys. **A280** (1977) 365; W. Bell *et al.*, Phys. Lett. **B117** (1982) 131; J. Jaros *et al.*, Phys. Rev. **C18** (1978) 2273; V. G. Ableev *et al.*, Z. Phys. **A340** (1991) 340; V. G. Ableev *et al.*, Acta physica Polonica **B16** (1985) 913; L. Satta *et al.*, Phys. Lett. **B139** (1984) 263.

[18] G. D'Agostini, Nucl. Inst. Meth. **A362** (1995) 487.

[19] A. Brekke, Physics of the Upper Polar Atmosphere, pp. 127–145, (Wiley, 1997).

[20] Formula 2.1 at solar minimum from M. Honda *et al.*, Phys. Rev. **D52** (1995) 4985, we have recently been informed that their current analysis is in closer agreement with our data. We thank M. Honda for this communication.

[21] AMS Collaboration, J. Alcaraz *et al.*, Phys. Lett. **B472** (2000) 215–226.

[22] AMS Collaboration, J. Alcaraz *et al.*, Phys. Lett. **B484** (2000) 10–22.

The AMS Collaboration

J.Alcaraz[y], B.Alpat[ac], G.Ambrosi[r], H.Anderhub[ag], L.Ao[g], A.Arefiev[ab], P.Azzarello[r], E.Babucci[ac], L.Baldini[j,l], M.Basile[j], D.Barancourt[s], F.Barao[w,v], G.Barbier[s], G.Barreira[w], R.Battiston[ac], R.Becker[l], U.Becker[l], L.Bellagamba[j], P.Béné[r], J.Berdugo[y], P.Berges[l], B.Bertucci[ac], A.Biland[ag], S.Bizzaglia[ac], S.Blasko[ac], G.Boella[z], M.Boschini[z], M.Bourquin[r], L.Brocco[j], G.Bruni[j], M.Buenerd[s], J.D.Burger[l], W.J.Burger[ac], X.D.Cai[l], C.Camps[b], P.Cannarsa[ag], M.Capell[l], D.Casadei[j], J.Casaus[y], G.Castellini[p,j], C.Cecchi[ac], Y.H.Chang[m], H.F.Chen[t], H.S.Chen[i], Z.G.Chen[g], N.A.Chernoplekov[aa], T.H.Chiueh[m], Y.L.Chuang[ad], F.Cindolo[j], V.Commichau[b], A.Contin[j], M.Cristinziani[r], J.P.da Cunha[n], T.S.Dai[l], J.D.Deus[v], N.Dinu[ac,1], L.Djambazov[ag], I.D'Antone[j], Z.R.Dong[h], P.Emonet[r], J.Engelberg[u], F.J.Eppling[l], T.Eronen[af], G.Esposito[ac], P.Extermann[r], J.Favier[c], E.Fiandrini[ac], P.H.Fisher[l], G.Fluegge[b], N.Fouque[c], Yu.Galaktionov[ab,l], M.Gervasi[z], P.Giusti[j], D.Grandi[z], O.Grimm[ag], W.Q.Gu[h], K.Hangarter[b], A.Hasan[ag], V.Hermel[c], H.Hofer[ag], M.A.Huang[ad], W.Hungerford[ag], M.Ionica[ac,1], R.Ionica[ac,1], M.Jongmanns[ag], K.Karlamaa[u], W.Karpinski[a], G.Kenney[ag], J.Kenny[ac], W.Kim[ae], A.Klimentov[l,ab], R.Kossakowski[c], V.Koutsenko[l,ab], M.Kraeber[ag], G.Laborie[s], T.Laitinen[af], G.Lamanna[ac], G.Laurenti[j], A.Lebedev[l], S.C.Lee[ad], G.Levi[j], P.Levtchenko[ac,2], C.L.Liu[x], H.T.Liu[i], I.Lopes[n], G.Lu[g], Y.S.Lu[i], K.Lübelsmeyer[a], D.Luckey[l], W.Lustermann[ag], C.Maña[y], A.Margotti[j], F.Mayet[s], R.R.McNeil[e], B.Meillon[s], M.Menichelli[ac], A.Mihul[k], A.Mourao[v], A.Mujunen[u], F.Palmonari[j], A.Papi[ac], I.H.Park[ae], M.Pauluzzi[ac], F.Pauss[ag], E.Perrin[r], A.Pesci[j], A.Pevsner[d], M.Pimenta[w,v], V.Plyaskin[ab], V.Pojidaev[ab], M.Pohl[r], V.Postolache[ac,1], N.Produit[r], P.G.Rancoita[z], D.Rapin[r], F.Raupach[a], D.Ren[ag], Z.Ren[ad], M.Ribordy[r], J.P.Richeux[r], E.Riihonen[af], J.Ritakari[u], U.Roeser[ag], C.Roissin[s], R.Sagdeev[o], G.Sartorelli[j], A.Schultz von Dratzig[a], G.Schwering[a], G.Scolieri[ac], E.S.Seo[o], V.Shoutko[l], E.Shoumilov[ab], R.Siedling[a], D.Son[ae], T.Song[h], M.Steuer[l], G.S.Sun[h], H.Suter[ag], X.W.Tang[i], Samuel C.C.Ting[l], S.M.Ting[l], M.Tornikoski[u], J.Torsti[af], J.Trümper[q], J.Ulbricht[ag], S.Urpo[u], I.Usoskin[z], E.Valtonen[af], J.Vandenhirtz[a], F.Velcea[ac,1], E.Velikhov[aa], B.Verlaat[ag,3], I.Vetlitsky[ab], F.Vezzu[s], J.P.Vialle[c], G.Viertel[ag], D.Vité[r], H.Von Gunten[ag], S.Waldmeier Wicki[ag], W.Wallraff[a], B.C.Wang[x], J.Z.Wang[g], Y.H.Wang[ad], K.Wiik[u], C.Williams[j], S.X.Wu[l,m], P.C.Xia[h], J.L.Yan[g], L.G.Yan[h], C.G.Yang[i], M.Yang[i], S.W.Ye[t,4], P.Yeh[ad], Z.Z.Xu[t], H.Y.Zhang[f], Z.P.Zhang[t], D.X.Zhao[h], G.Y.Zhu[i], W.Z.Zhu[g], H.L.Zhuang[i], A.Zichichi[j], B.Zimmermann[ag], P.Zuccon[ac]

---

[a] I. Physikalisches Institut, RWTH, D-52056 Aachen, Germany[5]

[b] III. Physikalisches Institut, RWTH, D-52056 Aachen, Germany[5]

[c] Laboratoire d'Annecy-le-Vieux de Physique des Particules, LAPP, F-74941 Annecy-le-Vieux CEDEX, France

[e] Louisiana State University, Baton Rouge, LA 70803, USA

[d] Johns Hopkins University, Baltimore, MD 21218, USA

[f] Center of Space Science and Application, Chinese Academy of Sciences, 100080 Beijing, China

[g] Chinese Academy of Launching Vehicle Technology, CALT, 100076 Beijing, China

[h] Institute of Electrical Engineering, IEE, Chinese Academy of Sciences, 100080 Beijing, China

[i] Institute of High Energy Physics, IHEP, Chinese Academy of Sciences, 100039 Beijing, China[6]

[j] University of Bologna and INFN-Sezione di Bologna, I-40126 Bologna, Italy[7]

[k] Institute of Microtechnology, Politechnica University of Bucharest and University of Bucharest, R-76900 Bucharest, Romania

[l] Massachusetts Institute of Technology, Cambridge, MA 02139, USA

[m] National Central University, Chung-Li, Taiwan 32054

[n] Laboratorio de Instrumentacao e Fisica Experimental de Particulas, LIP, P-3000 Coimbra, Portugal

[o] University of Maryland, College Park, MD 20742, USA

[p] CNR–IROE, I-50125 Florence, Italy

[q] Max–Planck Institut für extraterrestrische Physik, D-85740 Garching, Germany

[r] University of Geneva, CH-1211 Geneva 4, Switzerland
[s] Institut des Sciences Nucleaires, F-38026 Grenoble, France
[t] Chinese University of Science and Technology, USTC, Hefei, Anhui 230 029, China[6]
[u] Helsinki University of Technology, FIN-02540 Kylmala, Finland
[v] Instituto Superior Técnico, IST, P-1096 Lisboa, Portugal
[w] Laboratorio de Instrumentacao e Fisica Experimental de Particulas, LIP, P-1000 Lisboa, Portugal
[x] Chung–Shan Institute of Science and Technology, Lung-Tan, Tao Yuan 325, Taiwan
[y] Centro de Investigaciones Energéticas, Medioambientales y Tecnologícas, CIEMAT, E-28040 Madrid, Spain[8]
[z] INFN-Sezione di Milano, I-20133 Milan, Italy[7]
[aa] Kurchatov Institute, Moscow, 123182 Russia
[ab] Institute of Theoretical and Experimental Physics, ITEP, Moscow, 117259 Russia
[ac] INFN-Sezione di Perugia and Universitá Degli Studi di Perugia, I-06100 Perugia, Italy[7]
[ad] Academia Sinica, Taipei 11529, Taiwan
[ae] Kyungpook National University, 702-701 Taegu, Korea
[af] University of Turku, FIN-20014 Turku, Finland
[ag] Eidgenössische Technische Hochschule, ETH Zürich, CH-8093 Zürich, Switzerland
[1] Permanent address: HEPPG, Univ. of Bucharest, Romania.
[2] Permanent address: Nuclear Physics Institute, St. Petersburg, Russia.
[3] Now at National Institute for High Energy Physics, NIKHEF, NL-1009 DB Amsterdam, The Netherlands.
[4] Supported by ETH Zürich.
[5] Supported by the Deutsches Zentrum für Luft– und Raumfahrt, DLR.
[6] Supported by the National Natural Science Foundation of China.
[7] Also supported by the Italian Space Agency.
[8] Also supported by the Comisión Interministerial de Ciencia y Tecnología.

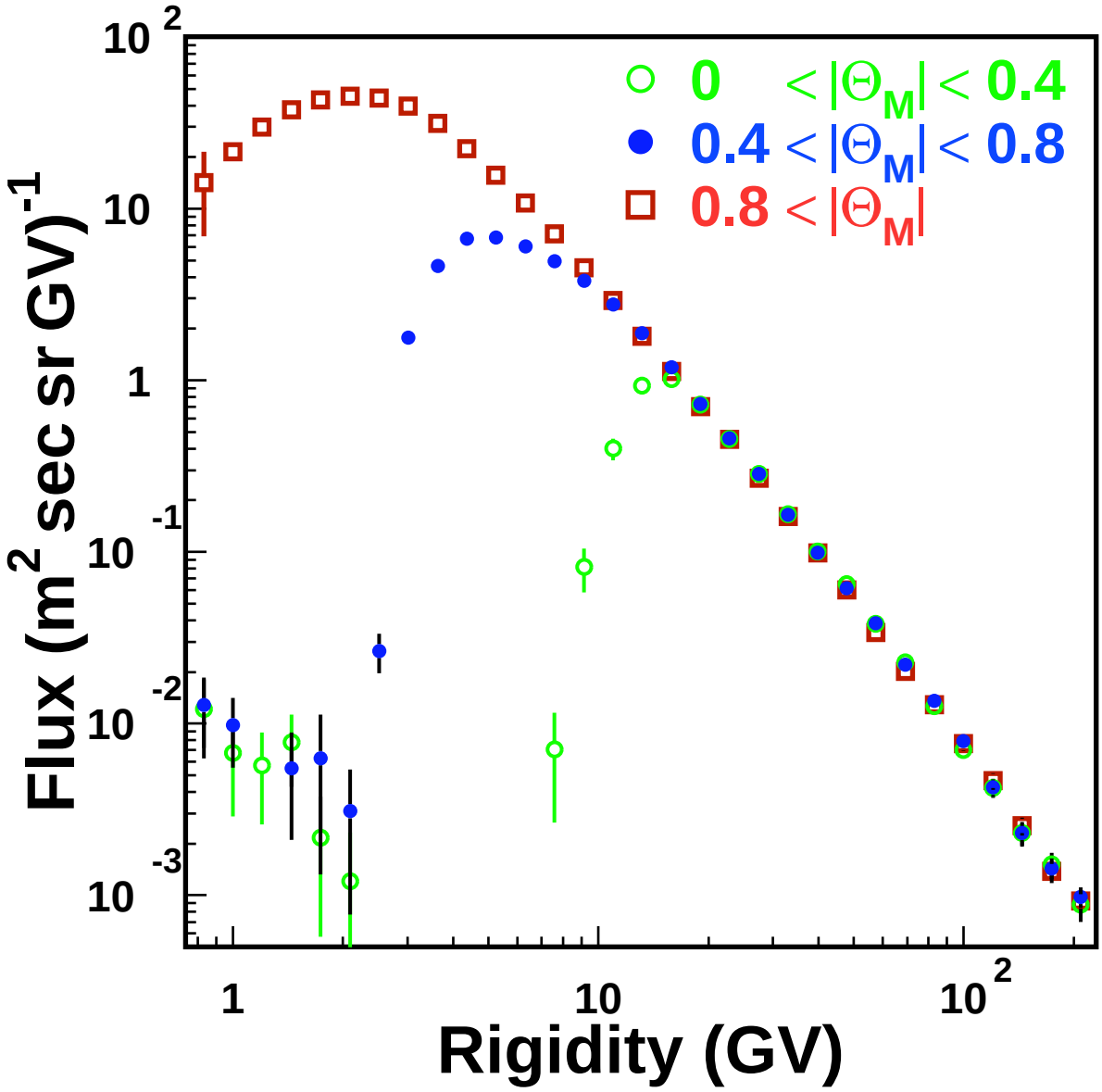

Figure 1: Helium flux spectra for the zenith pointing separated according to the geomagnetic latitude, $|\Theta_M|$, at which they were detected.

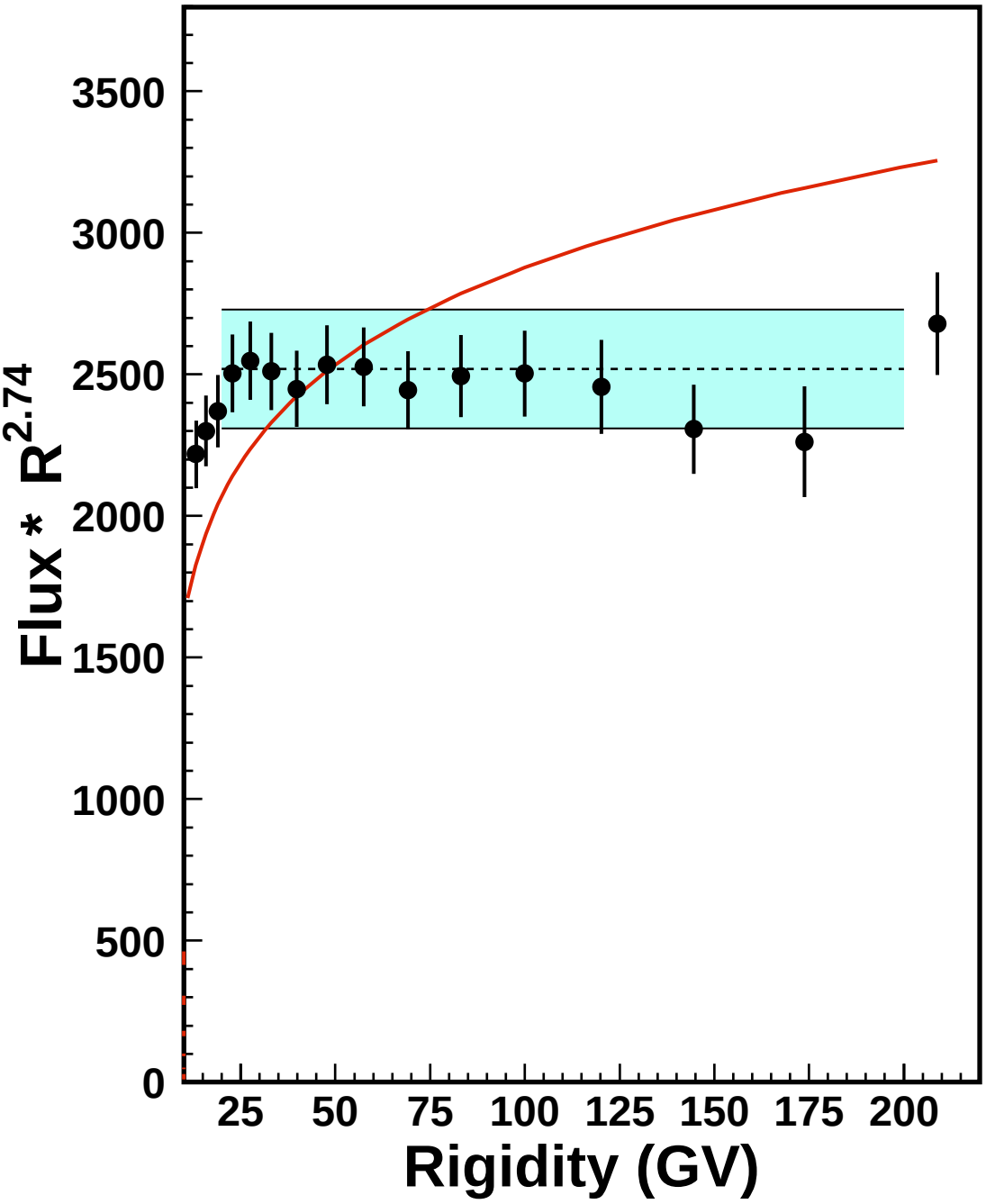

Figure 2: Primary helium flux spectrum multiplied by $R^{2.74}$ in units of $m^{-2}\,sec^{-1}\,sr^{-1}\,GV^{1.74}$. The band covers the range of the fit. The smooth line shows the spectrum used for atmospheric neutrino spectrum calculations [20].

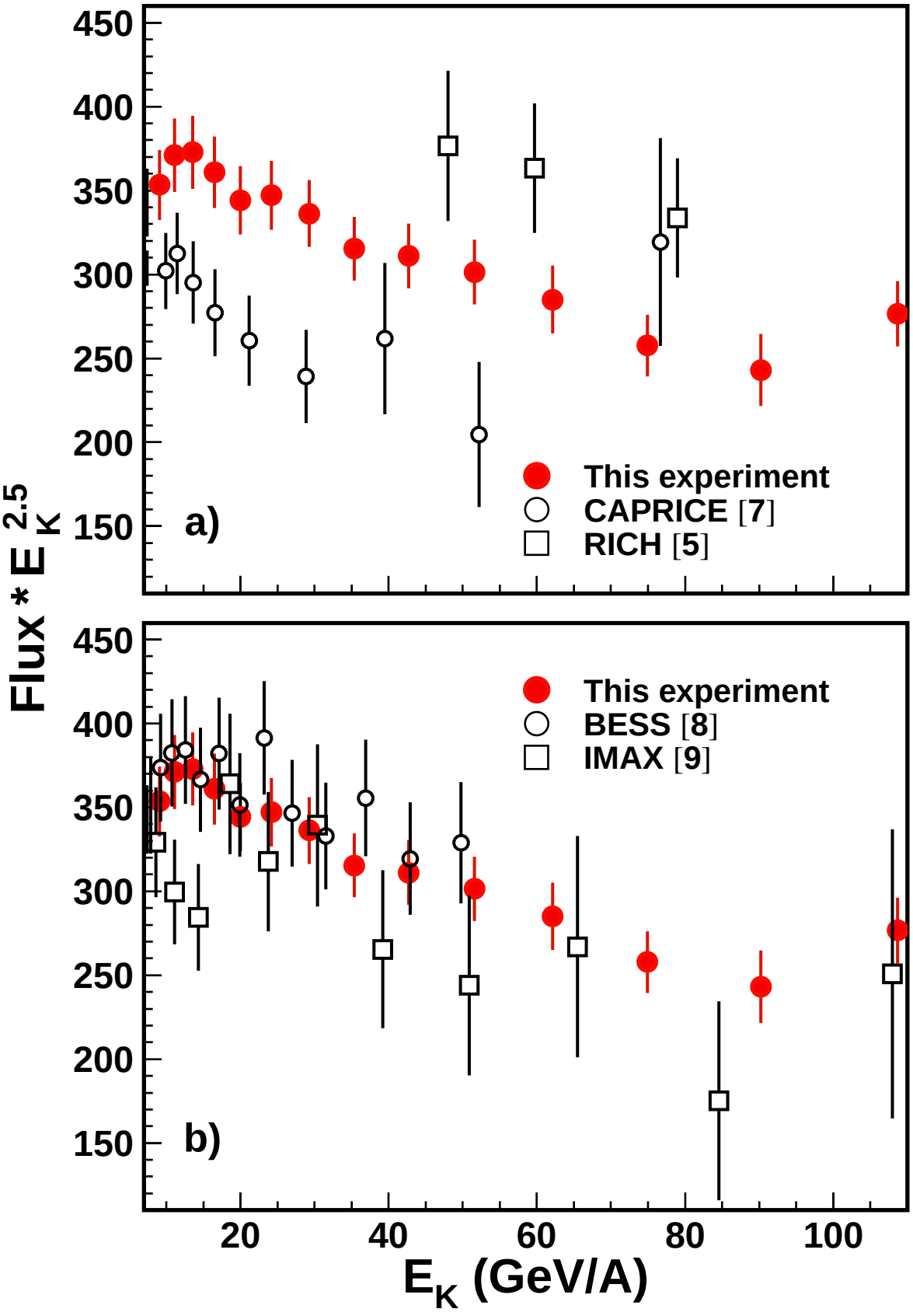

Figure 3: Comparison with recent measurements of the primary helium flux spectrum multiplied by $E_K^{2.5}$ in units of m^{-2} sec^{-1} sr^{-1} ($GeV/A)^{1.5}$.

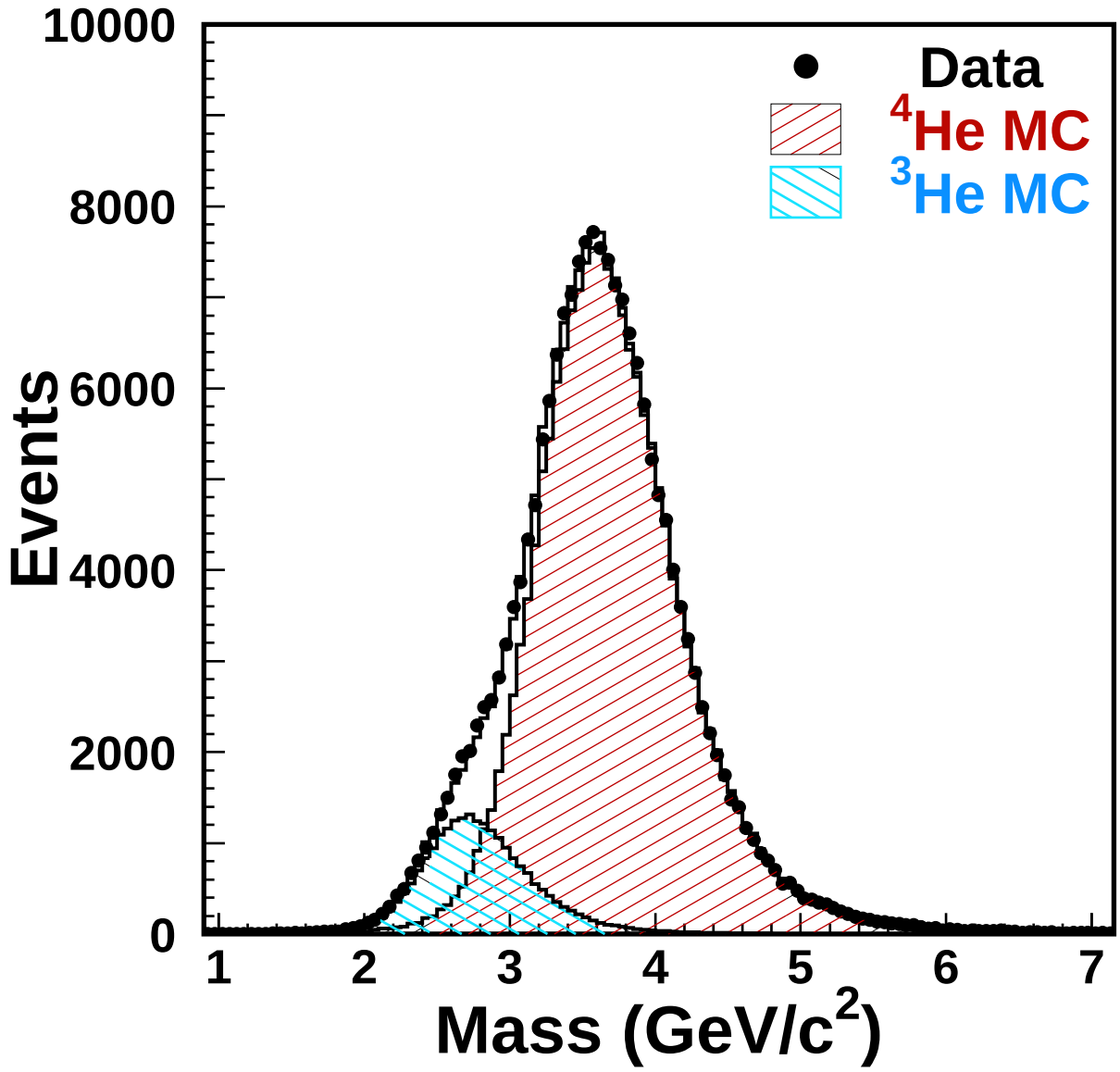

Figure 4: Mass distribution for helium events above geomagnetic cutoff for $|\Theta_M| > 0.9$ and $\beta < 0.9$. Filled circles are data for period (c). Histogram is a Monte Carlo simulation with 11.5 % ^{3}He.

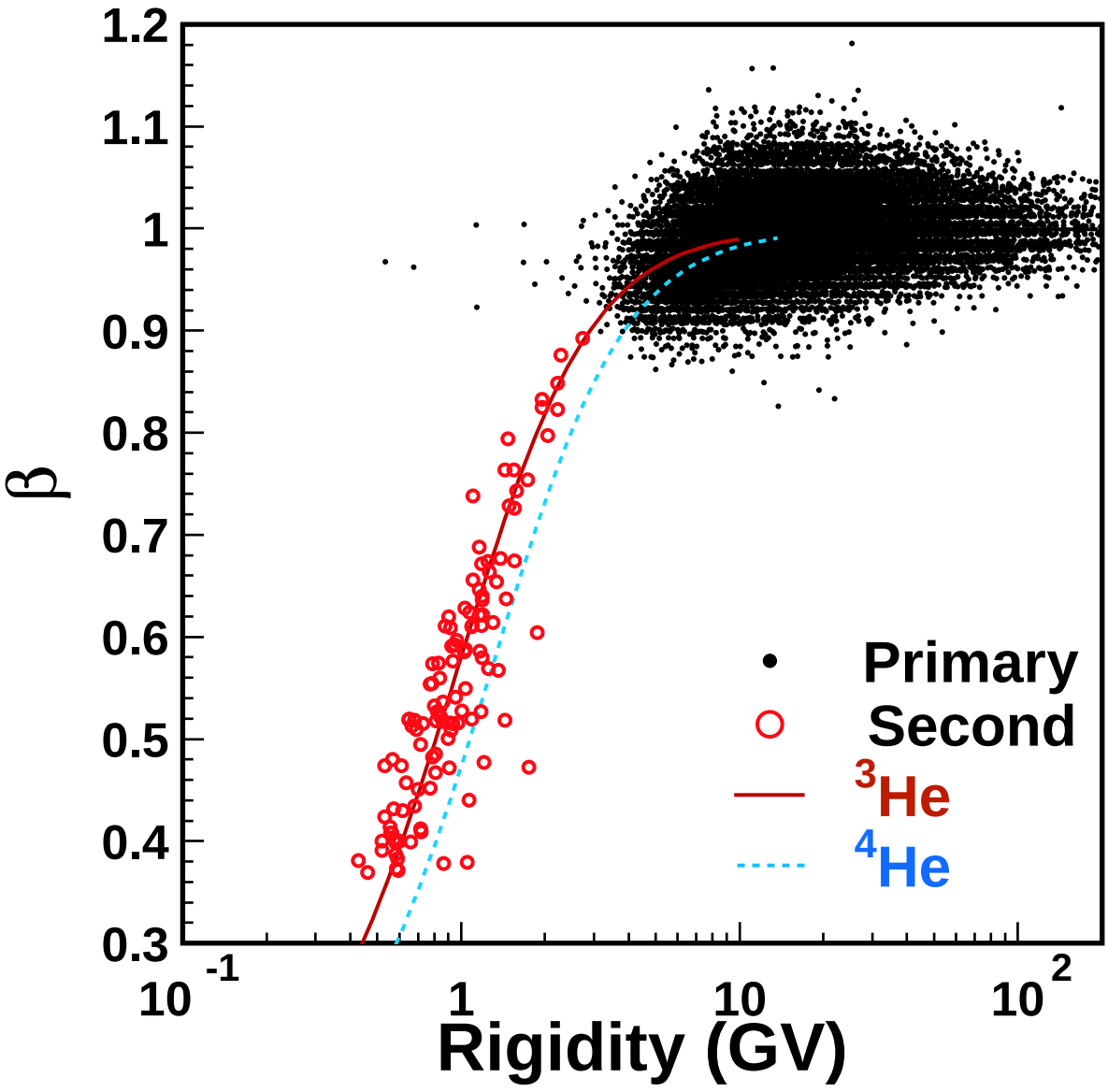

Figure 5: Correlation between rigidity and velocity for helium events detected at $|\Theta_M| < 0.6$. Dots denote events from the primary spectrum, and open circles those from under cutoff. The solid (dashed) line corresponds to ^{3}He (^{4}He).

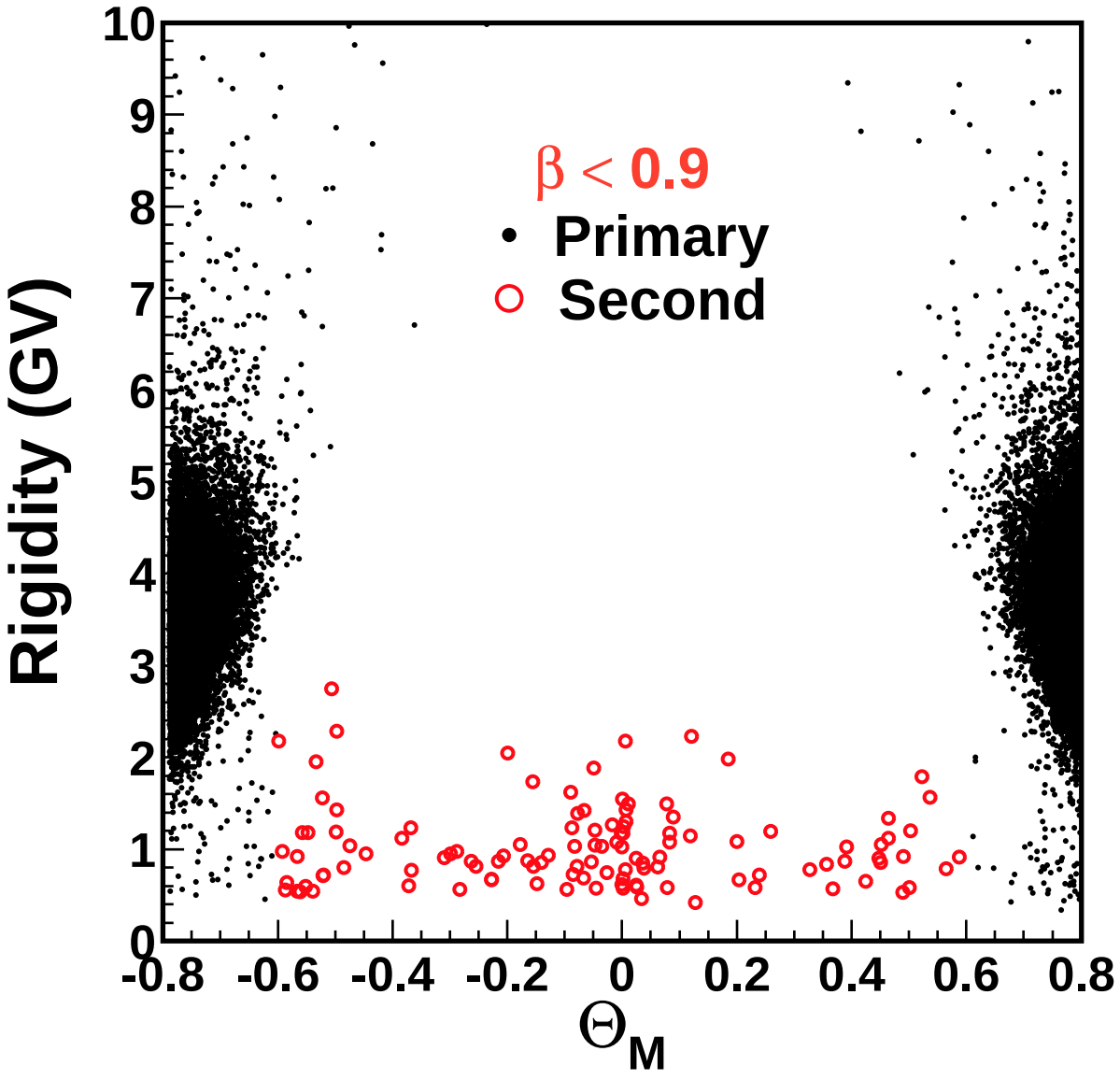

Figure 6: Rigidity versus Θ_M for events with $\beta < 0.9$. Dots and open circles as in Fig. 5.

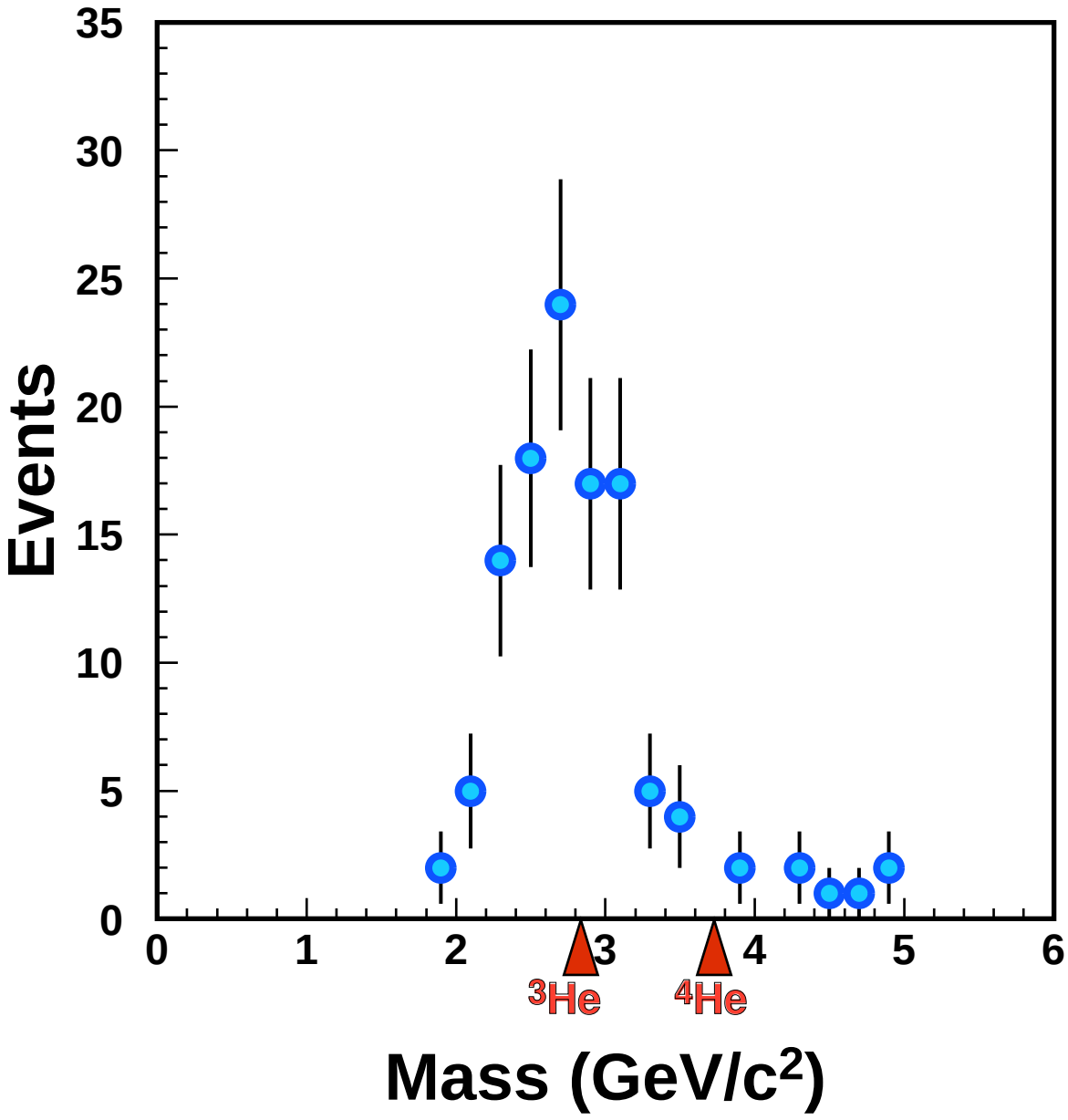

Figure 7: Reconstructed mass distribution for the second spectrum helium for $|\Theta_M| < 0.6$ compared with the masses of ^{3}He and ^{4}He.

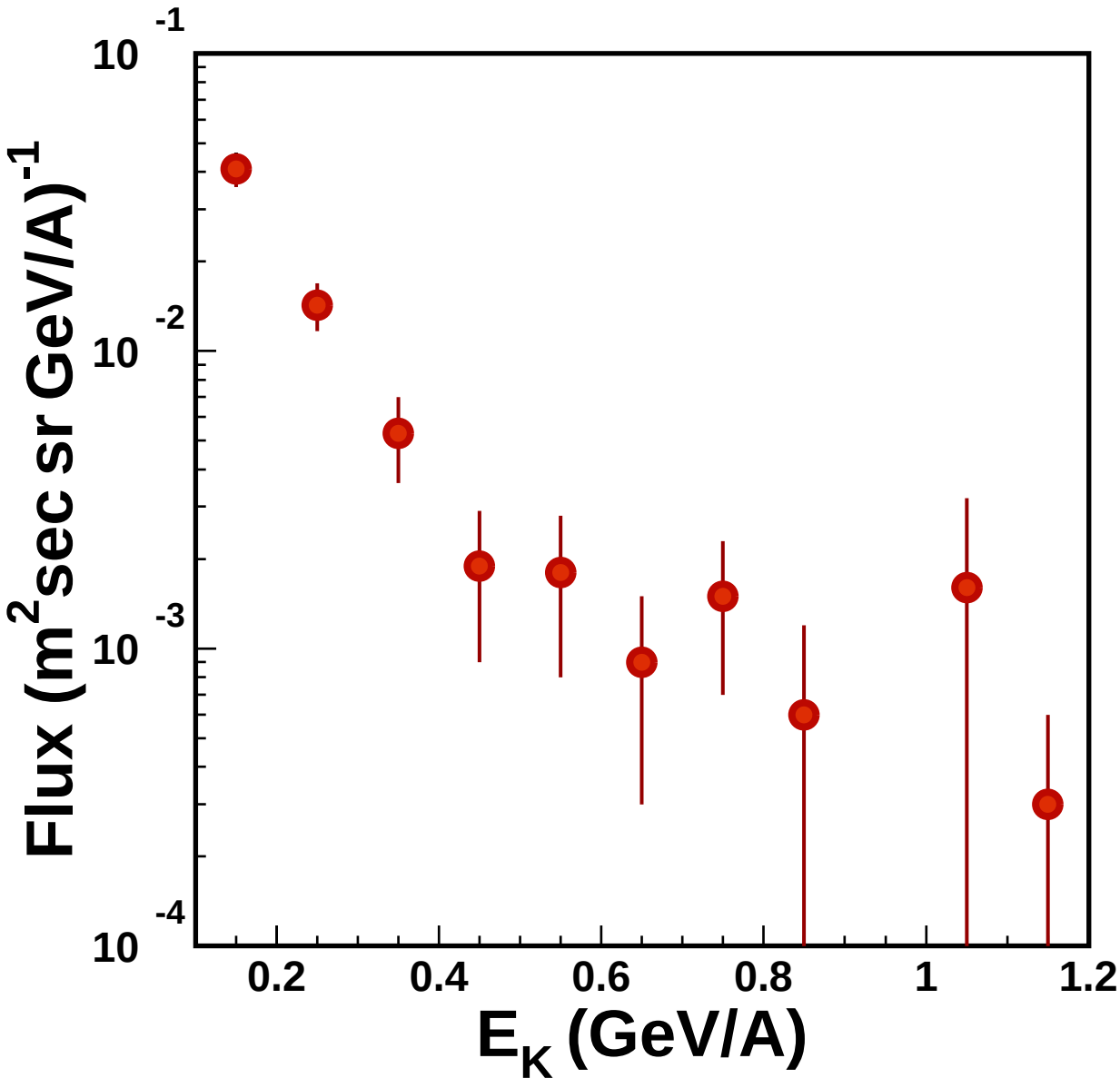

Figure 8: Second helium flux spectra for $|\Theta_M| < 0.6$.

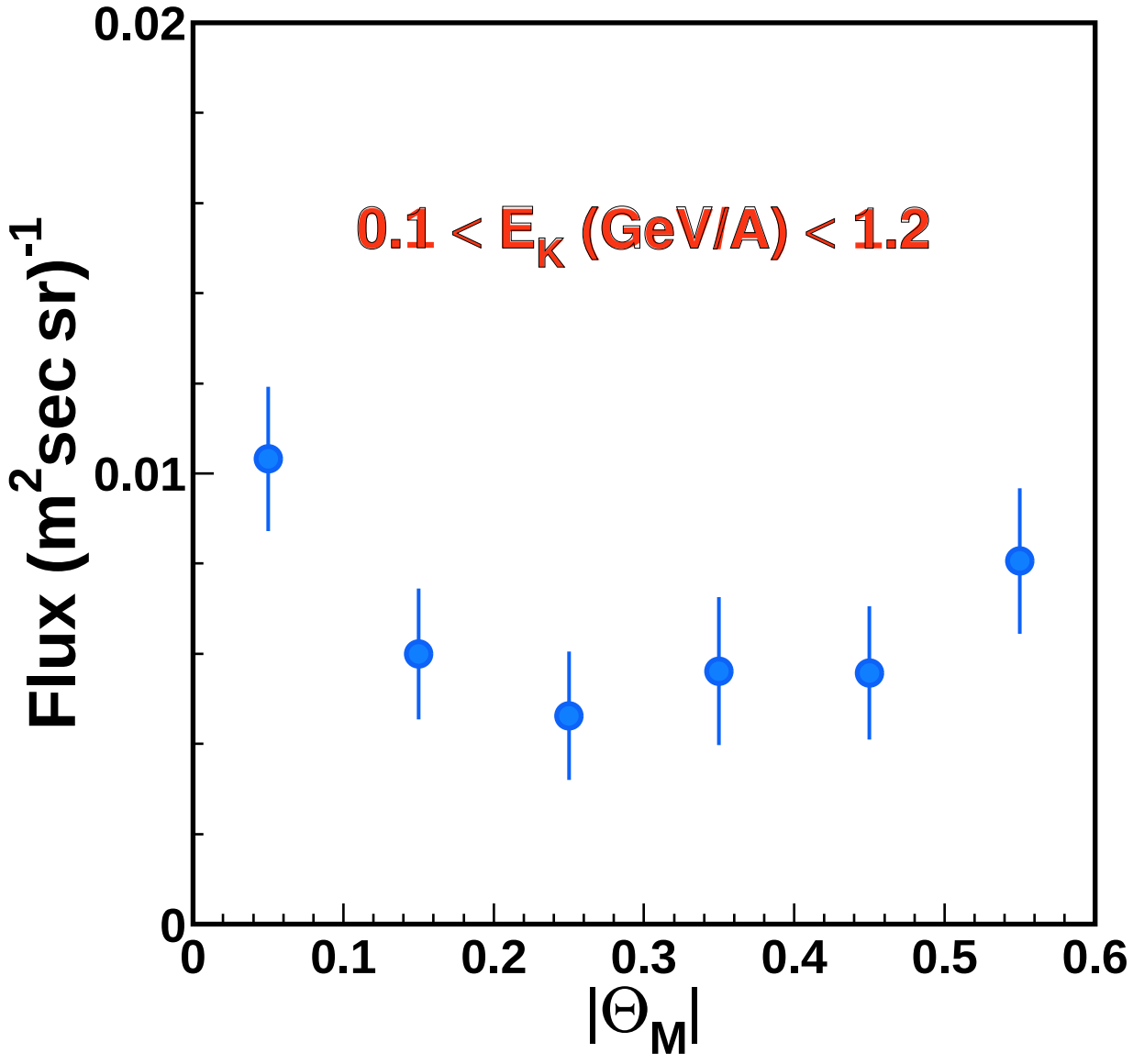

Figure 9: Average flux of the second helium spectrum versus geomagnetic latitude.

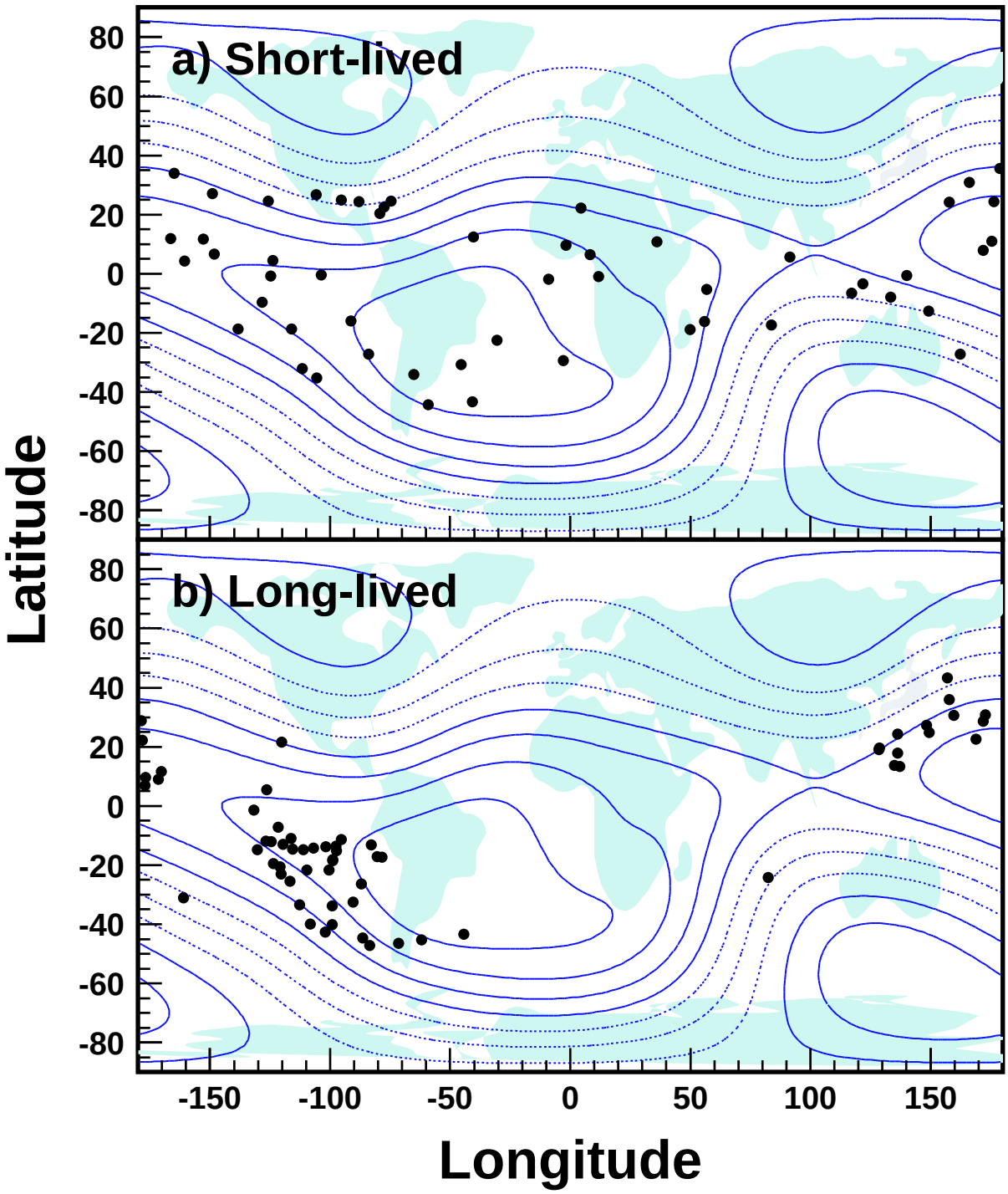

Figure 10: Geographical origin of a) “short-lived” and b) “long-lived” helium in the second spectrum. The lines indicate the geomagnetic field contours at 380 km.

AMS paper 05 "Helium in Near Earth Orbit"
Physics Letters B, Vol.494 (3-4) (2000) p193-202 .
Referee report :

" This is an exciting and important paper again from the AMS collaboration. It should be published.

There are only minor comments:

1) On p. 3 there is a rather cursory explanation of the proton contamination. Maybe it is possible to extend this brief explanation by a few more sentences, so that the reader understands better what was done to arrive at the numerical estimate of 10^4. Since the spectrum obtained at the end is very close to what earlier data had suggested as a good proton spectrum, any concern in this respect should be laid to rest.

2) Fig 1 on page 11 should really be complemented by a second figure which shows the fit, with the rigidity range actually used for the fit. When one looks along the face of the page, it becomes obvious, or at least looks obvious, that the data suggest a curvature, which of course it is not included in any powerlaw fit - and clearly does NOT warrant any other fit - but the reader would really appreciate seeing such a comparison between data and fit. The possibly easiest way to do this is to call the present figure 1 Fig 1a, and then include on the same page Fig 1b, where the flux has been multiplied by $R^{2.74}$, and R goes from 10 to 200 GV only - and this figure would then also show the fit. Then the ordinate could be greatly expanded, and the quality of the fit would be easily recognizable, as would be the quality of the data - and that is the key of this beautiful paper.

With such a Fig 1b any reader with a specific pet theory could just take a ruler and test it almost trivially against the data."